Effects of Irradiation and High Heat Flux on the Lifetime Performance of Ferritic and 316 Stainless Steels

Bruce Bernard Glasgow

May 1985

UWFDM-640

Ph.D. thesis.

Effects of Irradiation and High Heat Flux on the Lifetime Performance of Ferritic and 316 Stainless Steels

Bruce Bernard Glasgow

Fusion Technology Institute
University of Wisconsin
1500 Engineering Drive
Madison, WI 53706

http://fti.neep.wisc.edu

May 1985

UWFDM-640

Ph.D. thesis.

EFFECTS OF IRRADIATION AND HIGH HEAT FLUX ON THE LIFETIME PERFORMANCE OF FERRITIC AND 316 STAINLESS STEELS

by

BRUCE BERNARD GLASGOW

A thesis submitted in partial fulfillment of the
requirements for the degree of

DOCTOR OF PHILOSOPHY
Nuclear Engineering

at the
University of Wisconsin - Madison
1985

EFFECTS OF IRRADIATION AND HIGH HEAT FLUX ON THE LIFETIME PERFORMANCE OF FERRITIC AND 316 STAINLESS STEELS

Bruce B. Glasgow

Under the supervision of Professor W. G. Wolfer

Research into controlled thermonuclear fusion has reached an engineering phase where specific reactor designs and material selections are extensively examined. One material which has been included in several fusion reactor first wall designs is 316 stainless steel. The effort of this thesis is concentrated on comparing 316 stainless steel to ferritic steel for high heat flux and irradiation conditions expected in fusion reactors.

Under irradiation, metals form small bubbles within their grains; and because of (n, α) reactions, helium is usually concentrated within these bubbles. To model the pressure of the helium in a bubble, an Equation of State for helium has been developed. The results are used as input into a void (or bubble) swelling model. With the void swelling model, swelling rates for the two steels have been calculated. The ferritic steel is calculated to swell at a rate of about 0.3%/dpa; whereas, 316 stainless steel is calculated to swell at a rate of about 1%/dpa. Experimental results for 316 stainless steel show excellent agreement with the model.

Other aspects of high heat flux and irradiation are the potentially steep thermal stresses. There is also the evolution of the stress distribution as a result of swelling, and irradiation and thermal creep. A model to calculate the stress distribution in a thin shell element has been developed. The procedure is used along with assumed swelling and creep laws to model the stress distribution as a function of time. The results show that ferritic steel has a lower maximum stress by a factor of about 2 due to the better thermal and swelling properties.

Finally, the stress distribution is used as input to a crack growth and failure model. Failure is assumed when brittle fracture occurs or when the structure fails by plastic collapse. The results indicate that 316 stainless steel is much more susceptible to failure by crack growth than is ferritic steel. Further, failure in 316 stainless steel will be by brittle fracture; but, failure in ferritic steel will be by a combination of brittle and plastic failure due to the lower flow stress of ferritic steel. Ferritic steel is calculated to outlast 316 stainless steel from a crack growth standpoint by a factor of 10.

Approved:

Professor Wilhelm G. Wolfer

Nuclear Engineering

ACKNOWLEDGEMENTS

While being a graduate student at the University of Wisconsin - Madison and working on degree requirements and research is by no means an easy life; neither is it without reward – not just in the academic sense, but in quality of life. I have been very fortunate to have studied in Madison. The city is, in my opinion, a most pleasant environment. The students and faculty at the University are of extremely high caliber, both academically and personally. I would like to thank all of them with whom I have dealt, for their time and effort on my behalf. Of particular note is my advisor, Wilhelm Wolfer, whose guidance and patience made my studies enjoyable and rewarding.

Before coming to the University of Wisconsin, I was employed by the Department of Energy with the Division of Naval Reactors under Admiral Hyman Rickover. In those three years I learned a great deal about real engineering and engineering management. I would like to thank Phil Clark for his day-to-day example of how to get a job done right. Also, I would like to thank The Admiral for instilling in me a sense of pride in my work and for his relentless hard work and sound engineering judgement which made such an impression on me. The Admiral's work ethic is summed up on a notice which hung from his office wall

Late to bed, Early to rise
Work like hell, And you'll be wise.

For the past eight years the most influential and the most important person in my life has been my wife, Anna. Without her encouragement and

love, I may never have entered graduate school. Certainly, I would not have so enjoyed my life without her. Thank you, Anna, for marrying me.

Finally, I thank my parents, Robert and Jacqueline Glasgow. Their hard work with me through high school and their hard work by example, helped me accomplish whatever I set out to do. I hope that if I become a parent, I can be at least half as good a parent as they are.

Table of Contents

List of Tables

List of Figures

List of Publications

The following articles were published as part of my thesis research. Several of these articles have been incorporated as chapters into this thesis.

1. Glasgow, B. B., Si-Ahmed, A., and Wolfer, W. G., Helium Bubble Formation And Swelling In Metals, *Journal of Nuclear Materials* **103 & 104** (1981) 981-986. Also **UWFDM-430**, August 1981; and **DOE/ER-0046/7**, November 1981.

2. Glasgow, B. B. and Wolfer, W. G., Comparison Of Mechanisms For Cavity Growth by Athermal and Thermal Processes, *Journal of Nuclear Materials* **122 & 123** (1984) 503-508. Also **UWFDM-544**, September 1983.

3. Wolfer, W. G., Glasgow, B. B., Wehner, M. F., and Trinkaus, H., Helium Equation of State for Small Cavities: Recent Developments, *Journal of Nuclear Materials* **122 & 123** (1984) 565-570. Also **UWFDM-556**, September 1983.

4. Glasgow, B. B. and Wolfer, W. G., Modeling of Void Swelling in Irradiated Steels, *ASTM-STP-870*, to be published. Also **UWFDM-586**, June 1984.

5. Wolfer, W. G. and Glasgow, B. B., A Rate Theory Model for the Evolution of Network Dislocations in Irradiated Metals, to be published in *Acta Metallurgica*. Also **DOE/ER-0046/17**, May 1984. Also **UWFDM-602**, October 1984.

6. Glasgow, B. B. and Wolfer, W. G., Stress Analysis of a Duplex Structure in a High Heat Flux Environment, presented at *The Sixth Topical Meeting of the Technology of Fusion Energy*, March 1985. Also **UWFDM-616**, February 1985. To be published in *Fusion Technology*.

7. Glasgow, B. B. and Wolfer, W. G., Lifetime Analysis of Ferritic Steel Structures for High Temperature Fusion Applications, presented at *The Sixth Topical Meeting of the Technology of Fusion Energy*, March 1985. Also **UWFDM-615**, February 1985. To be published in *Fusion Technology*.

8. Glasgow, B. B. and Wolfer, W. G., Extension and Comparison of Various Equations of State for Gaseous and Solid Helium, **DOE/ER-0046/12**, February 1983.

9. Wolfer, W. G. and Glasgow, B. B., Growth Mechanisms for Helium Inclusions and Bubbles, **DOE/ER-0046/12**, February 1983.

10. Glasgow, B. B. and Wolfer, W. G., Simple Polynomial Expressions for the Helium Equation of State, **DOE/ER-0046/16**, February 1984.

11. Glasgow, B. B., Three Graphics Routines Available on the MFE Cray Computers, **UWFDM-589**, August 1984.

12. Glasgow, B. B., Review of Failure Criteria for Thin Wall Structures in a High Heat Flux Environment, **UWFDM-633**, March 1985.

13. Glasgow, B. B., EZGRAF, *NMFECC Buffer*, **Volume 8, Number 8**, August 1984, 1-2.

Chapter 1

INTRODUCTION

Research into controlled thermonuclear fusion has been conducted since the early 1950's. Many scientists now believe that fusion research is in a process of transition from a basic research phase into an engineering phase. Some fusion reactor designers anticipate the growth to a commercialization phase sometime in the early 21^{st} century. Before the commercialization of fusion reactors is realized, fusion reactors must be shown to be economically competitive with other power sources and to be environmentally acceptable. While the initial capital cost of a commercial fusion reactor will be in the billions of dollars, the initial cost may still be acceptable if the fusion reactors components are long lived. Or if long life is not possible, then replacement should be inexpensive and relatively easy. For the structural component designers the challenge presented by fusion reactors is particularly intriguing.

Past work by material structural designers has concentrated on the fusion reactor first wall. Being immediately next to the hot plasma, the first wall will be subject to neutron bombardment, plasma disruptions, high heat fluxes, and high temperatures. Because of the high heat fluxes, most first wall designs specify thin ($\sim$ 10 mm) first walls. Since the first wall is located at the inner most part of the reactor it is not expected to be replaced. Therefore, a first wall with $\sim$ 30 year lifetime is desired. There are also other components that have recently been included in fusion reactor designs which will be adjacent to the plasma. These include some type of impurity control device such as a limiter or divertor and, because of the plasma physics trend toward Radio Frequency (RF) heating, RF power launchers. The limiter, divertor, and RF launcher will also be subject to neutron flux, plasma disruptions, and high heat fluxes. Most designs for limiters and divertors assume a 2–4 year lifetime with relatively easy replacement. Once again because of the high heat flux thin walled structures are envisioned.

One consequence of neutron irradiation is radiation induced void swelling of the material. Excessive swelling of components can limit their lifetime because of dimensional changes and structural degradation. Because 316 stainless steel was an early choice for breeder reactors there is some long term swelling data available. However, for other materials under recent consideration for these high heat flux components such as ferritic steel and copper there is little data. In an effort to predict the swelling behavior of alternate materials as well as 316 stainless steel, a theoretical swelling model has been developed. And because the helium gas pressure inside the voids or bubbles can affect the swelling behavior, an equation of state for helium was also developed to accurately predict pressures at high densities and temperatures.

Stress cycling and high temperatures can cause cracks to grow in size and the growth may result in brittle fracture of components or a leak through a pressure boundary. Based on linear elastic fracture mechanics and collapse load considerations a theoretical and numerical model has been developed to follow crack growth and predict if brittle fracture, or leak through, or plastic collapse would occur. As part of the crack growth model the time evolution of the stress distribution through the thickness must be followed. A separate analytical and numerical approach has been developed for the stress distribution evolution.

As part of as overall effort to study ferritic steels as a potential structural material in fusion reactors, this thesis examines the effects of irradiation and high heat flux on the lifetime performance of a ferritic steel structure and compares the results to an identical analysis done using 316 stainless steel. The areas of study can be divided into 6 separate investigations:

1. As previously stated, neutron irradiation results in microstructural changes in metals. One of these changes is the nucleation and growth of helium filled bubbles. The density of helium atoms in these bubbles could become quite large; and consequently, the helium gas would no longer obey the ideal gas law. Therefore, in order to more accurately predict the pressure in the bubbles, an Equation of State was developed for dense helium gas and liquid helium. The pressure within these bubbles is an important parameter in predicting early growth behavior of the bubbles.
2. Another microstructural change which occurs as a result of irradiation is the evolution of the dislocation network. Cold-worked and annealed dislocation networks evolve with irradiation until some steady state density is reached. The importance of the dislocation network evolution is that the network is a major sink for point defects which are created as

a result of irradiation. The strength of this sink for point defects will affect the swelling behavior of the material.

3. The results of the previous two models are used as input to a void swelling model which calculates the swelling rate of metals under irradiation. The void swelling model is based on rate theory and includes time-dependent sink strengths and bias factors. The swelling rate as a function of time gives one of the inelastic strains rates which can be used in stress analysis of the structure.
4. In order to predict the stress levels in a thin-walled shell subjected to a fusion type environment, principal stress equations were developed for a thin shell element with arbitrary membrane loads and bending moments as boundary conditions. Further, understanding the time-dependent inelastic strain rates (swelling and creep rates), allows the calculation of a time-dependent stress distribution.
5. The time-dependent stress distribution is used as input into a crack propagation model based on Linear Elastic Fracture Mechanics. The LEFM model calculates how a crack will grow with time and, given the stress distribution and crack geometry, when brittle fracture or leak-through would occur. Either of these two conditions would result in failure of the structure.
6. The LEFM model does not take into account a potentially important failure mode — plastic collapse. In the final section of this thesis, incor-

poration of plastic collapse into the LEFM methodology is derived and the effect on predicted lifetime is discussed.

The overall scope of this research is to develop an analysis methodology for comparing different materials and different thermo-physical conditions of thin-walled structures. The analysis can be used as a tool in performing scoping studies on different materials and different assumed thermo-physical conditions.

Chapter 2

HELIUM EQUATION OF STATE

2.1. Introduction

Helium produced by (n,α) reactions or injected into metals is essentially insoluble. Therefore, it has the natural tendency to precipitate and to form bubbles. The pressure in small bubbles can be extremely large, and a realistic equation of state (EOS) is required to evaluate it. Unfortunately, the experimentally determined EOS for helium does not completely cover the range of temperatures and pressures of interest. This is illustrated in Figure 2.1 where the various regions are shown in which experimental data have been obtained. It is seen that only the recent measurements by Mills *et al.* [2.1] cover the range of high pressures equal to $2\gamma/r$ when r is small, where γ is the surface energy and r the radius of the bubble. A typical value for γ is 2 J/m^2. EOS measurements at elevated temperatures are still lacking. Empirical equations of state, such as the Van der Waals law, which have been fit to the experimental data, cannot be extrapolated with any confidence to the high pressures existing in small bubbles. The more theoretically based virial equation of state, being a power series expansion in the density of gas atoms, is naturally restricted to low values of the densities. Again, its extrapolation to high pressures is not possible. It is therefore of interest to develop a theoretical EOS which can be used for all temperatures and pressures of interest. Accordingly, a theoretical EOS has been developed for gaseous and solid helium.

It has recently become feasible to directly measure the density of helium in small bubbles. In fact, two techniques have been employed for this task: electron loss spectroscopy and vacuum ultra-violet absorption. In both cases helium is detected by the excitation of the orbital electrons. The energy levels involved in the transition of the orbital electrons is shifted by different amounts depending on the density of helium. Jäger *et al.* [2.2] have carried out experiments on nickel and aluminum implanted at room temperature with helium to concentrations somewhat below the critical value to produce blistering. The analysis of the orbital electron transitions revealed that the pressure in the helium bubbles was on the order of 50 GPa in the case of nickel and about 13 GPa in the case of aluminum. Note that the ratio of the pressure in the bubble to the shear modulus of the host metal is 0.64 and 0.52, respectively.

The ultra-violet absorption measurement of Rife *et al.* [2.3] in aluminum films bombarded at room temperature with 5 keV helium ions yielded a density of 7 to 14 $\times 10^{22}$ cm^{-3}, or a helium to vacancy ratio of 1 to 2 in bubbles about 5 nm in diameter. The measurement by Jäger *et al.* gave a helium density of 14 $\times$ 10^{22} cm^{-3}. It is most likely that helium is in the solid form at these densities at room temperature. In fact, there exists at least one data point which confirms this. Besson and Pinceaux [2.4] have solidified helium at room temperature in a diamond anvil cell and observed

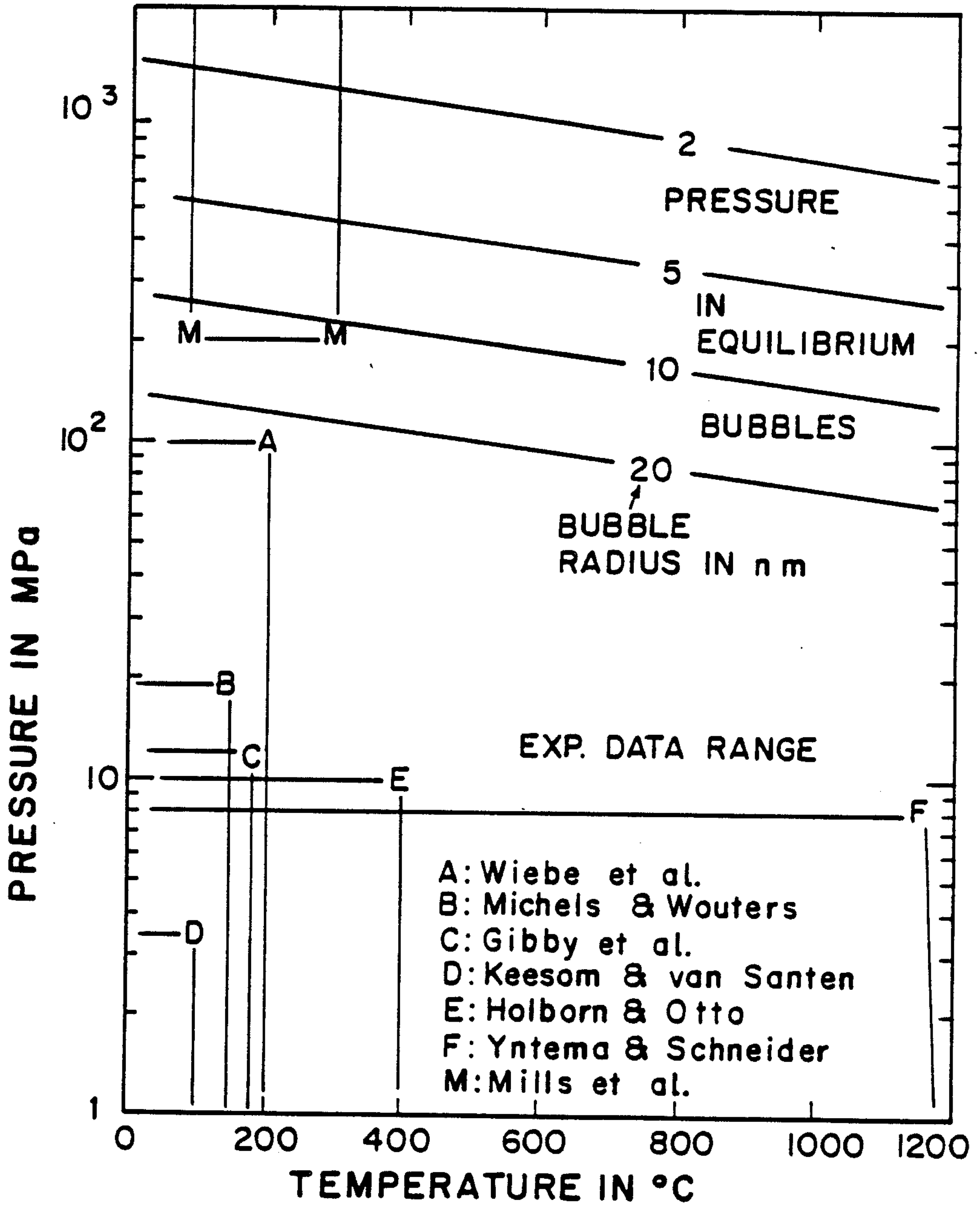

Figure 2.1. Ranges of temperature and pressure where experimental data exist for the EOS of helium. References to data can be found in Reference 1.

the actual melting process as well as grain boundaries in the solid phase. The pressure at melting and room temperature was determined to be ~ 11.5 GPa, and the density at melting was estimated to be about 15×10^{22} cm^{-3}. In the electron microscopy analysis of helium-implanted molybdenum Evans *et al.* [2.5] have identified helium platelets. The formation of non-spherical precipitates is again an indication that these platelets consist of solid helium.

The above examples show that indeed the densities and pressures within helium bubbles can be quite large and, in fact, solid helium can be formed. As stated previously, extrapolation of low density equations of state is not considered adequate. In the following sections of this chapter two different theoretical helium equations of state will be developed: one for gaseous helium and one for solid helium. A comparison to the Mills [2.1] empirical equation of state for low temperatures is also presented.

2.2. The Gaseous EOS Based On Perturbation Theory

One of the most successful approaches to model a liquid or a dense gas is by the so-called perturbation theory [2.6]. The fluid is modeled as a system of hard spheres. However, in order to account for the "softness", or finite steepness, of the repulsive part of the actual interatomic potential, the diameter d of the particles is made to depend on temperature and density according to Verlet and Weiss [2.7]

$$d = d_B(T)[1 + \delta(T)\psi(y)] \tag{2.1}$$

where $y = (\frac{\pi}{6})d^3\frac{N}{V}$ is the packing fraction and N is the number of helium particles in a volume V. If the interatomic potential $U(x)$ is expressed in terms of the dimensionless distance $x = r/\sigma$, where σ is the distance r where U becomes repulsive and ϵ is the depth of the potential well (see Figure 2.2), then

$$d_B(T)/\sigma = \int_0^{x_m} \{1 - \exp[-(U+\epsilon)/kT]\}\, dx \tag{2.2}$$

$$[1+\delta(T)](d_B/\sigma)^2 = 2\int_0^{x_m} \{1 - \exp[-(U+\epsilon)/kT]\}\, x\, dx \tag{2.3}$$

x_m denotes the location of the minimum of $U(x)$, *i.e.* $U(x_m) = -\epsilon$. The function $\psi(y)$ which is given in References [2.7,2.8] makes Equation 2.1 an implicit relationship for d, and numerical solution is required. Once d, and hence y, are known, the compressibility factor $z = pV/NkT$ is given by Carnahan and Starling [2.9] as

$$z_{HS} = (1 + y + y^2 - y^3)/(1-y)^3 \tag{2.4}$$

Several corrections to this equation are, however, required to account for quantum effects and for the attractive part of the interatomic potential.

2.3. The Quantum Correction

For a fluid comprised of light atoms, quantum corrections are important [2.6]. These corrections give rise to an additional term to the compressibility factor. If A_{cl} represents the free energy of the fluid treated with classical

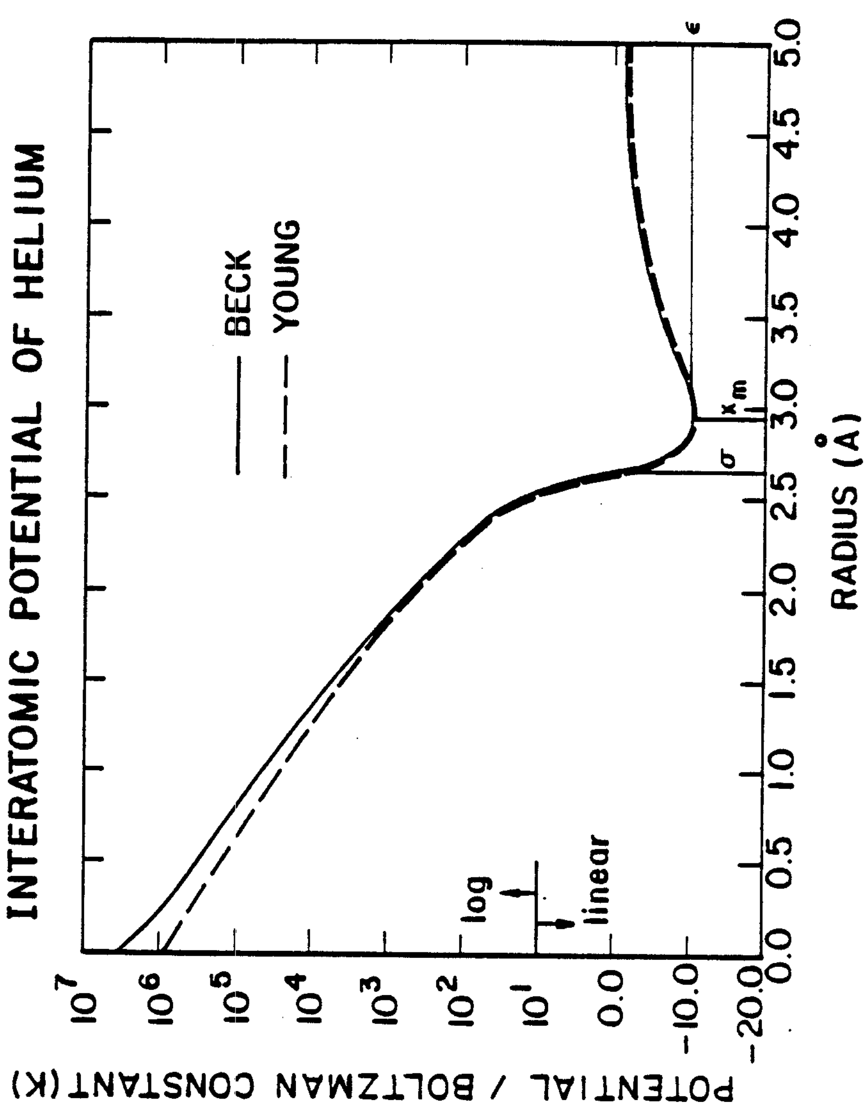

Figure 2.2. Interatomic potential for helium according to Beck [2.12] and Young *et al.* [2.13].

statistical mechanics, the inclusion of quantum corrections gives the following expression for the total free energy [2.6]

$$A = A_{cl} + \frac{h^2N^2}{24\pi mkTV}\int g(r)\nabla^2U(r)r^2\,dr \tag{2.5}$$

where h is Planck's constant, m the atomic mass, and $g(r)$ is the radial distribution function. An exact solution exists for the radial distribution function in the Percus-Yevick solution [2.10]. However, this analytical form is too cumbersome to use; therefore, a recent approximation to it developed by Shinomoto [2.11] is used instead

$$g(x,y) = \begin{cases} 0 & \text{for } x < \frac{d}{\sigma} \\ \exp[\frac{1}{2}y(x\frac{\sigma}{d} - 2)^2(x\frac{\sigma}{d} + 4)] & \text{for } \frac{d}{\sigma} \le x \le 2\frac{d}{\sigma} \\ 1 & \text{for } x > 2\frac{d}{\sigma} \end{cases} \tag{2.6}$$

As Shinomoto has shown, the hard sphere EOS derived with this radial distribution function agrees quite well with the molecular dynamics results.

The form of the radial distribution function in Equation 2.6 has the advantage that the derivative $(\partial A/\partial V)$ can be obtained prior to solving the integral in Equation 2.5. The compressibility factor can be written as

$$z = \frac{pV}{NkT} = -\frac{V}{NkT}\frac{\partial A}{\partial V} = y\frac{\partial(A/NkT)}{\partial y} = z_{cl} + z_Q \tag{2.7}$$

where

$$z_Q = \frac{h^2}{m(kT)^2\sigma^2}\,y\,\frac{\sigma}{d}\frac{\partial}{\partial y}[y\,\beta(y)] \tag{2.8}$$

and

$$\beta(y) = g(1,y)\left(-\frac{dU}{dx}\right)_{x=d/\sigma} + \left(\frac{\sigma}{d}\right)^2\int_{d/\sigma}^{2d/\sigma}\left(-\frac{dU}{dx}\right)\frac{\partial g}{\partial x}x^2dx \tag{2.9}$$

Using the above expressions

$$z_Q = \frac{h^2}{m\,(\sigma kT)^2}\frac{\sigma}{d}\Bigg[\left(1+\frac{5}{2}y\right)\exp\left(\frac{5}{2}y\right)\left(-\frac{dU}{dx}\right)_{x=d/\sigma} + \frac{3}{2}y\int_1^2\left(-\frac{dU}{dx}\right)\left[2+y\psi\left(\rho\right)\right]g\left(\rho,y\right)\left(\rho^2-2\right)\rho^2\,d\rho\Bigg] \tag{2.10}$$

For a give interatomic potential $U(x)$ the integral in Equation 2.10 can be evaluated numerically.

2.4. The Contribution From The Potential Well

So far the gaseous helium has been treated as a system of hard spheres, *i.e.* as a fluid system whose particles possess only a repulsive interaction. However, it is the attractive forces that actually give rise to the liquid phase. Since the depth of the potential well ϵ is small for helium it is approximated by a square well of the same depth and of width $d_w - d$. The value for d_w is chosen to be 0.35 nm to approximate the actual shape of the potential well calculated by Beck [2.12] and Young *et al.* [2.13].

For a square well potential Reijnhart [2.14] has derived the following EOS for the attractive potential

$$z_A = -4y\left(\frac{d_w}{d}\right)^3 g\left(\frac{d_w}{d},y\right)\left[1-\exp(-\epsilon/kT)\right] \tag{2.11}$$

Once again the radial distribution function of Shinomoto is used to evaluate Equation 2.11.

2.5. Evaluation Of The Gaseous EOS

The total compressibility factor is taken to be

$$z = z_{HS} + z_Q + z_A \tag{2.12}$$

In evaluating z, the interatomic potentials $U(x)$ of both Beck [2.12] and Young *et al.* [2.13] were utilized. As Figure 2.2 shows the two potentials differ only significantly for very small interatomic distances. As pointed out by Young *et al.*, the reduction of the interatomic potential reflects the many-body interactions at high densities and temperatures, an affect not accounted for in the Beck potential.

Figure 2.3 shows the predicted results for the Beck and Young potential. The EOS for the gaseous state is represented by the curve below the break points, whereas the solid EOS, discussed in the following section, is shown by the curves above the break points. The empirical EOS of Mills *et al.* [2.1], valid for temperatures at or below 300°K, is also shown for comparison at 200°K.

2.6. The Solid EOS For Helium

The interatomic potential, see Figure 2.2, of helium has a very shallow potential well with a depth of about 10°K. At the same time, it is a very light element. As a result of these two facts, the zero point vibrations are large, and helium does not solidify at atmospheric pressures. In fact, the solid phase of helium exists only for pressures greater than about 2.5 MPa ($\sim$ 25 atmospheres).

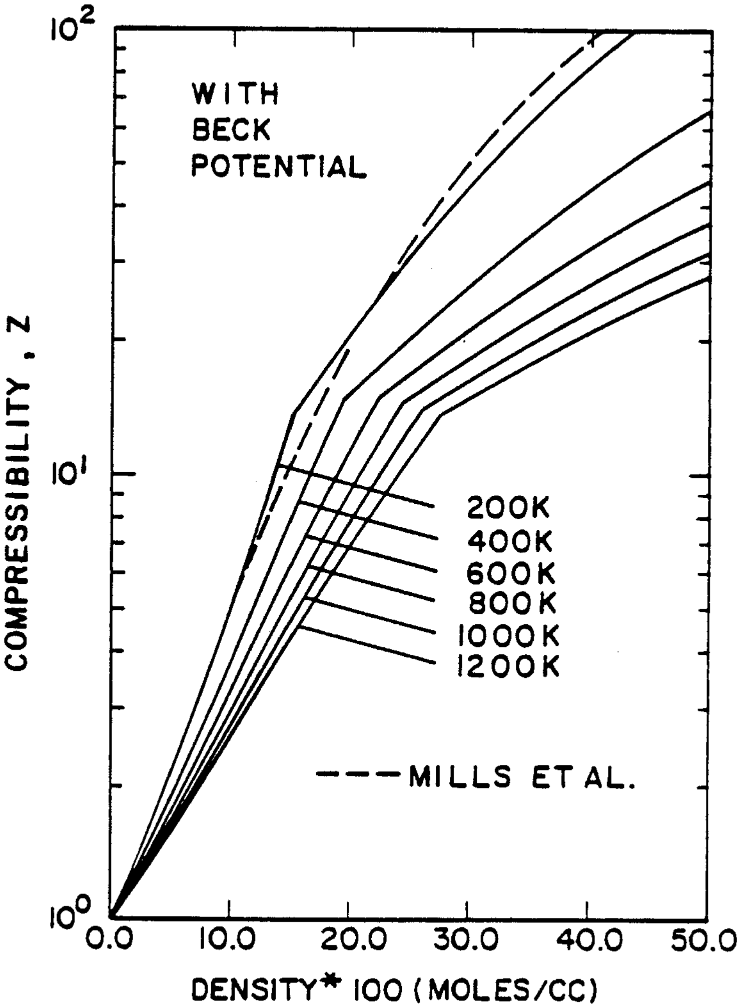

Figure 2.3a. Theoretical EOS using the Beck potential for the fluid EOS.

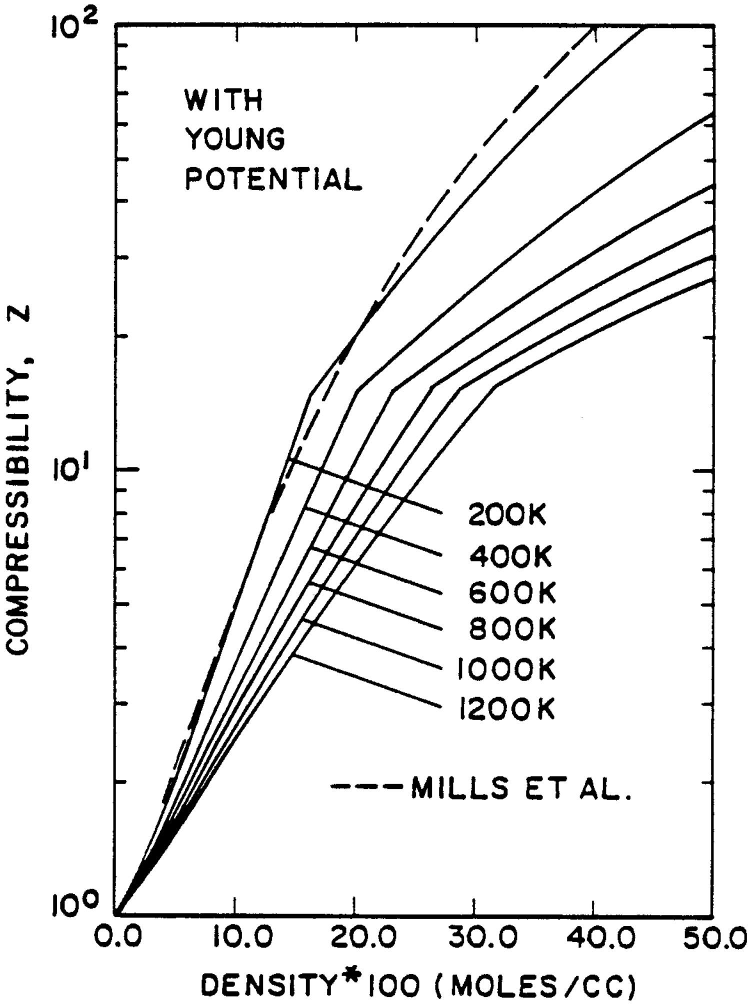

Figure 2.3b. Theoretical EOS using the Young potential for the fluid EOS.

In the quasi-harmonic approximation of the solid helium, the free energy is the sum of the potential energy A_o of an ideal lattice with all atoms located at their equilibrium positions plus a vibrational free energy A_h. As a result of this division, the pressure may also be written as a sum of two contributions, $p_o + p_h$, where $p_o = \partial A_o / \partial V$ and $p_h = \partial A_h / \partial V$.

The evaluation of p_o or A_o for solid helium requires extensive quantum mechanical computations for the following reasons. First, the interatomic interaction in a non-ionic solid is determined by the electronic structure of the valence and conduction bands at high densities. Second, in the case of solid helium, the ground state vibrations (at 0°K) are no longer negligible, and the nucleus must be described by a wave function rather than by a point charge fixed at the ideal lattice point. The latter aspect is particularly important at low densities of the solid when the average interatomic distance is larger than the atomic diameter σ, *i.e.* when the packing fraction is less than one.

Ground state pressures for this case have been obtained by Hansen and Pollock [2.15], and their results are shown in Figure 2.4. For higher densities, both Young *et al.* [2.13] and Zeller [2.16] have carried out electron band structure calculations, and their results are also indicated in Figure 2.4. Finally, Trinkaus [2.17] evaluated the static lattice energy for a face centered cubic helium crystal assuming that the pair-interaction is given by Beck's potential. The derived ground state pressure is remarkably close to the electron band structure results of Young *et al.* and to the results of Hansen and Pollock for medium densities. Deviations at very high densities are as expected, since the Young potential is softer than the Beck potential.

Both the low-density results of Hansen and Pollock [2.15] and the high-density results of Young *et al.* [2.13] can be fit to a smooth function of the form

$$p_o(\mathrm{MPa}) = [a + b]^6 \tag{2.13}$$

where

$$a = \left[\frac{1}{2}B^{1/2} + Q^{1/2}\right]^{1/3} \tag{2.14}$$

$$b = \left[\frac{1}{2}B^{1/2} - Q^{1/2}\right]^{1/3} \tag{2.15}$$

$$Q = \frac{1}{27}(B^3/A)^{1/2} + \frac{1}{4}By_o^2 \tag{2.16}$$

A and B are two constants with the values indicated in Figure 2.4.

It must be noted that Equation 2.13 is not entirely consistent as the results by Young *et al.* contain no contributions of the ground state vibrations to p_o. However, for high packing fractions, vibrations contribute relatively little to the total pressure.

In order to estimate the pressure contribution of lattice vibrations at finite temperatures, the Debye theory is employed together with a volume dependent Debye temperature to give the vibrational frequency spectrum. The Debye temperature is given by

$$\theta_D(V,T) = \theta_{Dm}(T)(V_m/V)^{\gamma} \tag{2.17}$$

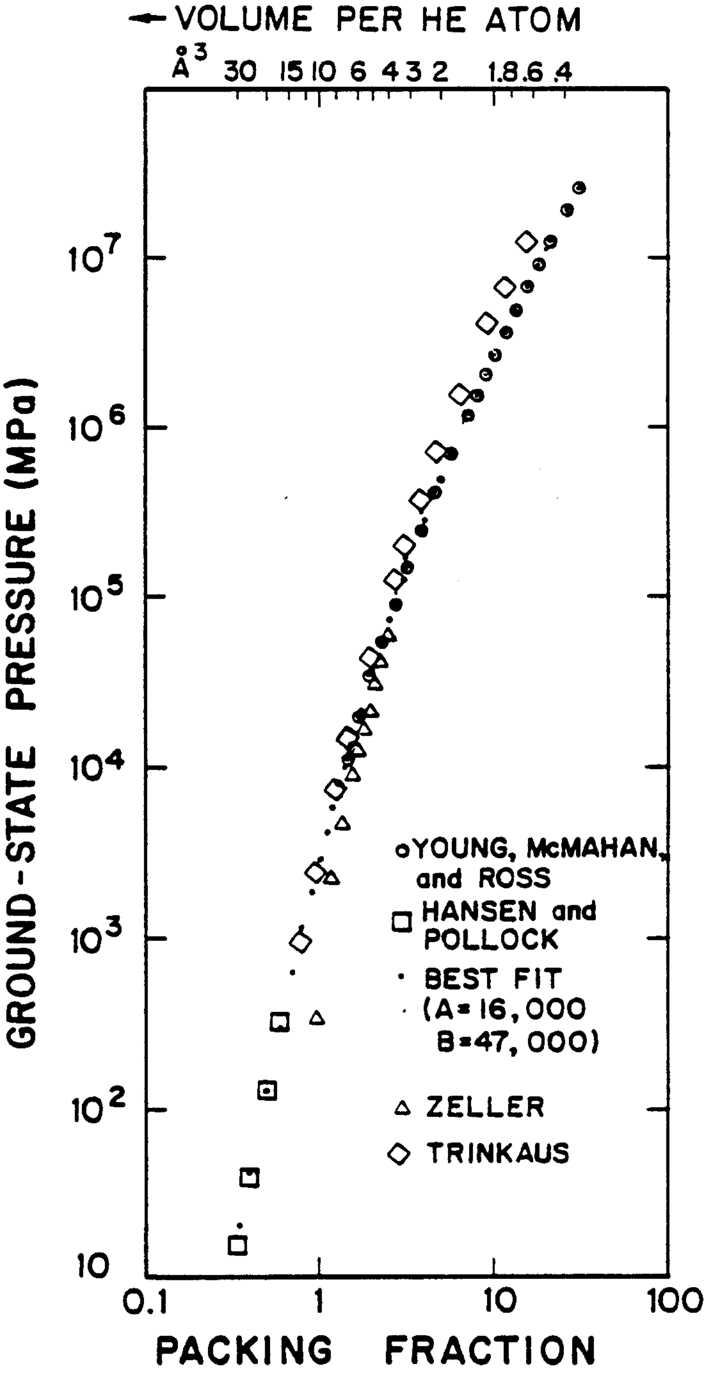

Figure 2.4. The ground-state pressure of solid helium at 0°K as a function of the packing fraction.

where θ_{Dm} is the Debye temperature at melting and given by the Lindemann law

$$\theta_{Dm} = 16.15931\, T^{1/2}\, y_{om}^{1/3} \tag{2.18}$$

the form of which has been shown to be valid [2.18] for several rare gas solids. The packing fraction at melting, y_{om}, is based on the theoretical results of Young *et al.* [2.13] which can be expressed by the equation

$$y_{om}^{1/3} = 0.15542\, T^{0.359} + 1.1292 \times 10^{-6}\, T^{1.903} \tag{2.19}$$

and the Grüneisen constant γ can be obtained by taking the derivative $(\frac{-d \ln \theta_{Dm}}{d \ln V})$ of Equation 2.18 and the following equation is obtained

$$\gamma = \frac{0.269\, T^{-0.641} + 1.953 \times 10^{-7}\, T^{0.903}}{0.0965\, T^{-0.641} + 3.7165 \times 10^{-7}\, T^{0.903}} \tag{2.20}$$

The pressure contribution by thermal vibrations is then obtained from

$$p_h = 9\gamma k T \left(\frac{N}{V}\right) (T/\theta_D)^3 \int_0^{\theta_D/T} x^3/(e^x - 1)\, dx \tag{2.21}$$

where the term due to ground state vibrations has been omitted as it is already included in p_0.

The compressibility factor for the above EOS for solid helium is shown in the upper parts of Figure 2.3.

2.7. Conclusions

A numerical solution for the EOS of helium has been developed. For the gaseous phase, the total compressibility is taken to be the sum of three components: 1) an attractive component, 2) a quantum mechanical component, and 3) a hard-sphere component. The attractive component [2.14] and the quantum correction component [2.6] use the helium radial distribution function derived by Shinomoto [2.11]. The hard-sphere component is given by the Carnahan-Starling [2.9] approximation, Equation 2.4, which is explicit in the packing fraction y. The packing fraction is, in turn, dependent on the diameter of the so-called "hard-sphere" helium atom. The diameter is, however, allowed to vary as a function of temperature and density.

For the solid phase of helium, the total compressibility is taken to be the sum of a ground state and a vibrational state of the lattice atoms. The ground state compressibility is determined by a fit to the results of various theoretical approaches reported in the literature as shown in Figure 2.4. The lattice vibration contribution is found by the Debye theory where the Debye temperature is taken to be a function of temperature and volume.

It was assumed that the phase transition between gaseous and solid helium occurs whenever the compressibility factors for the gas and the solid phases become equal. In other words, the phase with the lowest compressibility factor is the one which exists for a given temperature and volume. It should be noted that this is only approximately correct as the phase change at constant pressure is accompanied by a small volume change typically on the order of about 4%. Also, the Young potential is chosen over the Beck potential because of better accuracy at small interatomic distances.

By using the gaseous and solid EOS described above, a comprehensive EOS is derived as shown in Figure 2.3 This EOS can be used in void swelling calculations where the pressure of helium within a void can determine the onset of swelling.

References

[2.1.] Mills, R. L., Liebenberg, D. H., and Bronson, J. C., *Physical Review B* **21** (1980) 5137.

[2.2.] Jäger, W., Manzke, R., Trinkaus, H., Crecelius, G., Zeller, R., Fink, J., and Bay, H. L., *Journal of Nuclear Materials* **111 & 112** (1982) 647.

[2.3.] Rife, J. C., Donnelly, S. E., Lucas, A. A., Gilles, J. M., and Ritsko, J. J., *Physical Review Letters* **46** (1981) 1220.

[2.4.] Besson, J. M. and Pinceaux, J. P., *Science* **260** (1979) 1073.

[2.5.] Evans, J. H., van Veen, A., and Caspers, L. M., *Scripta Metallurgica* **15** (1981) 323.

[2.6.] Barker, J. A. and Henderson, D., *Reviews of Modern Physics* **48** (1976) 587.

[2.7.] Verlet, L. and Weiss, J. J., *Physical Review A* **5** (1972) 432; and *Molecular Physics* **24** (1972) 1013.

[2.8.] Wolfer, W. G., in "Effects of Radiation on Materials", Eds. Brager,H. R. and Perrin,J. S., **ASTM STP 725** (1981) 201.

[2.9.] Carnahan, N. F. and Starling, K. E., *Journal of Chemical Physics* **51** (1961) 635.

[2.10.] Perram, J. W., *Molecular Physics* **30** (1975) 1505.

[2.11.] Shinomoto, S., *Physical Letters* **89A** (1982) 19.

[2.12.] Beck, D. E., *Molecular Physics* **14** (1968) 311.

[2.13.] Young, D. A., McMahon, A. K., and Ross, M., *Physical Review B* **24** (1981) 5119.

[2.14.] Reijnhart, R., *Physica* **83A** (1976) 533.

[2.15.] Hansen, J. P. and Pollock, E. L., *Physical Review A* **5** (1972) 2651.

[2.16.] Zeller, R., private communication with W. G. Wolfer.

[2.17.] Trinkaus, H., *Radiation Effects*, **78** (1983).

[2.18.] Crawford, R. K., "Melting, Vaporization and Sublimation", Chapter II of "Rare Gas Solids", Volume II, Editors M. L. Klein and J. A. Venables, Academy Press, London, 1976.

Chapter 3

DISLOCATION EVOLUTION IN METALS UNDER IRRADIATION

3.1. Introduction

During the bombardment of metals with energetic particles, vacancies and self-interstitials are produced. At irradiation temperatures above the onset for vacancy migration but below the temperature where self-diffusion is rapid, the absorption of vacancies and interstitials at dislocations leads eventually to dramatic changes of the dislocation density. The dislocation density is important in calculating void swelling because the voids and the dislocations are the major sinks for point defects. Accordingly, in order to more accurately model void swelling, a dislocation evolution model is developed.

Other microstructural defects also arise, such as small dislocation loops and precipitates as a result of the irradiation. However, the evolution of the dislocation density is nearly independent of the evolution of all other microstructural features. Well-annealed metals exhibit a sharp increase with irradiation dose of the dislocation density which eventually approaches a saturation value. In cold-worked metals, however, the dislocation density drops with dose and approaches a saturation value similar or even identical to the one in the well-annealed counterpart. The observation that this saturation value is independent of the initial dislocation density has led several researchers [3.1-3.3] to suggest that the evolution of the dislocation network is the result of two competing processes, namely the generation of dislocations by loop growth and by climb of edge dislocation and the mutual annihilation of dislocations with opposite Burgers vectors.

These general ideas [3.2,3.4] provided the background for the empirical models of dislocation evolution proposed earlier, according to which the rate of change of the dislocation density $\rho(t)$ is given by

$$\frac{d\rho}{dt} = B\rho^m - A\rho^n \tag{3.1}$$

The logical choice for n is two since the annihilation of dislocations involves pairs with opposite Burgers vectors. For the production term, a plausible choice would be $m = 1$. However, Garner and Wolfer [3.4] provided heuristic arguments for $n = \frac{3}{2}$ and $m = \frac{1}{2}$. Unfortunately, the experimental data for $\rho(t)$ are not sufficiently accurate to determine the exponents m and n, and the choice of $m = 1$ and $n = 2$ appears to give an equally satisfactory correlation [3.2]. A review of the experimental results has been given earlier [3.4], and any discussion of those will be postponed to Section 3.6 where the measured dislocation densities are then compared with the theoretical predictions. Preceding this comparison, a model for the annihilation or recovery term $A\rho^2$ will be derived in Section 3.2, and Section 3.3 will deal with the derivation of the dislocation generation term $B\rho$. It will be found that both A and B are dependent on the dislocation density $\rho(t)$. Both processes require the climb motion of edge dislocations as a result of either an excess of self-interstitial absorption, or an excess of vacancy absorption or emission. At temperatures below about half of the melting point, the necessary climb motion can occur only if sinks with different point defect biases are present in the microstructure, where the bias is a measure of the preferential absorption of interstitials. Accordingly, we discuss in Section 3.4 the need and the extent of the bias variance necessary for the evolution of the dislocation structure to occur under irradiation. The comparison of the theory with the experimental data in Section 3.6 is limited to austenitic stainless steels irradiated in fast-neutron reactors, because the experimental irradiation conditions are well characterized, and the effects of the specimen surface are negligible. For irradiations performed with ion bombardment or electron beams, several additional complications exists such as a non-uniform defect production and a significant loss of dislocations to both the surface [3.3] and the portion of the specimen [3.5] not subject to radiation damage. For the present model to be applicable for ion bombardment or electron irradiations, these additional aspects must be included. However, they add little to the elucidation of the basic mechanisms which control the evolution of the dislocation density during high-temperature irradiations, and they will not be dealt with herein.

3.2. Dislocation Recovery

The reduction of the dislocation density in cold-worked metals by annealing involves the thermally activated climb of dislocations and the mutual annihilation of dislocations in dipole configurations. It is reasonable to assume then that the process of dipole annihilation takes place also under irradiation, and that this process is enhanced as a result of the radiation induced climb. In the following, an edge dislocation dipole is considered to consist of two nearly parallel segments of edge dislocations with parallel or anti-parallel Burgers vectors. The segment can either belong to line dislocations or to dislocation loops with a diameter significantly greater than the distance between the dislocations in the dipole.

Among the four different dipole configurations shown in Figure 3.1 which have edge dislocations of parallel or anti-parallel Burgers vectors and whose glide planes are separated by a distance h, only one pair will converge to a common glide plane when either interstitials or vacancies are preferentially absorbed at edge dislocations. For this one pair, called the converging dipole, h reduces with time, and if the segment can also glide under the mutual interaction force, annihilation will inevitably occur.

However, this requires that the interaction glide force overcomes a critical shear stress, τ_o. For a given τ_o this condition defines the maximum separation distance, h_{max}, from which a converging dipole may form. Using the glide force for an edge dislocation dipole [3.6], we obtain

$$\frac{\mu b}{2\pi(1-\nu)h_{max}} = \tau_o \tag{3.2}$$

where b is the Burgers vector, μ the shear modulus, and ν Poisson's ratio.

In alloys such as steels, dislocation motion is restricted by glide obstacles such as precipitates and by forest dislocations. Dislocation glide requires then the activation of Frank-Read sources. Accordingly, it is assumed that the critical shear stress τ_o for the glide motion of a dislocation segment is well approximated by the condition for the activation of a Frank-Read source of length l [3.6], *i. e.*

$$\tau_o = \frac{\mu b}{2\pi(1-\nu)l} \ln\left(\frac{l}{b}\right) \tag{3.3}$$

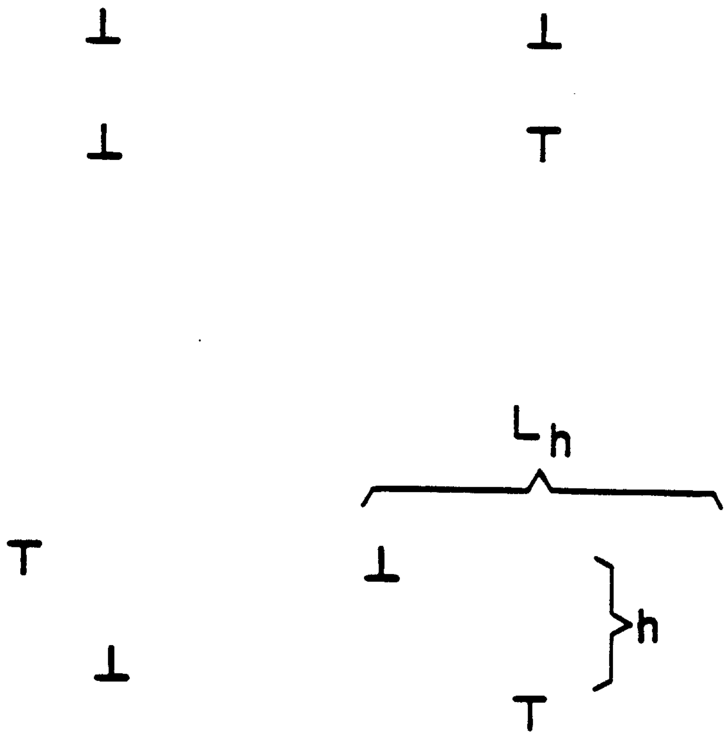

Figure 3.1. Edge dislocation dipole configurations.

Equations 3.2 and 3.3 define then the maximum separation distance h_{max} unless the dislocation density is so high that the average distance between parallel dislocation segments is less than this value.

Since $\frac{\rho}{12}$ is the dislocation density belonging to one glide system in the face centered cubic lattice, and since only one pair out of four will form a converging dipole, the average separation distance is $\frac{8}{\sqrt{\pi\rho/3}}$ between those dislocation segments capable of forming such a dipole. Hence,

$$h_{max} = \min\left[\frac{8}{\sqrt{\pi\rho/3}}, \frac{l}{\ln(l/b)}\right] \tag{3.4}$$

Let us assume now that at any given moment, the total number of all converging dipoles with a separation distance of their glide planes between h and $h + dh$ and with a separation distance parallel to the glide planes of $\frac{L_h}{2}$ or less (see Figure 3.1) is given by $12\frac{1}{4}\left(\frac{\rho}{12}\right)^2 L_h\, dh$ for a given glide system. If $h \leq h_{max}$, the dipole will in fact assume a configuration close to its mechanical equilibrium and $L_h \cong 2h$. Furthermore, let $\tau(h)$ denote the lifetime of a converging dipole of initial separation h. Then the rate of dislocation annihilation is finally given by

$$A\rho^2 = \frac{1}{24}\rho^2 \int_b^{h_{max}} \tau^{-1}(h) h\, dh \tag{3.5}$$

where we have summed over all 12 glide systems, but divided by four because three out of four dipole configurations are not converging.

If $V(h)$ represents the climb velocity of one dislocation, then the converging dipole lifetime is

$$\tau(h) = \int_b^h \frac{dh'}{2V(h')} \tag{3.6}$$

The climb velocity

$$V(h) = \frac{\Omega}{b}\left[Z_i^d D_i C_i - Z_v^d D_v C_v + Z_v^d D_v C_v^d(h)\right] \tag{3.7}$$

is determined by the concentrations of vacancies, C_v, and interstitials, C_i, by their diffusion coefficients, D_v and D_i, and by the vacancy concentration, $C_v^d(h)$, in local thermodynamic equilibrium with the dislocation. According to Kroupa [3.7]

$$C_v^d(h) = C_v^{eq} \exp\left(\frac{Hb}{h}\right) \tag{3.8}$$

where C_v^{eq} is the equilibrium vacancy concentration in the defect-free lattice,

$$H = \frac{\mu\Omega}{2\pi(1-\nu)kT} \tag{3.9}$$

Ω is the atomic volume, and kT has the usual meaning. The concentrations C_v and C_i can be obtained from two rate equations discussed in Section 3.5, and $V(h)$ can be written as

$$\begin{aligned} V(h) =& \frac{\Omega}{b}\left[\frac{Z_i^d}{Z_v^d} - \frac{\bar{Z}_i}{\bar{Z}_v}\right] Z_v^d D_v \Delta C_v + \frac{\Omega}{b} D_v Z_v^d C_v^{eq}\left[\exp\left(\frac{Hb}{h}\right) - 1\right] \\ =& V_R + V_T\left[\exp\left(\frac{Hb}{h}\right) - 1\right] \end{aligned} \tag{3.10}$$

The bias factors Z_i^d and Z_v^d contained in Equations 3.7 and 3.10 account for the effect of stress-induced migration on the absorption rate of interstitials and vacancies at edge dislocations, respectively. They are characteristic parameters of the type of sink under consideration.

Equation 3.10 shows that the climb velocity under irradiation can be separated into a radiation-induced part, V_R, and a thermally activated part proportional to V_T. The first part is proportional to excess vacancy concentration due to irradiation, ΔC_v, and the net bias, the expression in the bracket. This net bias is only different from zero when the sink-averaged bias factors, $\bar{Z}_i$ and $\bar{Z}_v$ are different from the dislocation bias factors, Z_i^d and Z_v^d; and this would require the presence of sinks other than dislocations. However, it will be shown in Section 3.4, that there exists a variance in the dislocation bias factors, and V_R will have to be modified. The modified V_R no longer vanishes when the sink structure consists only of dislocations.

With the expression for $V(h)$, the dipole lifetime defined by Equation 3.6 can now be evaluated. However, to obtain an analytical result, the following approximation must be made. Whenever the exponential term $\exp\left(\frac{Hb}{h'}\right)$ is large, the climb velocity makes the least contribution to $\tau(h)$. Conversely, only for large values of h' will the thermally activated climb velocity contribute significantly to $\tau(h)$. In this case, $\exp\left(\frac{Hb}{h'}\right) \cong 1 + \frac{Hb}{h'}$ and

$$\begin{aligned}\tau(h) &\cong \frac{1}{2}\int_b^h \frac{dh'}{(V_R + V_T Hb/h')} \\ &= \frac{h}{2V_R} - \frac{V_T Hb}{2V_R^2}\ln\left[1 + \frac{V_R h}{V_T Hb}\right]\end{aligned} \tag{3.11}$$

The coefficient A for the dislocation annihilation rate is then given by

$$A \cong \frac{1}{12}V_T Hb \int_{x_o}^{x_1}\left[1 - \frac{1}{x}\ln(1+x)\right]^{-1} dx \tag{3.12}$$

where $x = \frac{V_R h}{V_T Hb}$, $x_o = \frac{V_R}{V_T H}$, and $x_1 = \frac{V_R h_{max}}{V_T Hb}$. No closed-form solution to this integral exists. However, two limiting cases can be evaluated easily. First, if $V_R \gg V_T$, then $\frac{1}{x}\ln x \ll 1$, and

$$A \cong \frac{1}{12}V_R h_{max} \tag{3.13}$$

Second, if $V_T \gg V_R$, then $x \ll 1$, and expanding $\frac{1}{x}\ln(1+x) \cong 1 + \frac{x}{2}$. In this case

$$A \cong \frac{1}{6} V_T H b \ln\left(\frac{h_{max}}{b}\right) \tag{3.14}$$

These two special cases represent the low and high temperature approximations, respectively. Because of the strong temperature dependence of self-diffusion and hence of V_T, the range of temperatures, where V_R and V_T are of the same order, is very narrow. As a result, we may simply add the expressions and obtain the approximation

$$A \cong \frac{1}{12} V_R h_{max} + \frac{1}{6} V_T H b \ln\left(\frac{h_{max}}{b}\right) \tag{3.15}$$

suitable for all temperatures. Note that V_R depends on the dislocation density $\rho(t)$.

3.3. Dislocation Generation

The dislocation density may increase during irradiation as a result of two processes: first by the formation and growth of dislocation loops, and second by the climb of dislocation segments pinned by obstacles. The latter process is exemplified by the Bardeen-Herring source [3.6].

Evaluation of the average rate of increase for the dislocation density by these processes follows. Dislocation loops can grow under irradiation to an average maximum radius R_m, whereupon they may unfault and become part of the network or coalesce with other loops or dislocations. If V represents the mean climb velocity, the average lifetime of a dislocation loop is $\tau = \frac{R_m}{V}$. Assuming that $\bar{R} = \frac{R_m}{2}$ is the average loop radius at any instant, the dislocation density due to loops is $\rho = \pi R_m N_l$ averaged over a significantly large volume containing a density of N_l loops.

The rate of increase of this dislocation density is then given by

$$B\dot{\rho} = \frac{2\pi \dot{R}_m N_l}{\tau} = \frac{\rho V}{\bar{R}} \qquad (3.16)$$

To evaluate the change in dislocation density from the climb of edge dislocations, consider in Figure 3.2 a bowed-out dislocation segment pinned at two centers separated by a distance l, the mesh length. To remain pinned under a current of point defects constant along the arc, the point defects must pipe-diffuse towards the center of the arc. It is assumed that pipe-diffusion can occur readily such that the dislocation segment maintains always its minimum line energy commensurate with the area F required to accommodate the accumulated atoms. The rate of increase for F is given by $\frac{dF}{dt} = VL$ where V is the climb velocity of an unpinned segment and L is the arc length of the bowed-out segment. As the dislocation segment continues to bow-out, it encounters eventually new pinning centers or it annihilates with another edge dislocation segment. When new pinning centers are encountered, the bowed-out segments is subdivided into new segments with an original mesh length of average value l. The process of regeneration repeats itself with each segment. If τ denotes then the average time of regeneration and L_m the maximum arc length a segment can reach, then the rate of dislocation increase in a volume containing N_d segments is given by

$$B\rho = \frac{N_d(L_m - l)}{\tau} \qquad (3.17)$$

The regeneration time may be obtained from

$$\tau = \int_0^{\tau} dt = \frac{1}{V} \int_l^{L_m} \frac{dF}{dL} \frac{dL}{L} \tag{3.18}$$

With the help of Figure 3.2 it is easy to derive the following geometrical relationships

$$L = \psi R, \qquad l = 2R \sin\left(\frac{\psi}{2}\right) \tag{3.19}$$

and

$$F = \frac{1}{2}\left[LR - l\left(R^2 - \frac{l^2}{4}\right)^{1/2}\right] \tag{3.20}$$

From these it is possible to obtain

$$\tau = \frac{l}{2V} \int_0^{\psi_m} \frac{1 - \left(\frac{\psi}{2}\right) \cot\left(\frac{\psi}{2}\right)}{\psi \sin\left(\frac{\psi}{2}\right)} \, d\psi \tag{3.21}$$

The dislocation density at any given instant averaged over a sufficiently large volume is given by

$$\rho = \frac{N_d}{L_m - l} \int_l^{L_m} L \, dL \tag{3.22}$$

if it is assumed that segments bowed out to any length between l and L_m are equally abundant. Equation 3.22 can also be written as

$$\rho = \frac{N_d}{L_m - l} \int L \frac{dL}{d\psi} \, d\psi = \frac{N_d l^2}{L_m - l} \int_0^{\psi_m} \frac{\psi^2 \left[\left(\frac{\psi}{2}\right) - \cot\left(\frac{\psi}{2}\right)\right]}{8 \sin^2\left(\frac{\psi}{2}\right)} \, d\psi$$

We may use this equation to eliminate the segment density N_d from Equation 3.17, use Equation 3.21 to eliminate τ, and obtain

$$B\rho = \frac{C\left(\frac{L_m}{l}\right) V \rho}{l} \tag{3.23}$$

where

$$C^{-1}\left(\frac{L_m}{l}\right) = \left(\frac{l}{L_m - l}\right)^2 \int_0^{\psi_m} \frac{1 - \left(\frac{\psi}{2}\right)\cot\left(\frac{\psi}{2}\right)}{\psi \sin\left(\frac{\psi}{2}\right)} d\psi \int_0^{\psi_m} \frac{2\psi - \psi^2 \cot\left(\frac{\psi}{2}\right)}{8\sin^2\left(\frac{\psi}{2}\right)} d\psi$$

and $\psi_m = \frac{L_m}{R(L_m)}$. The numerical evaluation of $C\left(\frac{L_m}{l}\right)$ is shown in Figure 3.3. If the segment bows out to a half-circle, then $L_m = \frac{\pi l}{2}$, $\psi_m = \frac{\pi}{2}$, and $C\left(\frac{\pi}{2}\right) = 1.355$. Except for values of L_m close to l, the coefficient C is of order one, and this approximate value will be used in the following.

In the above derivation, it was also assumed that the climb velocity V of the bowed-out dislocation segment is not dependent on the radius of curvature, R. However, at elevated temperatures when $V_T \cong V_R$, the vacancy concentration in thermodynamic equilibrium with the bowed-out segment is given by [3.6]

$$C_v^b = C_v^{eq} \exp\left[-\frac{\mu\Omega}{2\pi(1-\nu)kT}\frac{b}{R}\ln\frac{R}{1.86b}\right] \tag{3.24}$$

when the bow-out is due to excess interstitial absorption. For the case of excess vacancy absorption, the sign in the exponential is reversed. Figure 3.4 shows the ratio C_v^b/C_v^{eq} evaluated for nickel according to Equation 3.24. It is seen that $C_v^b - C_v^{eq}$ becomes increasingly negative as R decreases. As a result, the current of thermal vacancies to the bowed-out segment may cancel the excess interstitial flow at elevated temperatures, and the net climb velocity becomes zero. The minimum value of C_v^b is reached when $R = \frac{l}{2}$ corresponding to a "minimum" climb velocity of

$$V_m = V_R + V_T\left[\exp\left(-\frac{\mu\Omega}{\pi(1-\nu)kT}\frac{b}{l}\ln\frac{l}{3.6b}\right) - 1\right] \tag{3.25}$$

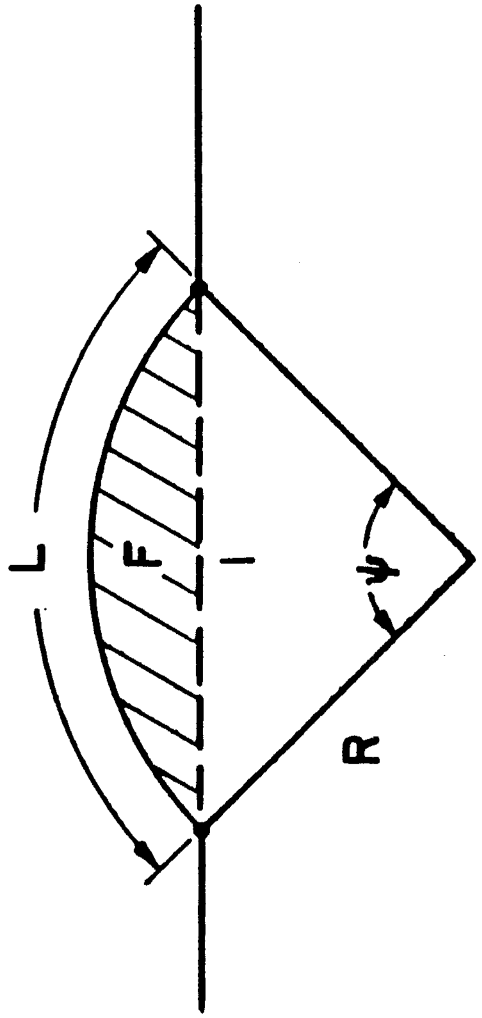

Figure 3.2. Geometric parameters for a Bardeen-Herring source.

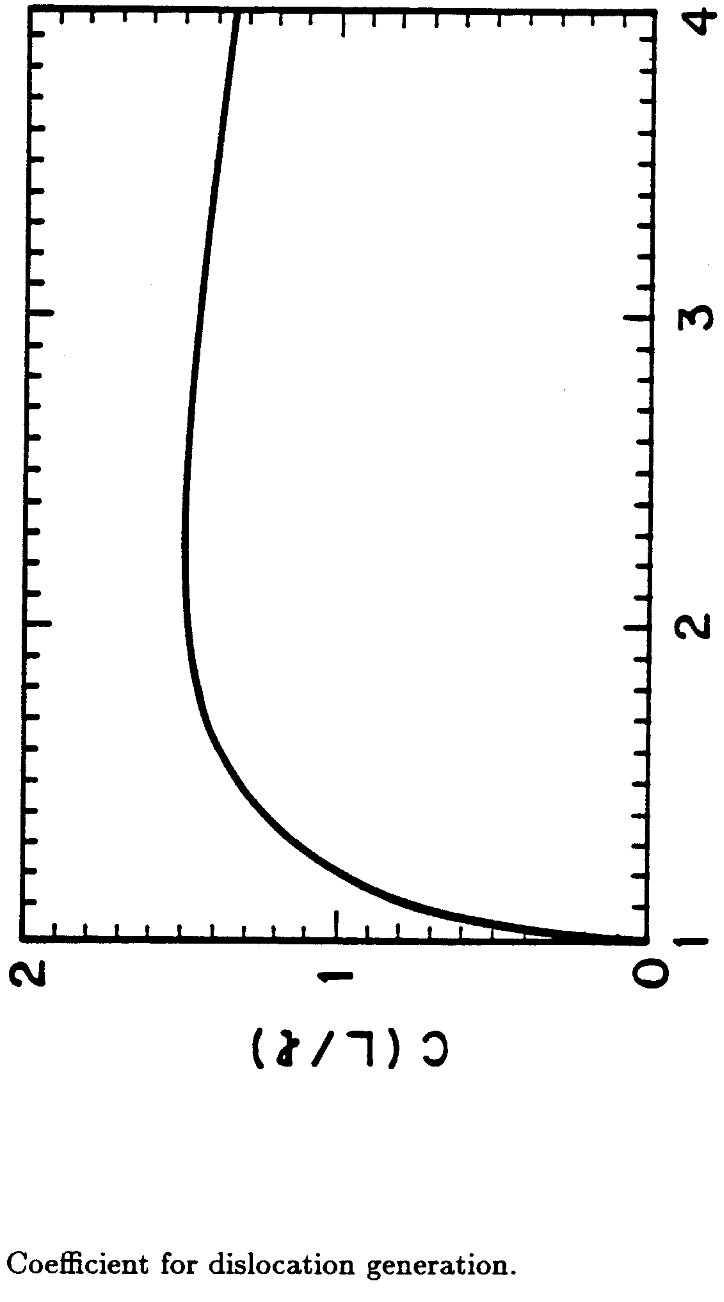

Figure 3.3. Coefficient for dislocation generation.

If this climb velocity is zero or negative, the dislocation generation by the Bardeen-Herring process is no longer possible and $B = 0$. Accordingly, the rate of dislocation generation is approximately given by

$$B\rho = \begin{cases} \frac{\rho V_m}{l}, & \text{for } V_m > 0; \\ 0, & \text{for } V_m \leq 0. \end{cases} \tag{3.26}$$

In the low temperature ($\leq 300^oC$) range where loops contribute significantly to the dislocation density, the rate of dislocation generation is seen to be given by similar expressions, *i. e.* by Equations 3.16 and 3.26. The major difference lies merely in the characteristic length parameters, the average loop radius, $\bar{R}$ in the case of loops, and the average distance between pinning obstacles, l in the case of network dislocations.

3.4. Bias Variance

The radiation-induced part of the climb velocity, V_R in Equation 3.10, is proportional to the net bias parameter $\frac{Z_i^d}{Z_v^d} - \frac{\bar{Z}_i}{\bar{Z}_v}$. It is already mentioned in Section 3.2, that this parameter vanishes if only one type of sink is present.

In cold-worked steels, void formation is suppressed for an extended period of irradiation. Nevertheless, during this period the dislocation density has been observed to change dramatically even at temperatures where V_T is negligibly small. It can therefore be concluded that V_R does not vanish even though the net bias is zero when only dislocations are present as sinks.

This paradox can be resolved by taking into account the bias variance of edge dislocations. This variance arises from the partial cancellation of the long-range stress fields of individual dislocations when they are arranged in

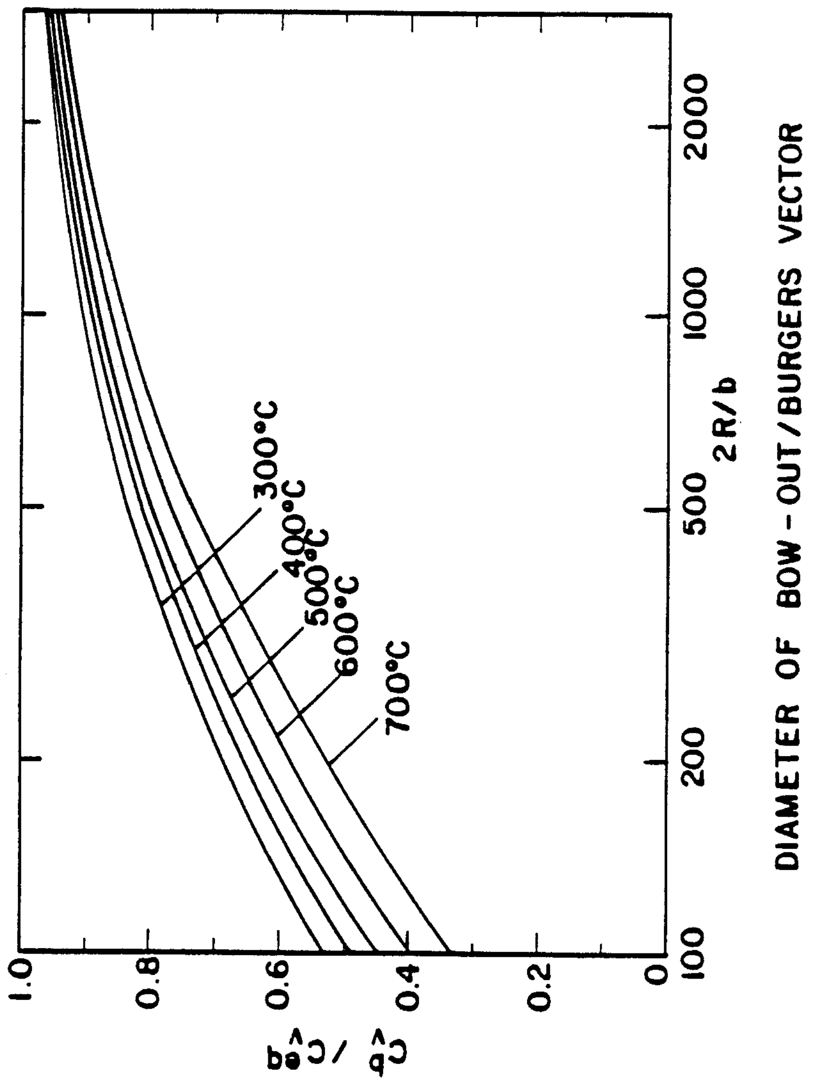

Figure 3.4. Ratio of vacancy concentration in equilibrium with an interstitial dislocation loop and with a straight edge dislocation.

dense groups. The bias of an individual edge dislocation depends to some degree on the proximity of other edge dislocations and on the directions of their Burgers vector. Wolfer *et al.* [3.8] have estimated this bias variance by considering narrowly spaced dislocation multipoles. It was found that the bias of an edge dislocation dipole can be as low as half the value for an isolated edge dislocation, and that dislocations in higher-order multipole configurations have even lower bias values. To take into account this bias variance, the net bias

$$(1+z)\frac{Z_i^d}{Z_V^d} - \frac{\bar{Z}_i}{\bar{Z}_V} \tag{3.27}$$

is assigned to the individual edge dislocation and z is assumed to be a normally distributed random variable. Then, the average climb velocity V_R remains proportional to $(\frac{Z_i^d}{Z_v^d} - \frac{\bar{Z}_i}{\bar{Z}_v})$, but Z_i^d and Z_v^d are to be interpreted as mean values for the dislocation bias factors. Furthermore, both positive and negative climb directions contribute to the average climb velocity V_R. However, with regard to increasing the dislocation line length through climb or with regard to annihilation, the direction of climb does not matter, and we must therefore take the average of the absolute climb velocities. This average is given by integrating over the assumed normal distribution for the bias variance with the result

$$\begin{aligned}\bar{V}_R =& \frac{\Omega}{b} Z_v^d D_v \Delta C_v \int_{-\infty}^{\infty} dz \left| \frac{Z_i^d}{Z_v^d}(1+z) - \frac{\bar{Z}_i}{\bar{Z}_v} \right| (\sqrt{2\pi}\varsigma)^{-1} \exp\left(\frac{-z^2}{2\varsigma^2}\right) \\ =& \frac{\Omega}{b} Z_v^d D_v \Delta C_v \left[\frac{Z_i^d}{Z_v^i}\left(1+\varsigma\sqrt{2\pi}\right) - \frac{\bar{Z}_i}{\bar{Z}_v} \right]\end{aligned} \tag{3.28}$$

is to be substituted for V_R in both Equations 3.25 and 3.16.

The standard deviation ς of the dislocation bias is expected to depend on the dislocation density itself. In a well-annealed material, most dislocations in narrowly spaced dipole configurations have been annihilated by the very process described in Section 3.2. The remaining edge dislocations possess then the full bias of an isolated dislocation, and ς is close to zero. In contrast, in a heavily cold-worked material, many dislocations are part of dense tangles, resulting in a large bias variance. If we assume for this case that $\varsigma \cong \frac{1}{2}$, and $\varsigma \cong 0$ for the annealed case,

$$\varsigma = 0.5[1 - \exp(-\lambda\rho)] \tag{3.29}$$

will provide a plausible dependence of the bias variance on the dislocation density. The choice of $\lambda = 10^{-15}$ m^2 assures that the bias variance becomes negligible for $\rho \leq 10^{15}$ m^{-2} but approaches its maximum value for $\rho \geq 10^{16}$ m^{-2}.

3.5. Rate Equations For Point Defects

The average concentrations of vacancies and interstitials, C_v and C_i, in a material subject to a constant rate of generation P by a fast neutron flux are given by the two rate equations

$$P - \kappa D_v C_v D_i C_i - D_i C_i \sum_s N^s A^s Z_i^s = 0 \tag{3.30}$$

$$P - \kappa D_i C_i D_v C_v - D_v \sum_s (C_v - C_v^s) N^s A^s Z_v^s = 0 \tag{3.31}$$

where

$$\kappa = \frac{4\pi r_c}{\Omega}\left(\frac{1}{D_v} + \frac{1}{D_i}\right) \tag{3.32}$$

is the recombination coefficient and r_c the recombination radius for a Frenkel pair. N^s is the density of sinks of type "s", A^s a geometrical factor characteristic of this sink type, and Z_i^s and Z_v^s are the bias factors of this sink type for interstitial and vacancy absorption, respectively.

The solution of the rate equations for D_iC_i and D_vC_v are

$$D_vC_v = D_v\left(\frac{\bar{Z}_i}{\bar{Z}_v}\Delta C_v + \bar{C}_v^{eq}\right) \tag{3.33}$$

$$D_iC_i = D_v\Delta C_v \tag{3.34}$$

where

$$\bar{Z}_{i,v} = \frac{\sum_s N^s A^s Z_{i,v}^s}{\sum_s N^s A^s} \tag{3.35}$$

are the sink-averaged bias factors and

$$\bar{C}_v^{eq} = \frac{\sum_s N^s A^s Z_v^s C_v^s}{\sum_s N^s A^s Z_v^s} \tag{3.36}$$

is the sink-averaged thermal vacancy concentration. The vacancy concentration in local thermodynamic equilibrium with the sink of type "s" is denoted by C_v^s.

The excess vacancy concentration ΔC_v is given by

$$\Delta C_v = \frac{\bar{N}\bar{Z}_v}{2\kappa D_v}\left[\left(M^2 + L\right)^{1/2} - M\right] \tag{3.37}$$

where

$$M = 1 + \frac{\kappa D_v \bar{C}_v^{eq}}{\bar{N}\bar{Z}_i} \tag{3.38}$$

and

$$L = \frac{4P\kappa}{\bar{Z}_i \bar{Z}_v \bar{N}^2} \tag{3.39}$$

Here $\bar{N} = \sum_s N^s A^s$ is the total sink strength.

3.6. Results And Discussion

The following predictions for the evolution of the network dislocation density are carried out for 316 austenitic stainless steel and the ferrite phase of ferritic steel. The dislocation bias factors Z_i^d and Z_v^d are evaluated with the formulas given by Sniegowski and Wolfer [3.9]. An example of the dislocation bias factors for 316 stainless steel is given in Figure 3.5. Properties used are listed in Table 3.1. With the exception of the mesh length, all other properties in Table 3.1 are based on measured or theoretically determined values. The mesh length was selected such that the saturation dislocation density will be 6×10^{14} m^2 for an irradiation temperature of 500°C; this density corresponds to experimentally observed saturation densities in 316 stainless steel at about 500°C. The average point defect concentrations produced during irradiation are evaluated with rate theory as outlined in a previous section. A density of cavity embryos is assumed to exist from the beginning. The density of cavities depends on temperatures and is assumed to be equal to the terminal void number density as observed experimentally. These cavities are allowed to grow according to rate theory which results in void swelling and an increase in the cavity sink strength. The details of void swelling are discussed in a later chapter.

The saturation dislocation density is found to be independent of temperature between 300°C and 500°C for 316 stainless steel, (300°C and 400°C for ferrite phase) but begins to decrease with increasing temperature above about 550°C for 316 stainless steel (450°C for ferrite phase). Figure 3.6 shows the dislocation saturation density for 316 stainless steel as a function of temperature for two different mesh length assumptions. The theoretical predictions compare quite well with observed experimental densities [3.4] as shown in the figure; error bars are shown when given in the references. As can be seen the error in experimental measurement can be quite large. The reasons for the decrease in saturation density as temperature increases is the increasing contribution of thermally induced climb as self-diffusion becomes important. The thermally induced climb is of course responsible for the high temperature recovery of cold-worked materials. This recovery can also be described with the present theory by turning off the point defect production rate. Figure 3.7 shows the results for thermal recovery of the dislocation density in cold-worked 316 austenitic stainless steel. It is seen that the dislocation recovers to a value of 5×10^{13} m^{-2}, typical of annealed material, within about 12 days at an annealing temperature of 700°C. Annealing also occurs at 600°C; but it becomes increasingly insignificant at lower temperatures. These predictions are in general agreement with observation, though no dislocation density measurements have been found in the literature.

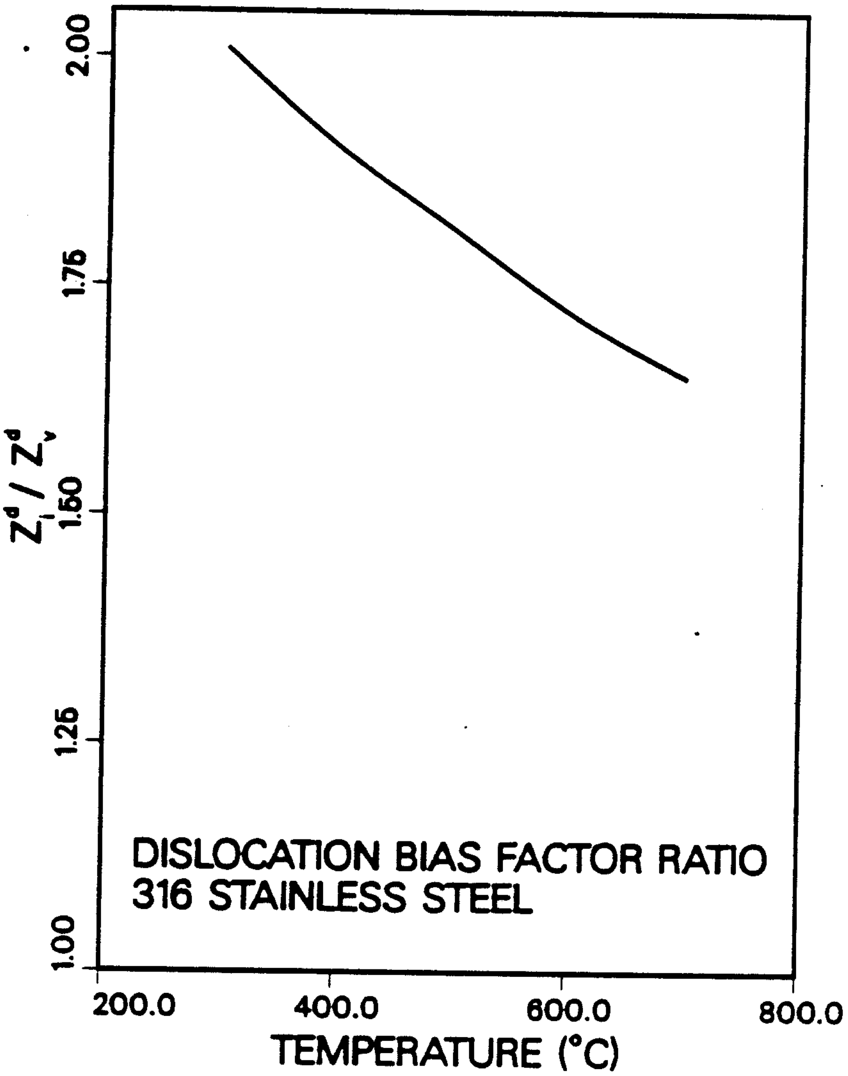

Figure 3.5. Dislocation bias factor ratio for 316 stainless steel based on model by Sniegowski and Wolfer [3.9].

Table 3.1. Material Parameters

	316 SS	ferrite
Displacement rate, dpa/sec	10^{-6}	10^{-6}
Cascade efficiency	0.1	0.1
Lattice parameter a_o, nm	0.3639	0.2866
Burgers vector, nm	0.2573	0.2482
Shear Modulus, GPa	82.95	80.65
Poisson's ratio	0.264	0.254
Vacancy migration energy, J	1.92×10^{-19}	2.02×10^{-19}
Vacancy formation energy, J	2.88×10^{-19}	2.46×10^{-19}
Pre-exponential factor D_v^o, m^2/s	1.29×10^{-6}	4.46×10^{-5}
Vacancy relaxation volume, Ω	-0.2	-0.5
Interstitial relaxation volume, Ω	1.5	0.85
Vacancy shear polarizability, J	-2.4×10^{-18}	-2.4×10^{-18}
Interstitial shear polarizability, J	-2.535×10^{-17}	-2.535×10^{-17}
Initial dislocation densities, m^{-2}		
for annealed	4×10^{12}	4×10^{12}
for cold-worked	7×10^{15}	7×10^{15}
Mesh length l, μm	0.4	0.4

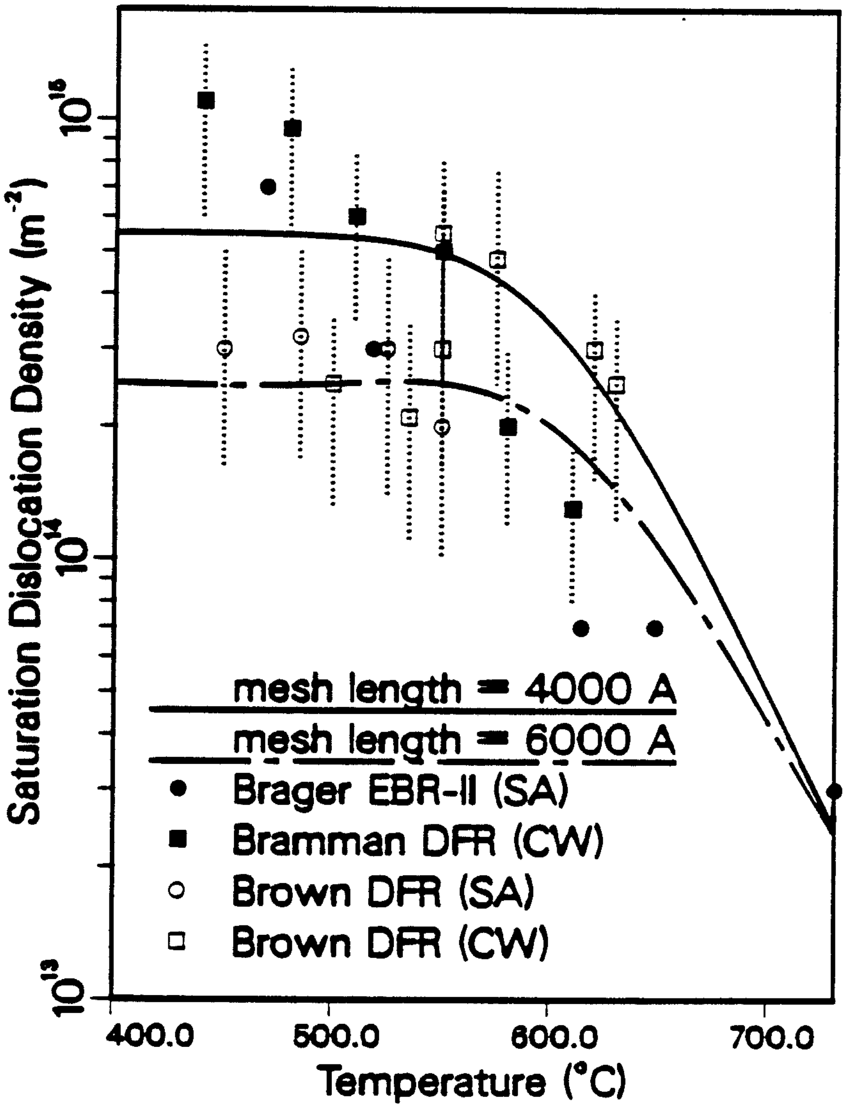

Figure 3.6. Saturation dislocation densities in type 316 stainless steel irradiated to doses greater than 20 dpa in breeder reactors.

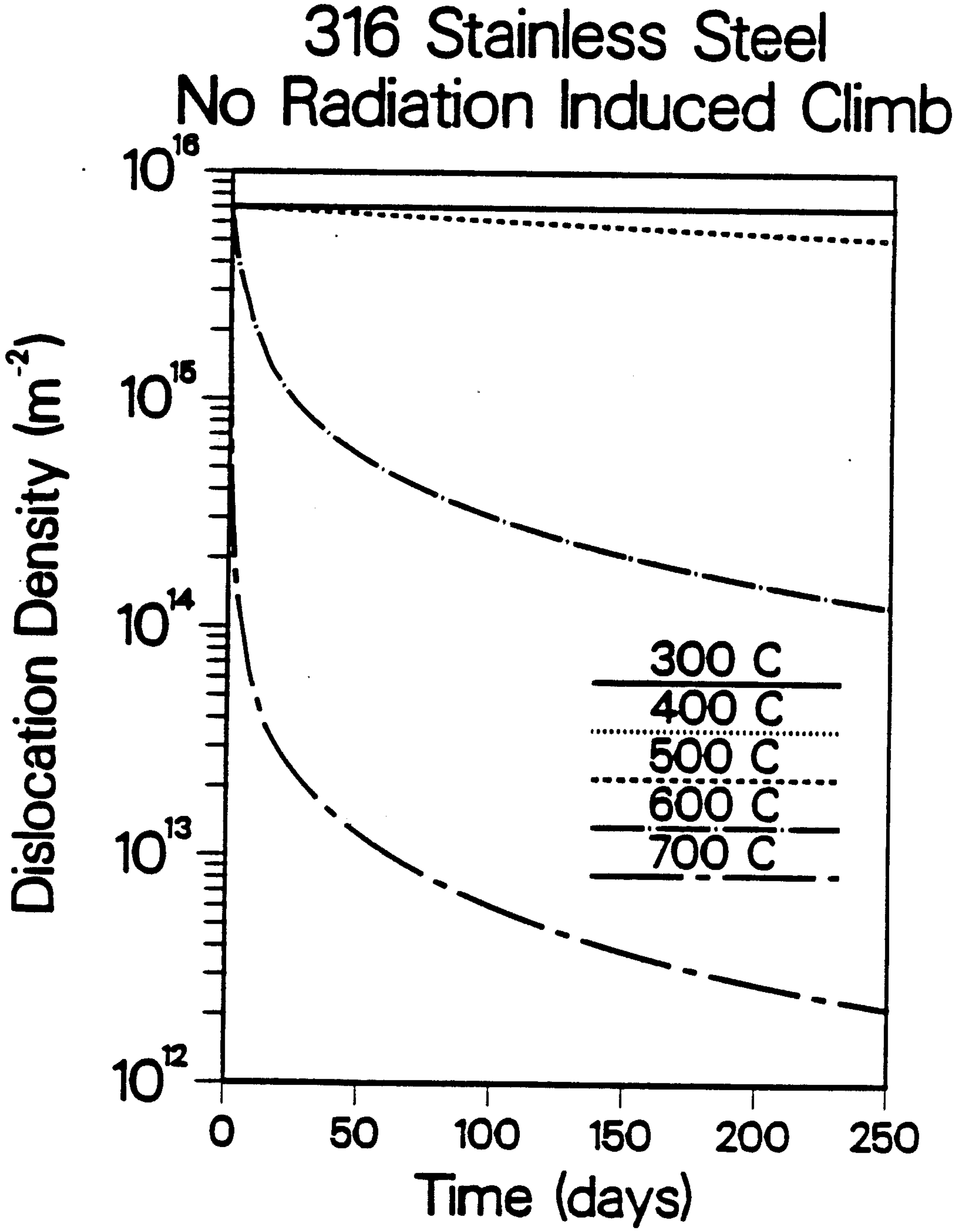

Figure 3.7. Predicted recovery of the dislocation density in initially cold-worked 316 stainless steel due to thermal annealing. The 400°C curve is coincident with the 300°C curve.

Figures 3.8 and 3.9 show the predictions for the dislocation evolution for 316 austenitic stainless steel and ferrite phase. The time evolution is given in units of dpa, where the dpa rate is 1×10^{-6} dpa/sec. The helium/dpa ratio of 20 appm He/dpa is typical of fusion reactors. Comparison to experimentally measured dislocation densities [3.4] in the transient region is very limited but agrees quite well considering the uncertainty in the experimental measurements.

The model developed for the evolution of the network dislocation density reproduces remarkably well the experimental observations. This is significant for two major reasons. First, the materials parameters required are very fundamental and reasonably well known. Therefore, with the exception of the mesh length parameter l and the bias variance ς, no other parameters required adjustments. The value chosen for l, namely 400 nm, is also reasonably close to the mesh length of bowed-out dislocations observed in micrographs of irradiated steels.

The second important implication of the successful model is that the complex dislocation structure and its evolution can in fact be understood in terms of two simple processes: the Bardeen-Herring process of climb in a material with supersaturation of point defects; and the climb-induced annihilation of dislocation dipoles.

The fact that dislocation loops have not been explicitly considered in the present model constitutes both one of its strengths and its weaknesses.

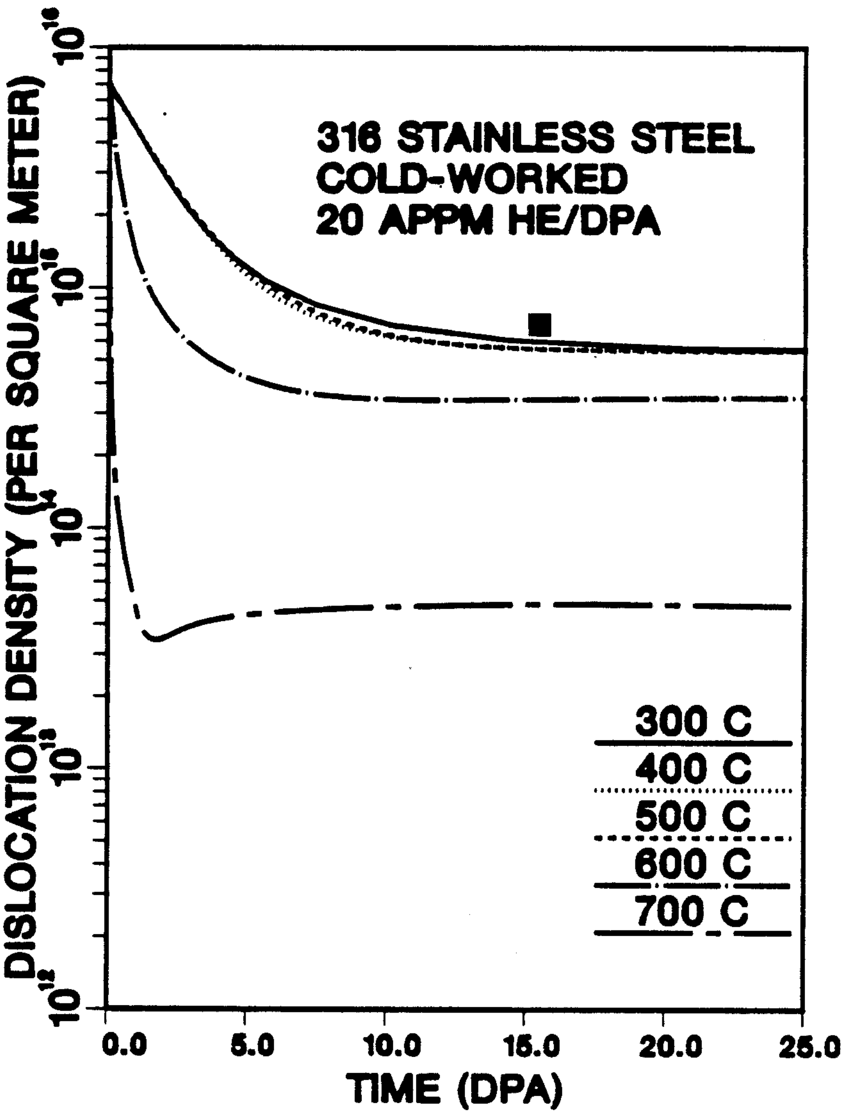

Figure 3.8a. Dislocation density evolution with irradiation time for cold-worked 316 stainless steel at a displacement rate of 10^{-6} dpa/sec and 20 appm He/dpa. The results for 0.6 appm He/dpa show similar results except the steady state density for 700°C is approximately half as high. The one data point [3.1] was taken at an irradiation temperature of 500°C and is within a factor of 2 of the theoretical result.

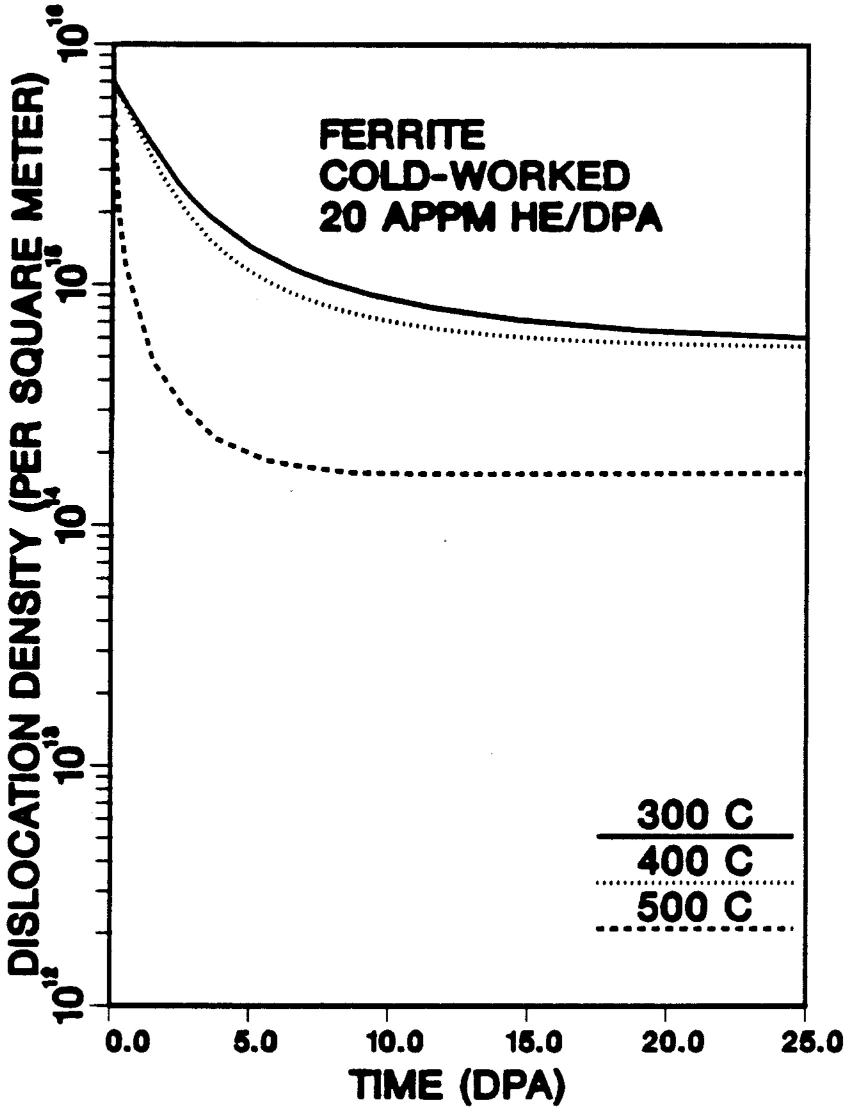

Figure 3.8b. Dislocation density evolution with irradiation time for cold-worked ferrite phase at a displacement rate of 10^{-6} dpa/sec and 20 appm He/dpa. The results for 0.6 appm He/dpa show similar results.

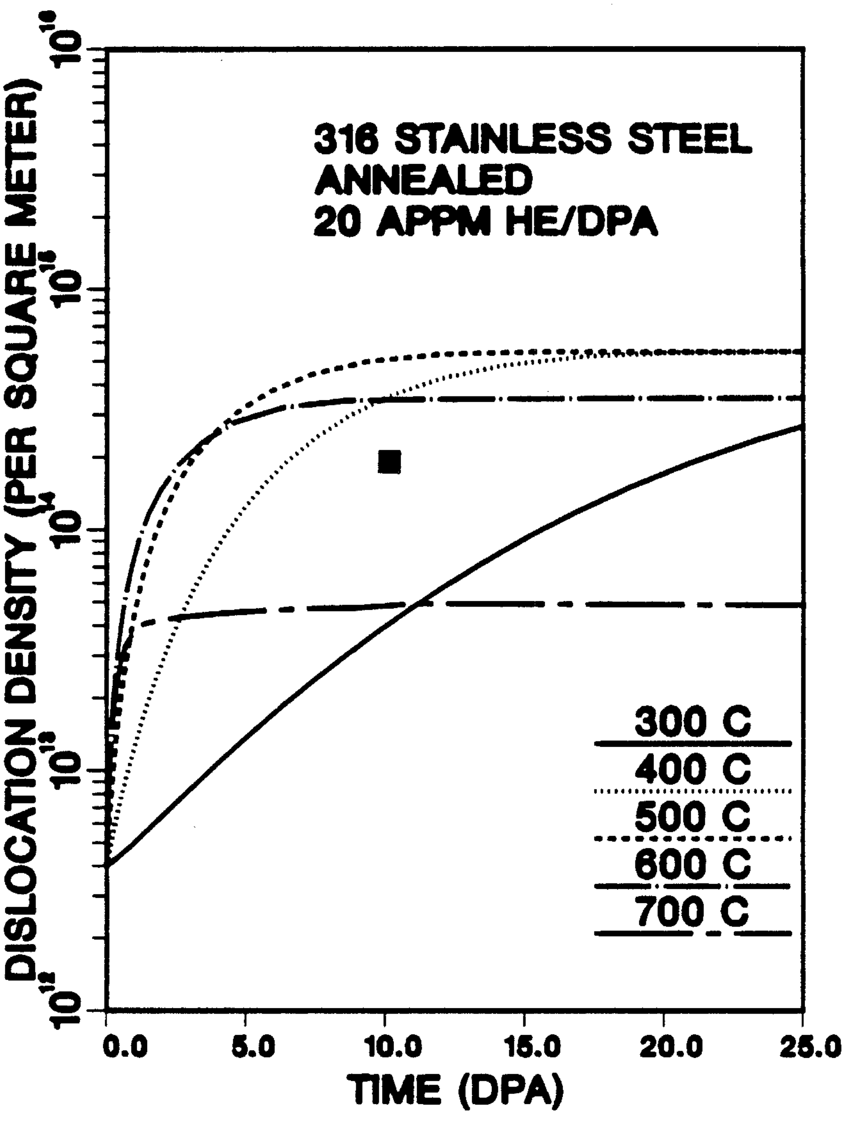

Figure 3.9a. Dislocation density evolution with irradiation time for annealed 316 stainless steel at a displacement rate of 10^{-6} dpa/sec and 20 appm He/dpa. The results for 0.6 appm He/dpa show similar results except the steady state density for 700°C is approximately half as high. The one data point [3.1] was taken at an irradiation temperature of 500°C and is within a factor of 3 of the theoretical result.

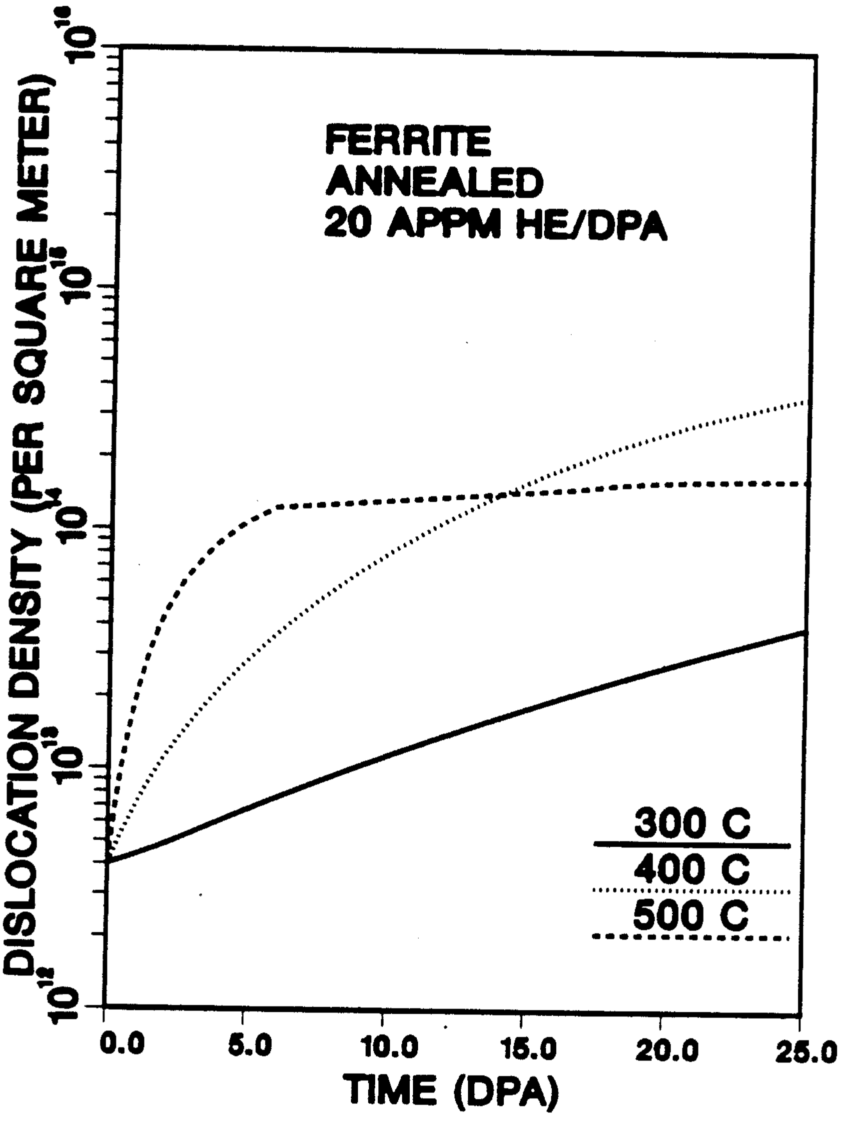

Figure 3.9b. Dislocation density evolution with irradiation time for annealed ferrite phase at a displacement rate of 10^{-6} dpa/sec and 20 appm He/dpa. The results for 0.6 appm He/dpa show similar results.

Large loops increase their line length very much like a bowed-out dislocation segment, independent of the presence or absence of a stacking fault. When the stacking fault energy is low, the stacking fault does not contribute significantly to the line tension and to the vacancy concentration C_v^b in Equation 3.24. Therefore, dislocation loops and bowed-out edge dislocations can indeed be treated as one at higher temperatures.

However, when dislocation loops are small, it is no longer adequate to model them as edge dislocation segments. In this case, loops and network dislocations must be considered as different sinks, and their evolution will have to be described by different models. Based on experimental observation, the loop density increases and their size decreases with decreasing irradiation temperature. It is therefore expected, that small dislocation loops are present at an irradiation temperature of 300°C, and that these loops make a major contribution to the total dislocation density. Accordingly, the present model should not be applied to the entire dislocation structure in materials containing a high density of small dislocation loops.

References

[3.1.] Brager, H. R., Garner, F. A., Gilbert, E. R., Flinn, J. E., and Wolfer, W. G., *Radiation Effects in Breeder Structural Materials* (Editors: M. L. Bleiberg and J. W. Bennett), page 727, American Institute of Mining, Metallurgical, and Petroleum Engineers, New York (1977).

[3.2.] Wolfer, W. G., *Journal of Nuclear Materials* **90** 175 (1980).

[3.3.] Ignata, N., Kohyama, A., and Nomura, S., *ASTM STP 725* 627 (1981).

[3.4.] Garner, F. A. and Wolfer, W. G., *ASTM STP 782* 1073 (1982).

[3.5.] Farrell, K., Packan, N. H., and Houston, J. T., *Radiation Effects* **62** 39 (1982).

[3.6.] Hirth, J. P. and Lothe, J., *Theory of Dislocations, 2^{nd} Edition*, John Wiley and Sons, New York (1982).

[3.7.] Kroupa, F., *Czechoslovakian Journal of Physics* **B17** 220 (1967).

[3.8.] Wolfer, W. G., Ashkin, M., and Boltax, A., *ASTM STP 570* 233 (1975).

[3.9.] Sniegowski, J. J. and Wolfer, W. G., *Proceedings of the Topical Conference of Ferritic Alloys for Use in Nuclear Energy Technology* (Editors: J. W. Davis and D. J. Michel) page 579, The Metallurgical Society AIME, Warrendale (1984).

Chapter 4

MODELING OF VOID SWELLING IN IRRADIATED STEELS

4.1. Introduction

Recent analysis [4.1] of swelling data for austenitic stainless steels has revealed that the steady state swelling rate is nearly independent of temperature for temperatures of interest in fusion and fission reactors. Furthermore, the swelling rate appears to approach an ultimate value of about 1 %/dpa independent of the initial microstructure and independent of the alloy composition. These observations are in contradiction with earlier analyses. In order to theoretically understand swelling behavior, the physical processes of swelling have been reexamined from first principles and a rate theory model of swelling has been developed. Additionally, initial experimental results [4.2] of the swelling of ferritic steel suggest a much lower swelling rate for this class of steel. However, long term exposure results have not yet been completed. In an effort to predict the steady state swelling behavior of ferritic steels, the rate theory model of swelling is applied to the ferrite phase.

The rate theory of swelling is basically concerned with the calculation of the net flux of point defects to the surface of a void or bubble. Knowing the net flux to a cavity surface, the growth rate can be calculated. The major unknowns to be determined in this rate theory are the sink strengths and the bias factors of cavities and dislocations. However, as a result of the continuous helium production, other growth mechanisms are also possible and are incorporated in the present model. These gas-driven mechanisms are as follows.

1. Thermal vacancy exchange. Due to differences in the equilibrium vacancy concentrations between the cavity surface and the bulk material, thermally generated vacancies will tend to flow either toward or away from cavity surfaces.
2. Loop punching. Given a sufficiently high pressure and energetically favorable conditions, it has been shown [4.3] that an interstitial platelet can be punched out from the bubble surface.
3. Self-Interstitial Emission. Given high enough pressure within a bubble, a self-interstitial can be emitted from a bubble surface.

The results of the model presented herein do not accurately match experimentally determined swelling behavior. This is to be expected because of many simplifying assumptions made. For example, the only sinks modeled are cavities and dislocations. The nucleation of cavities is not modeled; rather, a constant number of cavities is assumed with a uniform radius which increases with time. It is assumed that all of the helium is equally partitioned to the cavities. Even though certain aspects of the physical processes are not modeled, important features of swelling behavior result. These features include a steady state swelling rate roughly independent of temperature, a significantly lower swelling rate for the ferrite phase in comparison to austenitic stainless steels, and an incubation-type period early in life which depends on the helium concentration and pressure. Temperature independent steady state swelling rate and an incubation period have been reported [4.1] in experimental results; and helium is considered to be a major factor in causing early nucleation of cavities in steels exposed to neutrons.

4.2. Athermal Growth Processes

Two different athermal growth mechanisms are considered in the model: 1) self-interstitial emission and 2) interstitial loop punching. These two mechanisms are activated only at relatively high pressures.

Glasgow and Wolfer [4.4] concluded that self-interstitial emission is energetically favored over helium interstitial emission. The pressure required for bubble growth by self-interstitial emission may be estimated as follows. Suppose that the rate of helium generation or implantation is $\dot{P}_{He}$ (per metal atom and per second), and that there are already N helium bubbles per unit volume of average radius R. Further assume that a stationary condition has been reached such that each new helium atom generated or implanted will after some time be trapped at one of the already existing bubbles. In addition, the ratio of helium atoms to vacancies in the bubble η shall remain constant, and any newly acquired helium atom in a bubble induces the emission of a self-interstitial. Then the following relationship is valid.

$$\dot{P}_{He} = \eta 4\pi R N D_I C_I^o \tag{4.1}$$

Here, $D_I = D_I^o \exp(-E_I^m/kT)$ is the self-interstitial diffusion coefficient and C_I^o is the concentration of self-interstitials in local thermodynamic equilibrium with the bubble and is given by [4.4]

$$C_I^o = \exp\left[-\frac{E_I^f + U_I}{kT} + \frac{z(y_o)y_o\Omega}{\Omega_{He}} - \frac{2\gamma\Omega}{RkT}\right] \tag{4.2}$$

By neglecting the interaction energy of the self-interstitial with the bubble U_I in Equation 4.2 and using Equations 4.1 and 4.2, the following relationship exists and when satisfied results in self-interstitial emission.

$$p\Omega \geq \frac{2\gamma\Omega}{R} + E_i^f + E_i^m + kT\ln\left[\frac{\dot{P}}{\eta 4\pi RND_i^o}\right] \tag{4.3}$$

It is found [4.4] from this equation that the overwhelming contribution to the right hand side originates from E_i^f, the interstitial formation energy; and that p must be on the order of 10^{10} Pa for the condition to be satisfied. The other parameters included in the above equations are as follows: Ω is the atomic volume, γ is the cavity surface energy, R is the cavity radius, E_i^m is the interstitial migration energy, k is Boltzmann's constant, T is the temperature, D_i^o is the pre-exponential interstitial diffusion constant, $\dot{P}$ is the helium production rate, η is the ratio of helium atoms to vacancies in a cavity, N is the cavity number density, z is the compressibility factor determined for the equation of state discussed in an earlier chapter, and y_o is the packing fraction of helium atoms.

Instead of the emission of one interstitial at a time, it is possible that an entire interstitial platelet may be emitted. As shown by Trinkaus and Wolfer

[4.3], the least energy is expended when the dislocation loop radius equals the radius of the bubble R. Trinkaus [4.5] and Greenwood *et al.* [4.6] have shown that the condition for loop punching is

$$p\Omega \geq \frac{(2\gamma + \mu b)\Omega}{R} \tag{4.4}$$

when the bubble radius R is less than about $15b$. Here, μ is the bulk modulus and b is the Burgers vector.

As can be seen, there is a radius dependence for loop punching, whereas self-interstitial emission is nearly independent of the bubble radius. While self-interstitial emission is favored over loop punching at small radii, the opposite is true at larger radii.

Athermal processes can be activated only if the above described conditions are satisfied. To determine if either of the two conditions is satisfied, it is assumed that a density of cavities (dependent on temperature) with a uniform radius exists and that all helium atoms are evenly distributed among the cavities. The pressure within the cavities can be found using the equation of state (discussed in a previous chapter) and compared with the two criteria. If one of the two criteria embodied in Equations 4.3 and 4.4 is satisfied, the cavity radius is increased incrementally until the pressure drops below the critical values for self-interstitial emission and for loop punching. It has been found that athermal cavity growth is significant only under extremely high helium production or implantation rates as is seen in blistering studies.

4.3. Bias Driven Growth And Thermal Vacancy Exchange

According to the rate theory of void growth the swelling rate is given by [4.7]

$$\frac{d}{dt}\left(\frac{\Delta V}{V}\right) = 4\pi NRZ_v^o\left\{D_v\left[\frac{\bar{Z}_i}{\bar{Z}_v} - \frac{Z_i^o}{Z_v^o}\right]\Gamma - D_v(C_v^o - \bar{C}_v)\right\} \tag{4.5}$$

where N and R are the cavity number density and radius, respectively. $4\pi NR$ is known as the void sink strength (S_o). D_v is the vacancy diffusion coefficient, $\bar{Z}_{i,v}$ and $Z_{i,v}^o$ are the average bias factors for interstitials and vacancies and the void bias factors for interstitials and vacancies, respectively. $\bar{C}_v$ is the sink-averaged vacancy concentration and C_v^o is the vacancy concentration in equilibrium with a cavity. Γ is defined as

$$\Gamma = \frac{S}{2\lambda D_v}[\sqrt{\alpha^2 + \beta} - \alpha] \tag{4.6}$$

where $\lambda = 4\pi R_c/\Omega$, R_c is the recombination radius. $\alpha = 1 + \lambda\bar{C}_v/(S\bar{Z}_i)$, $\beta = 4\lambda D_v P_{pd}/(S^2\bar{Z}_i\bar{Z}_v)$, P_{pd} is the production rate of point defects. S is the total sink strength, which is composed of the void sink strength (S_o) and the dislocation sink strength (S_d).

The second term in Equation 4.5 is due to the flow of vacancies to or away from the cavities, depending on the vacancy concentration in local thermodynamic equilibrium with the cavity. This concentration is given by

$$C_v^o = C_v^{eq}\exp\left(\frac{p_o\Omega}{kT}\right) \tag{4.7}$$

where $p_o = (2\gamma/R - p)$ and C_v^{eq} is the thermal equilibrium vacancy concentration. For over-pressurized bubbles ($p > 2\gamma/R$) there will be a net flow of vacancies to the bubble surface. Because of the temperature dependence of D_v, the second term in the swelling rate Equation 4.5 (annealing term) is not important at temperatures below about 500^oC. However, at temperatures above about 600^oC the annealing term is comparable to or larger than the first term (bias term).

The time evolution of the microstructure plays an important role in the bias term. In particular, the sink strengths (S_o and S_d) and the sink-averaged parameters ($\bar{C}_v$, $\bar{Z}_i$, and $\bar{Z}_v$) change with the microstructure. If only two sinks types are present, namely cavities of equal radii and edge dislocations, then

$$\text{bias driven swelling rate} \sim \frac{S_0\, S_d}{(S_d + S_o)^2} \left(\frac{Z_v^o\, Z_i^d - Z_i^o\, Z_v^d}{\bar{Z}_i\, \bar{Z}_v} \right)$$

where $Z_{i,v}^d$ are the dislocation bias factor for interstitials and vacancies. From this expression it can be seen that sink strengths and sink-averaged bias factors are important for bias driven growth. It is also evident that the maximum swelling rate for bias driven growth is attained when the void sink strength equals the dislocation sink strength as pointed out by Harkness and Li [4.8]. In this case the swelling rate is mainly determined by the bias factors and to a lesser extent by Γ. In turn, the net bias factor is critically dependent on the interstitial and vacancy relaxation volumes as shown by Sniegowski and Wolfer [4.9]. The results of typical bias factor calculations for dislocations and voids are illustrated in Figures 4.1 and 4.2.

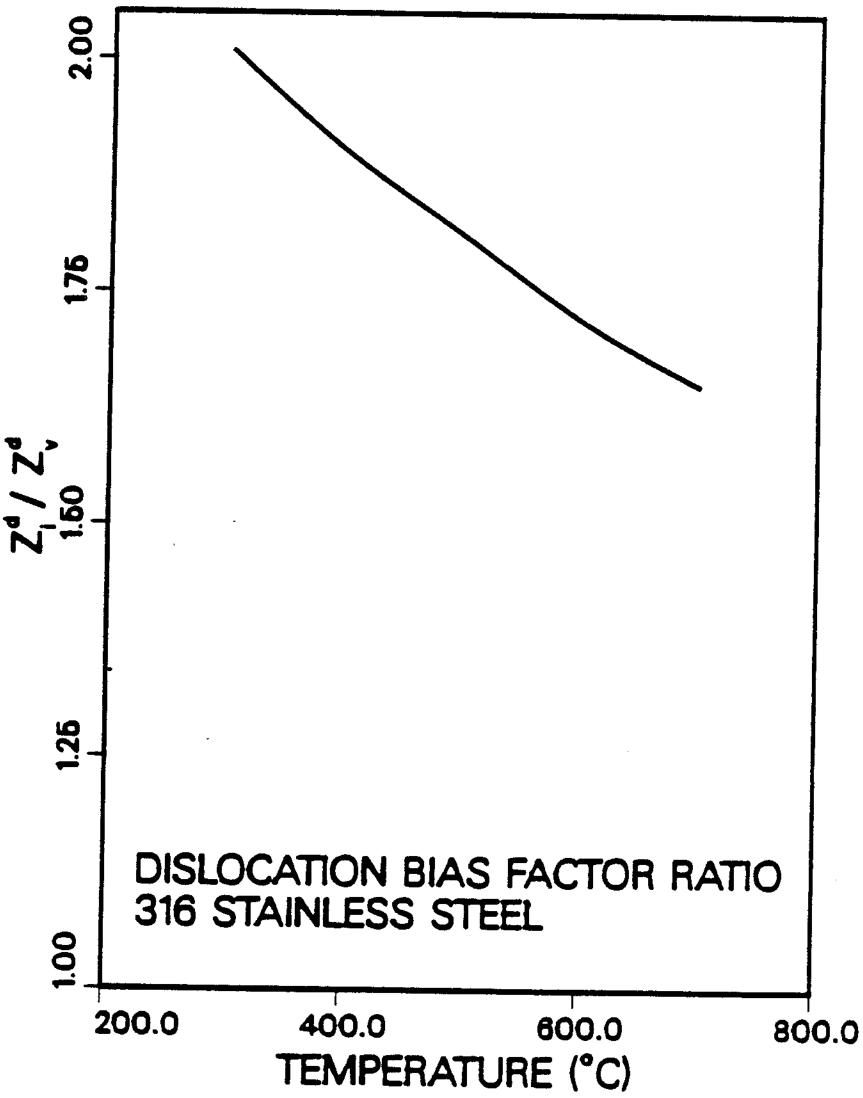

Figure 4.1. Dislocation bias factors for 316 stainless steel as a function of temperature [4.9]. This figure is also shown in a previous chapter and is shown here for completeness.

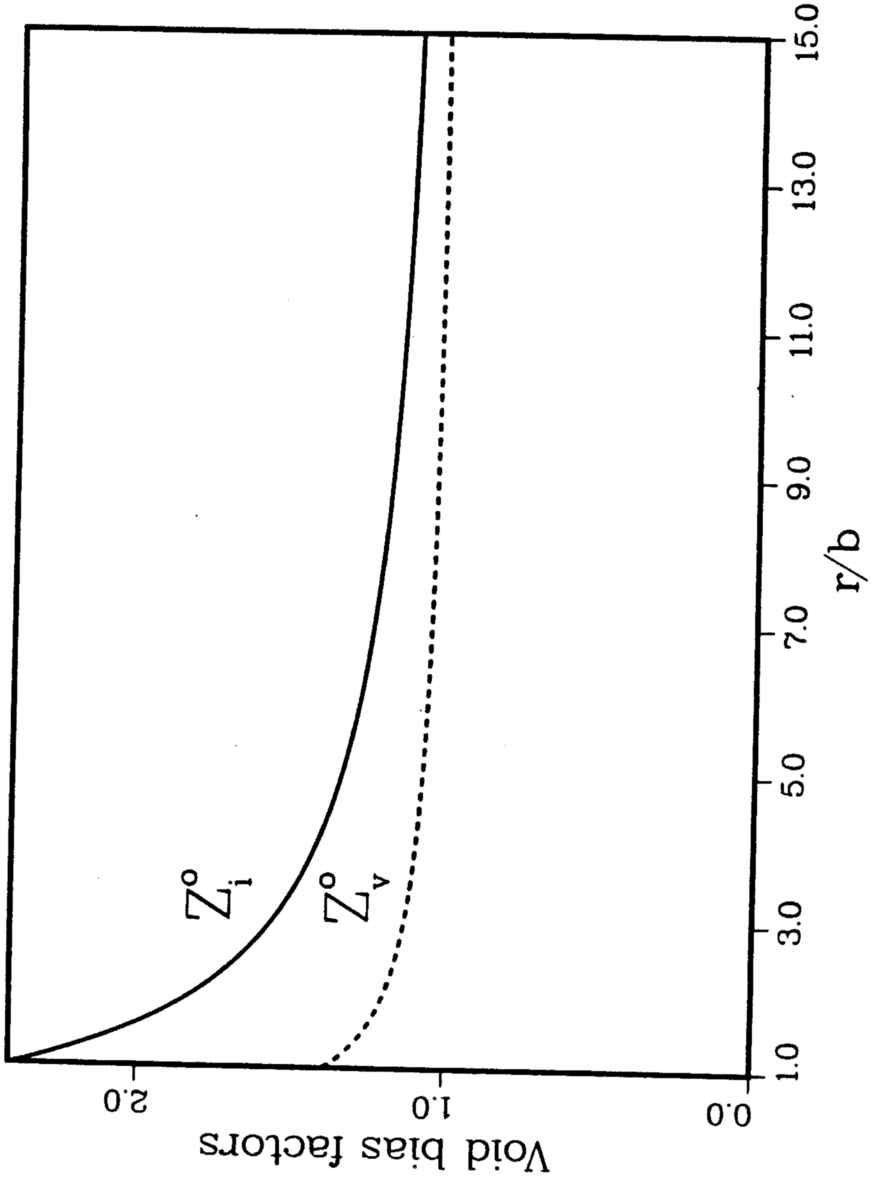

Figure 4.2. Void bias factors for 316 stainless steel as 500°C as a function of void size.

4.4. Discussion And Results

The swelling model described above and the dislocation evolution model described in an earlier chapter have been coded into a computer program known as WINGRA (WIsconsiN Growth RAte code). The flow diagram, Table 4.1, summarizes the method of determining swelling rate and swelling. It also illustrates how bias factors and sink strengths are continuously evaluated as the microstructure evolves. The results of the calculations are as follows.

1. Athermal processes (self-interstitial emission and loop punching) are not activated unless blistering type conditions are modeled for which the He/dpa ratio is about 1000.
2. Thermal vacancy exchange is not important until higher temperatures are reached. For austenitic stainless steels the temperature must exceed 600^oC. For the ferrite phase the temperature must exceed 500^oC. The minimum temperature where thermal vacancy exchange becomes noticeable is determined by the vacancy migration energy. The values for this energy along with other parameters of interest can be seen in Table 4.2.
3. Bias driven growth is the most important growth mechanism for temperatures below 500 and 600^oC for the ferrite phase and the austenitic stainless steels, respectively.

Two different steels (austenitic stainless steel and ferrite phase) were modeled for two different helium build-up rates (20 appm He/dpa and 0.6 appm He/dpa to model fusion and fission environments, respectively)

Table 4.1

1. Initialize the problem; set constraints: material parameters, dose rate, helium buildup rate, initial dislocation density.

2. For a given temperature determine the dislocation bias factors $Z^d_{i,v}$, set the temperature dependent parameters.

3. Given a swelling, helium density, and temperature determine compressibility factor z and pressure in the cavity.

4. Determine void bias factors $Z^o_{i,v}$ and sink strengths $S_{o,d}$. Find sink averaged bias factors and vacancy concentration, $\bar{Z}_{i,v}$ and $\bar{C}_v$.

5. Calculate swelling rate and dislocation density rate of change. Find a suitable time step and increment swelling and dislocation density. Go to step 3 as necessary.

Table 4.2

	316 SS	ferrite
lattice parameter (m)	3.639×10^{-10}	2.8664×10^{-10}
vacancy relaxation volume (Ω)	-0.2	-0.5
interstitial relaxation volume (Ω)	1.5	0.85
vacancy formation energy (J)	2.88×10^{-19}	2.464×10^{-19}
interstitial formation energy (J)	9.6×10^{-19}	9.6×10^{-19}
vacancy migration energy (J)	1.92×10^{-19}	2.016×10^{-19}
interstitial migration energy (J)	2.4×10^{-20}	3.2×10^{-20}
vacancy diffusion constant (m^2/sec)	1.29×10^{-6}	4.463×10^{-5}
dpa rate (dpa/sec)	1.0×10^{-6}	1.0×10^{-6}
cascade efficiency	0.1	0.1

with two different material starting conditions (cold-worked and annealed). The two Figures 4.3 and 4.4 show the results for swelling. An explanation of the results follows.

For 316 austenitic stainless steel a steady state swelling rate of between 0.7 %/dpa and 1.3 %/dpa is calculated for temperatures between 300^oC and 600^oC. The variation in steady state swelling rates is due mainly to variations in sink strengths. The lower the temperature the higher the void number density; hence, the greater the difference between void and steady state dislocation sink strength. At higher temperatures the sink strengths are closer to being equal and a higher swelling rate is calculated.

For ferrite phase a steady state swelling rate of between 0.01 %/dpa and 0.3 %/dpa is calculated. Once again the difference in swelling rate can be attributed to variation in steady state sink strengths for voids and dislocations.

For both steels at 20 appm He/dpa, differences in early swelling rates for annealed versus cold-worked material at 300^oC can be attributed to the time evolution of the dislocation density. The annealed material takes longer to reach a steady state dislocation density than does cold-worked material. Therefore, a more slowly increasing swelling rate for 300^oC can be seen for the annealed material than for the cold-worked material. However, as stated previously the small dislocation loops have not been accounted for.

For both steels at 0.6 appm He/dpa an incubation-type period is observed at early times. This latent period is due to there not being sufficient

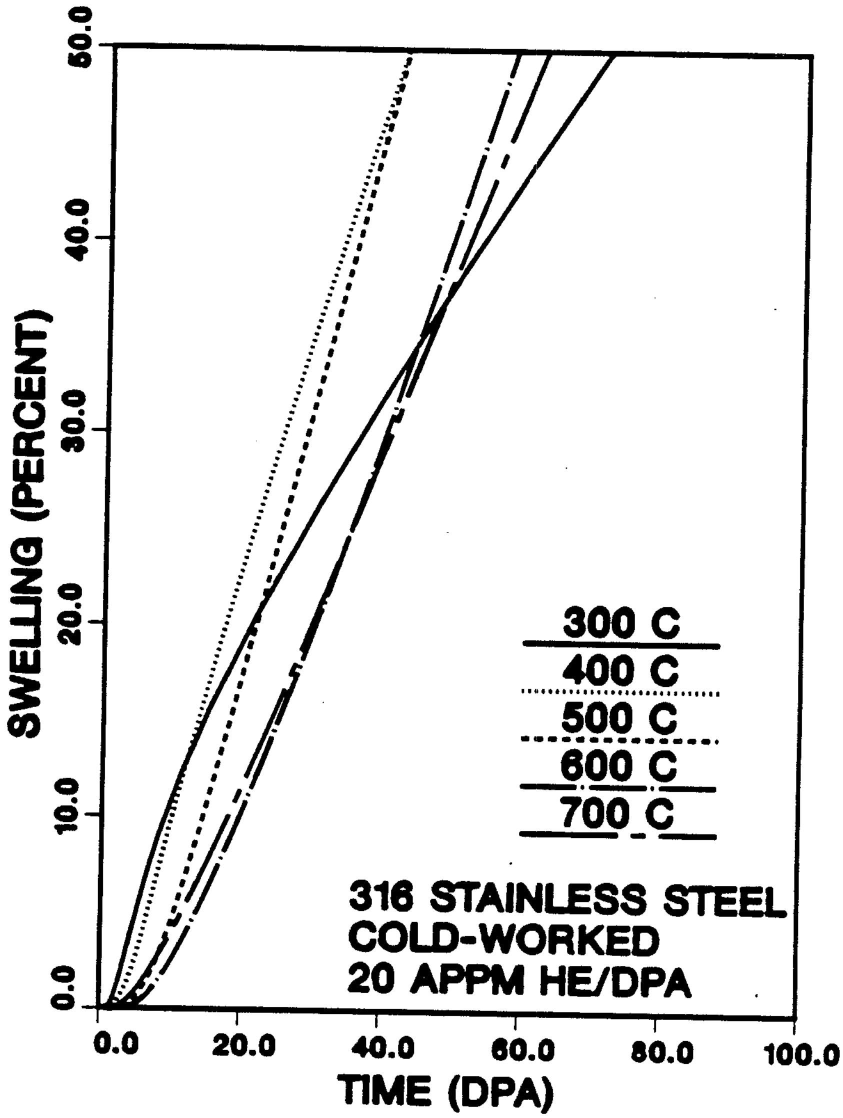

Figure 4.3a. Swelling versus dpa for various temperatures. Cold-worked 316 austenitic stainless steel, 20 appm He/dpa.

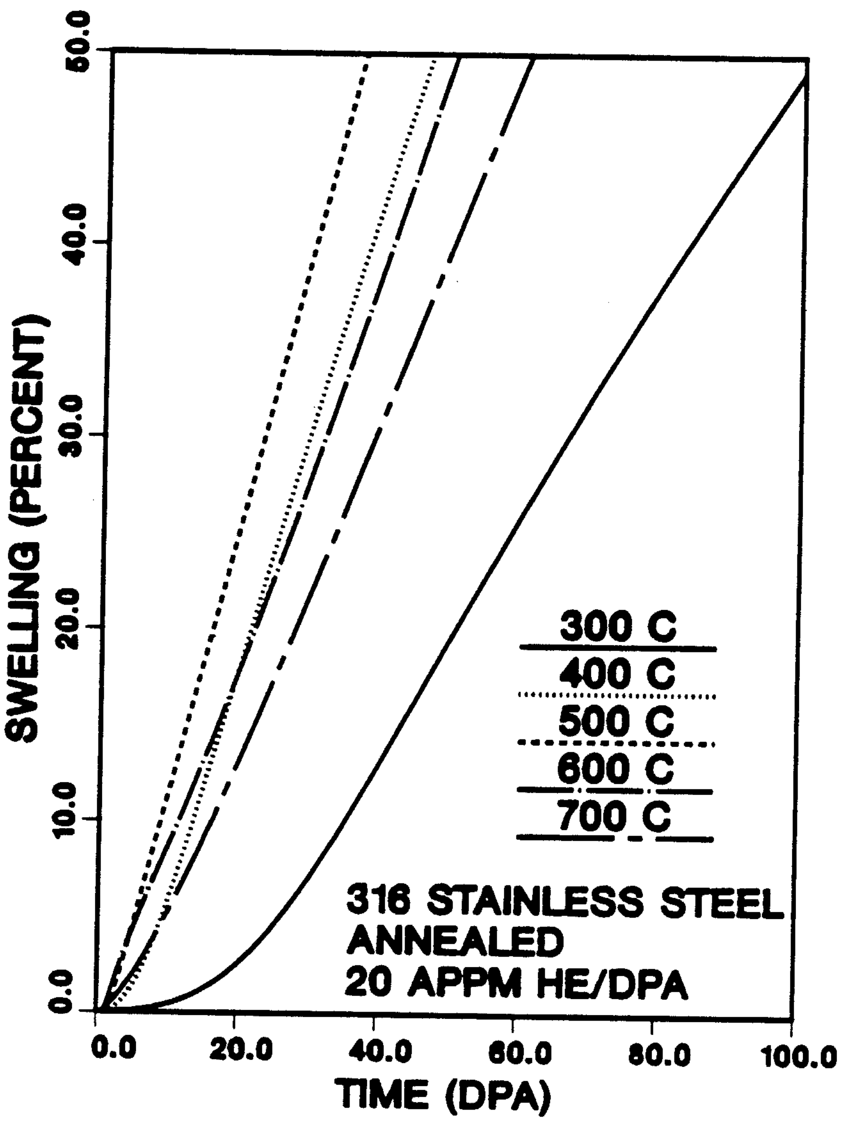

Figure 4.3b. Swelling versus dpa for various temperatures. Annealed 316 austenitic stainless steel, 20 appm He/dpa.

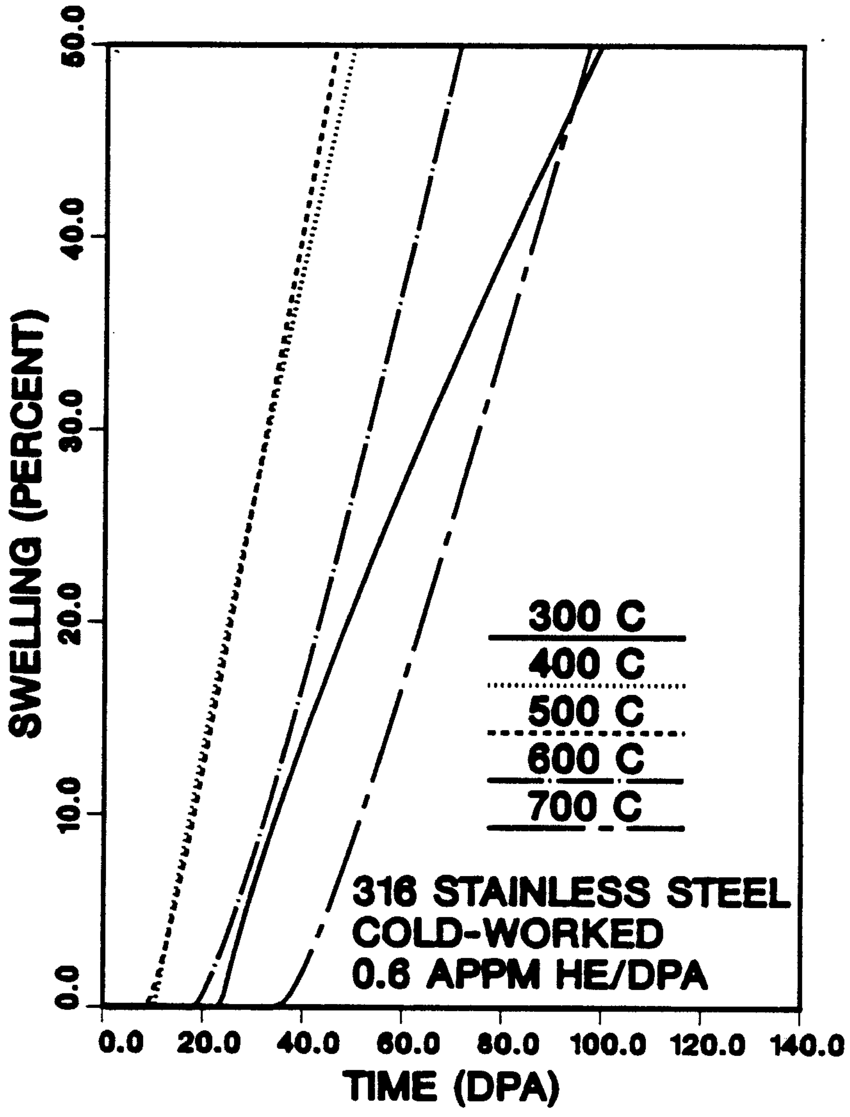

Figure 4.3c. Swelling versus dpa for various temperatures. Cold-worked 316 austenitic stainless steel, 0.6 appm He/dpa.

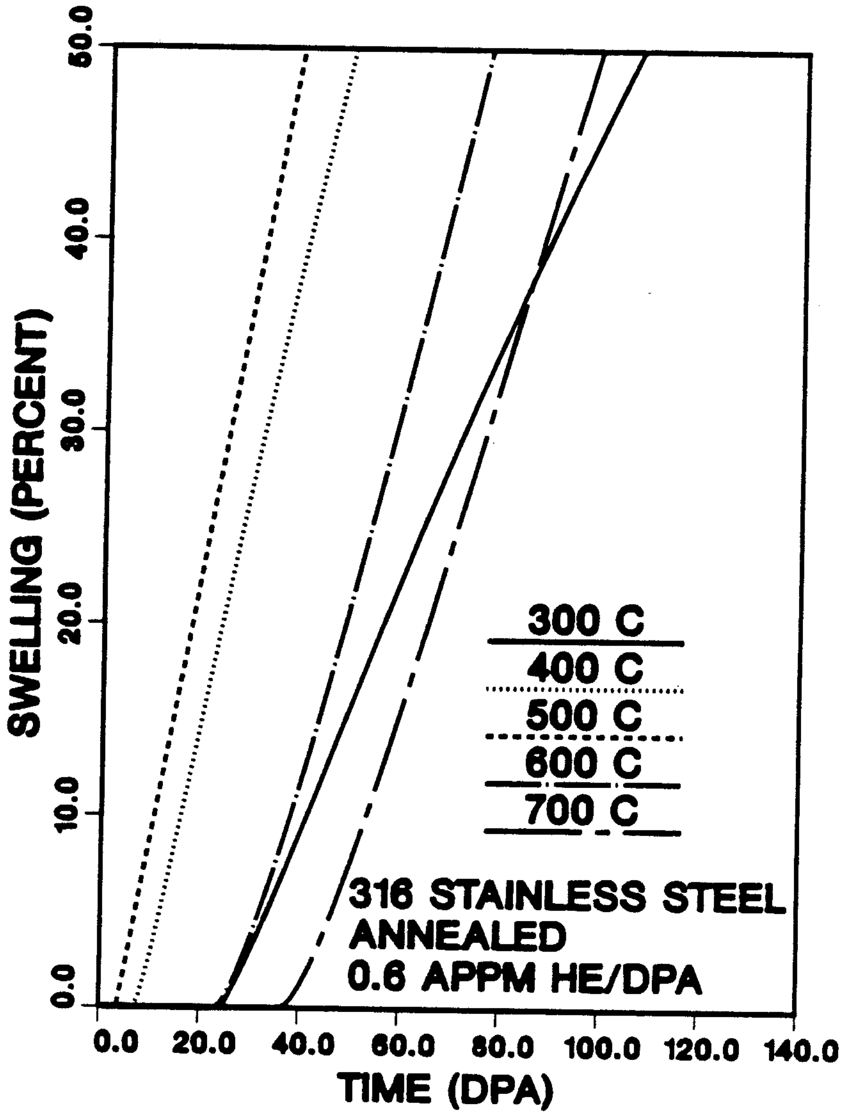

Figure 4.3d. Swelling versus dpa for various temperatures. Annealed 316 austenitic stainless steel, 0.6 appm He/dpa.

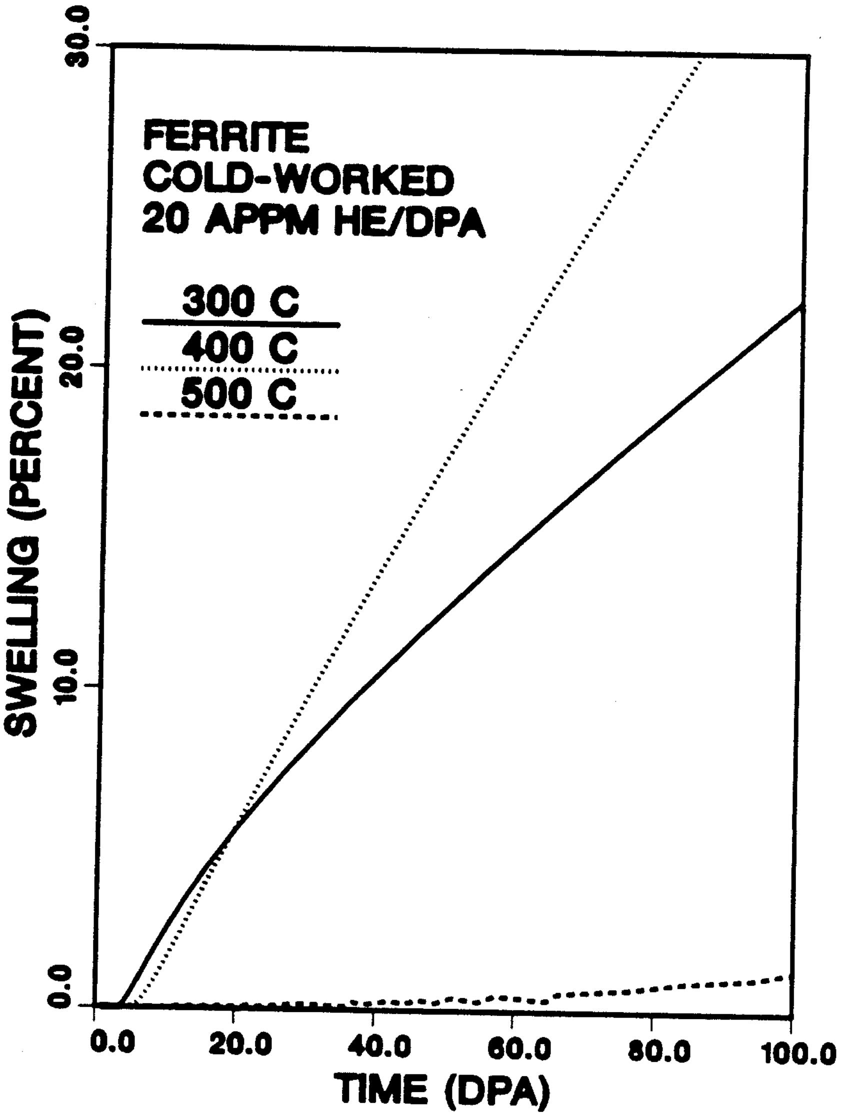

Figure 4.4a. Swelling versus dpa for various temperatures. Cold-worked ferrite phase, 20 appm He/dpa.

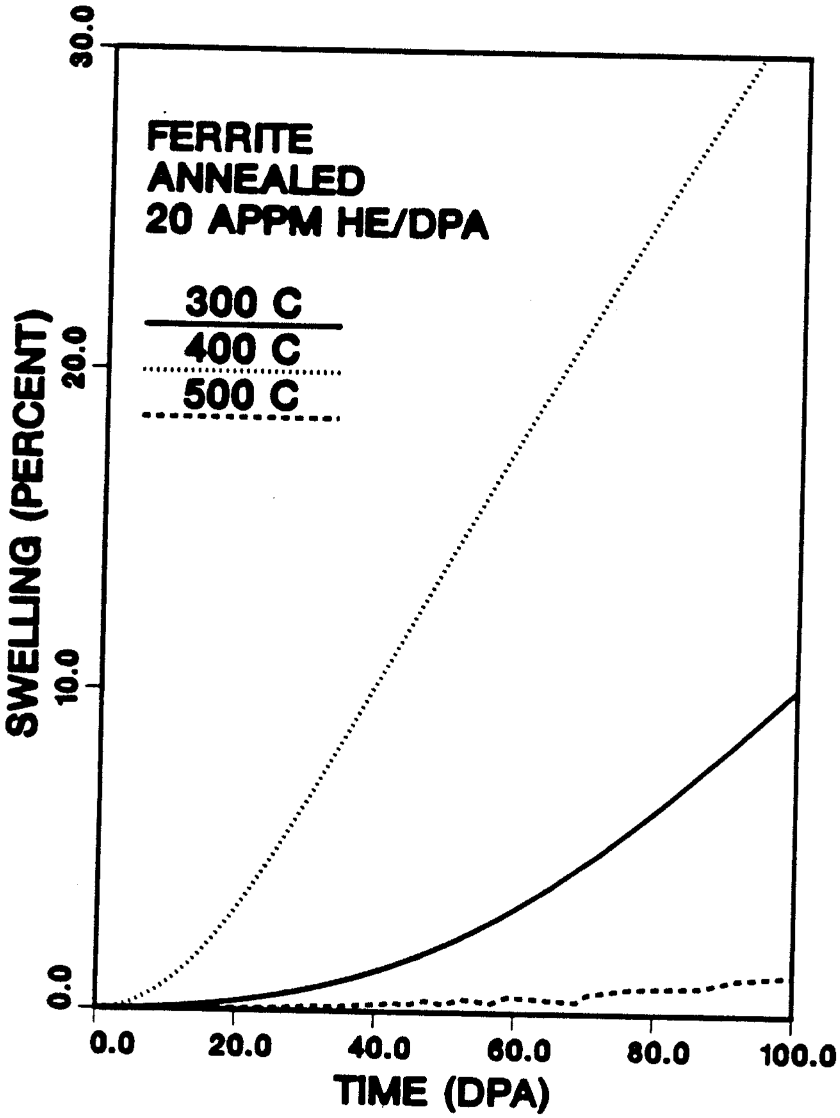

Figure 4.4b. Swelling versus dpa for various temperatures. Annealed ferrite phase, 20 appm He/dpa.

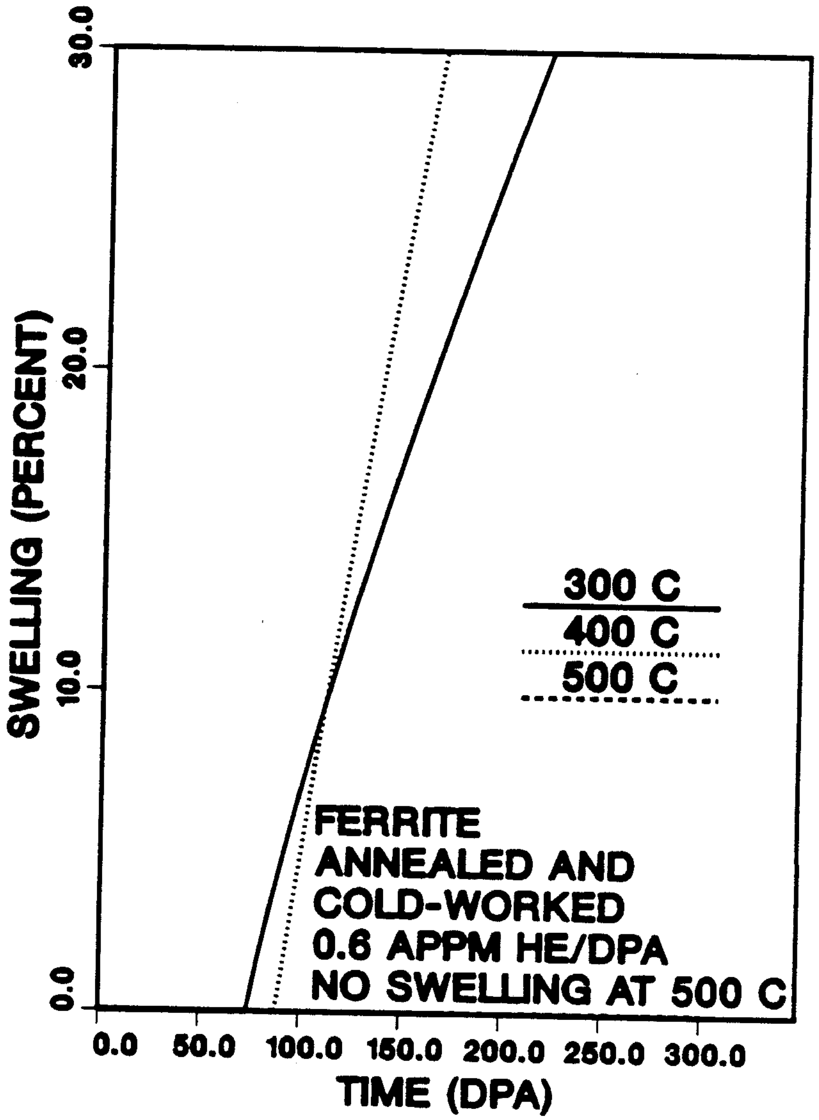

Figure 4.4c. Swelling versus dpa for various temperatures. Cold-worked and annealed ferrite phase, 0.6 appm He/dpa. Swelling rates for the 0.6 appm He/dpa case are the same for both cold-worked and annealed because the onset of swelling occurs after steady state dislocation density is reached.

helium pressure to force the cavities to grow to sufficient size for bias driven growth to dominate. However, once the cavity reaches a critical size for bias driven growth to become dominant, the voids grow according to rate theory calculations. This then explains the rapid changes in slope for swelling as a function of dose. The latent period of very slow void growth is due to the interplay of two factors. First, small vacancy clusters whether empty or filled with helium, possess a significant bias for preferential interstitial absorption due to the image interaction; this bias decreases however with increasing cavity radius, as is illustrated in Figure 4.2. The small cavities are stabilized by the helium and growth requires, for some period, the continuing capture of additional helium. As a result, the pressure in small cavities becomes very large which in turn enhances bias driven growth, and the pressure decreases rapidly as the radius increases. Figure 4.5 shows the net pressure $(p-2\gamma/R)$ as a function of dose for the two helium production rates of 0.6 and 20 appm He/dpa. It is seen that the small cavities are extremely over-pressurized but with increasing dose rapidly convert to voids as already pointed out by Stoller and Odette [4.10]. Bias driven growth becomes dominant after $(p-2\gamma/R)$ reaches its minimum. It is found that this conversion to a bias driven void occurs at a radius of about 1.2nm independent of the helium production rate.

The present void growth model for swelling needs several improvements before the swelling predictions can be compared with experiments. Most importantly, it is necessary to allow for time-dependent vacancy cluster formation in order to obtain a cavity size distribution. This will produce a more

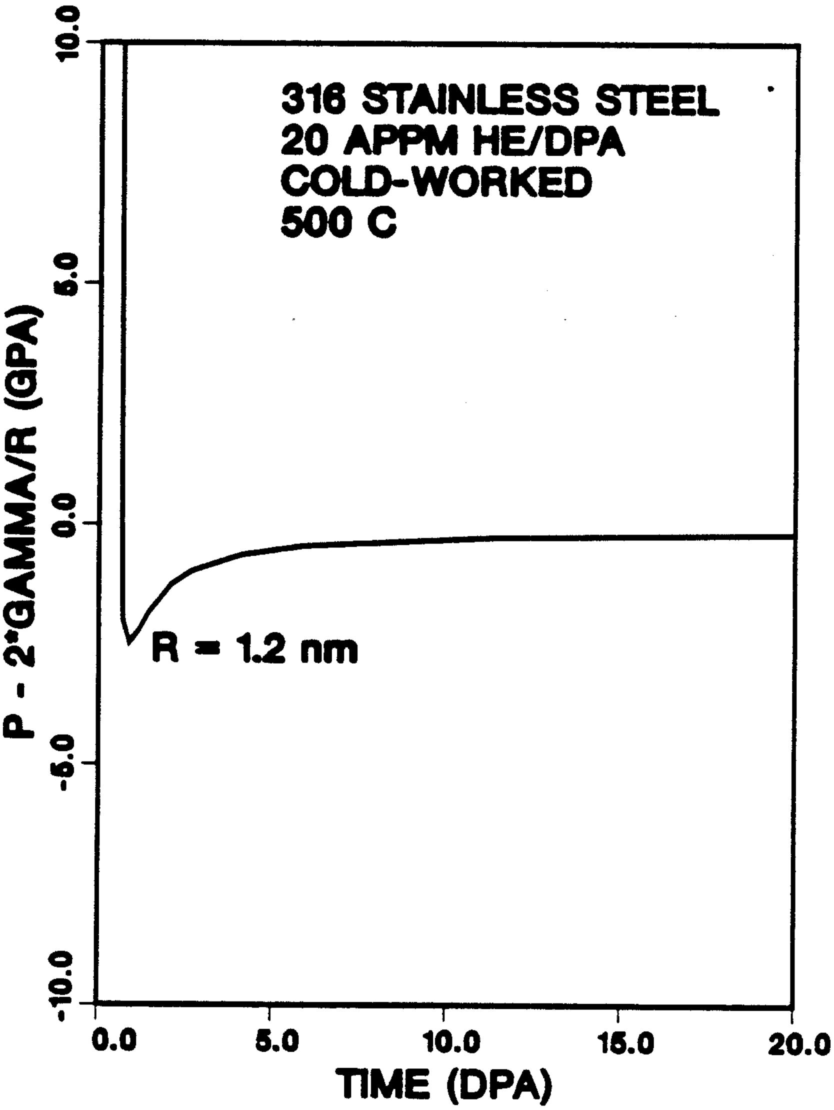

Figure 4.5a. Net pressure versus dpa for 20 appm He/dpa. The minimum occurs at approximately 1.2 nm.

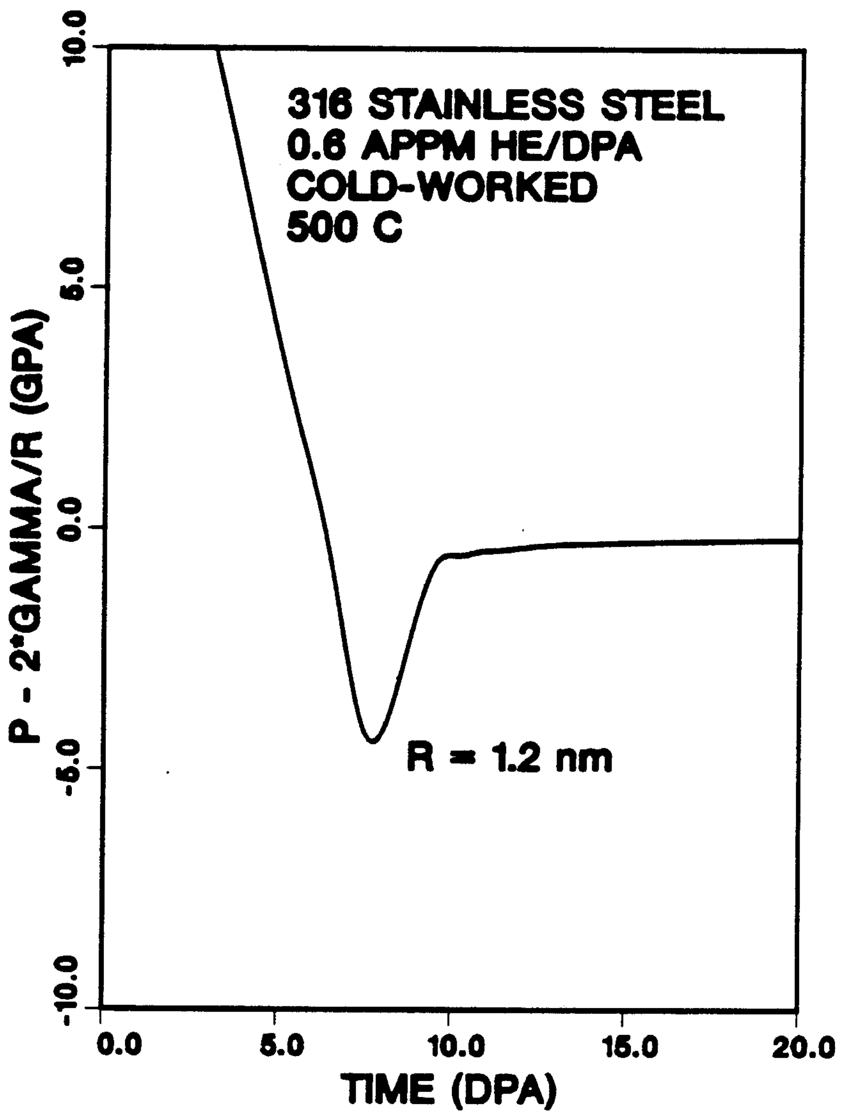

Figure 4.5b. Net pressure versus dpa for 0.6 appm He/dpa. As in the case of 20 appm He/dpa, the minimum occurs at approximately 1.2 nm.

gradual transition in swelling from the transient period to the steady state period. A second modification will also be required to allow for the continued formation of small helium bubbles in the presence of already existing large voids whenever the helium production rate is high. The formation of a bimodal cavity distribution has been observed in HFIR irradiated type 316 stainless steels [4.11,4.12]. Recent theoretical work by Wehner and Wolfer [4.13] has been able to model quite well void nucleation as a function of time. Future work on void swelling may be able to use their results to more accurately model number and size distribution of voids during nucleation.

References

[4.1.] Garner, F. A., Recent Insights on the Swelling and Creep of Irradiated Austenitic Alloys, *ASTM-STP-870*, to be published.

[4.2.] Gelles, D. J., *Journal of Nuclear Materials* **122 & 123** (1984) 202.

[4.3.] Trinkaus, H. and Wolfer, W. G., Conditions for Dislocation Loop Punching by Helium Bubbles, *Journal of Nuclear Materials* **122 & 123** (1984).

[4.4.] Glasgow, B. B. and Wolfer, W. G., Comparison of Mechanisms for Cavity Growth by Athermal and Thermal Processes, *Journal of Nuclear Materials* **122 & 123** (1984) 503–508.

[4.5.] Trinkaus, H., *Radiation Effects* **78** (1983) 189.

[4.6.] Greenwood, G. W., Forman, A. J. E., and Rimmer, D. E., *Journal of Nuclear Materials* **4** (1959) 305.

[4.7.] Brailsford, A. D. and Bullough, R., The Rate Theory of Swelling Due to Void Growth in Irradiated Materials, *Journal of Nuclear Materials* **44** (1972) 121–135.

[4.8.] Harkness, S. D. and Li, C. Y., "Proceedings of the International Conference on Radiation-Induced Voids in Metals", J. W. Corbett and L. C. Ianniello, Eds., (1971) 798.

[4.9.] Sniegowski, J. J. and Wolfer, W. G., On the Physical Basis for the Swelling Resistance of Ferritic Steels, "Proceedings of the Topical Conference on Ferritic Alloys for Use in Nuclear Energy Technologies", June 1983, to be published.

[4.10.] Stoller, R. E. and Odette, G. R., A Model Based Fission-Fusion Correlation of Cavity Swelling in Stainless Steel, *Journal of Nuclear Materials* **104** (1981) 1361.

[4.11.] Maziasz, P. J., *Journal of Nuclear Materials* **108** (1982) 359.

[4.12.] Maziasz, P. J., Comparison of Swelling and Cavity Microstructure Development for Type 316 Stainless Steel Irradiated in EBR-II and HFIR, *Journal of Nuclear Materials* **122 & 123** (1984) 236.

[4.13.] Wehner, M. F. and Wolfer, W. G., to be published in *Philosophical Magazine A*.

Chapter 5

INELASTIC STRESS ANALYSIS OF A THIN SHELL ELEMENT

5.1. Introduction

Current proposals for high heat flux fusion components include duplex thin walled structures. The advantage of such a structure is that the plasma side material can be chosen to minimize sputtering and the coolant side material can be chosen to maximize heat transfer. The structure may be subjected to high temperatures, high temperature gradients, thermal and irradiation creep, swelling, and thermal expansion. While extensive stress analysis has been carried out for high heat flux structures [5.1] made of single materials such as 316 stainless steel, stress analysis for duplex structures is only just beginning. One exception has been the work of Mattas [5.2]. Mattas has analysed structures with the plasma side material being beryllium or graphite and the coolant side material being 316 stainless steel or V-15Cr-5Ti.

This chapter presents the development of the inelastic stress equations for a thin shell element with arbitrary material properties, and subsequently specializes it for a plate constrained from bending. As part of the development, the temperature distribution, swelling, and creep models are discussed. Finally, the results of the model are presented for a beryllium/copper plate.

5.2. Inelastic Stress Equation

Consider a thin plate constrained from bending but free to expand with no external forces. The well known stress equation for this case is

$$\sigma_x(1-\nu^2) = \frac{E}{h}\int(e_x+\nu e_y)dz - E(e_x+\nu e_y) \tag{5.1}$$

where σ_x is the stress in the x-direction, E is Young's Modulus, h is the plate thickness, ν is Poisson's Ratio and e_x is the strain in the x-direction. One of the simplifying assumptions made in deriving Equation 5.1 is that the material properties are constant through the material. What follows is a general analysis of the stress equation when material properties are not assumed constant.

Consider a shell element as shown in Figure 5.1. A shell is defined as a thin curved surface whose thickness is much less than its other two dimensions. In the limit of no curvature a shell becomes a thin plate. For a given shell element assume that the membrane forces (N_i and N_j) and the bending moments (M_i and M_j) are specified. The problem then becomes how to determine the principal stresses (σ_i and σ_j) through the shell thickness given the membrane forces and bending moments.

Hooke's Law for elastic material and a biaxial state of stress is given by

$$\sigma_i = \frac{E}{(1-\nu^2)}(e_i^e+\nu e_j^e) \tag{5.2}$$

where e^e is the elastic strain. The subscripts i and j can be interchanged to obtain the principal stresses in the two directions. Assuming a state of

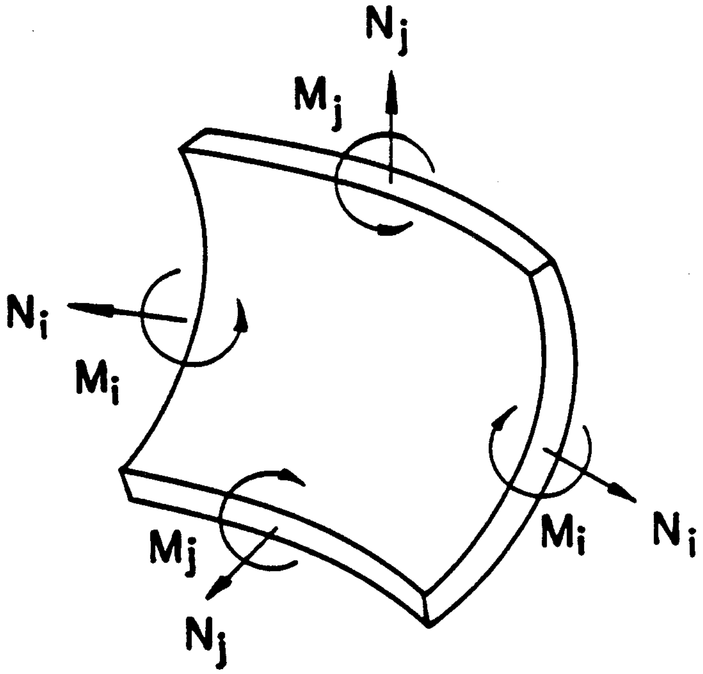

Figure 5.1. A shell element with the membrane forces (N and N_j) and bending moments (M and M_j).

plane stress and no shearing strains, σ_i and σ_j are the only stresses present. Introduce next the inelastic strains by assuming that the total strain is a superposition of elastic and inelastic strains; that is,

$$e_i^t = e_i^e + e_i^i \tag{5.3}$$

Substituting Equation 5.3 into Equation 5.2, one obtains

$$\sigma_i = \frac{E}{(1-\nu^2)}(e_i^t - e_i^i) + \frac{E\nu}{(1-\nu^2)}(e_j^t - e_j^i) \tag{5.4}$$

The next step is to choose an appropriate strain field which is compatible with the assumed deformations. Consider the shell element with only N_i and N_j acting on it. The total strain field is not constant through the thickness as in the plate element. Rather, the strain field varies linearly as

$$e_i^t = K_i(1 - \frac{z}{r_j}) \tag{5.5}$$

Similarly in pure bending the strain field varies quadratically [5.3] as

$$e_i^t = L_i(1 - \frac{z}{r_j})z \tag{5.6}$$

where K_i and L_i are constants, r_j is the radius of curvature in the j-direction and z is the distance from the shell midplane. Then substituting Equations 5.5 and 5.6 into Equation 5.4 results in

$$\begin{aligned}\sigma_i = {} & \frac{E}{(1-\nu^2)}\left[K_i(1 - \frac{z}{r_j}) + L_i(1 - \frac{z}{r_j})z - e_i^i\right] \\ & + \frac{E\nu}{(1-\nu^2)}\left[K_j(1 - \frac{z}{r_i}) + L_j(1 - \frac{z}{r_i})z - e_j^i\right]\end{aligned} \tag{5.7}$$

There are now two such equations (one for σ_i, Equation 5.7, and a corresponding equation for σ_j) but with a total of four unknowns. Boundary conditions must now be imposed to assure self-consistency between applied loads and the stress distribution. These conditions are

$$N_i = \int \sigma_i(1 - \frac{z}{r_j})dz \tag{5.8}$$

$$M_i = \int \sigma_i(1 - \frac{z}{r_j})z\,dz \tag{5.9}$$

Substituting Equation 5.7 into Equations 5.8 and 5.9 two of the four simultaneous equations in the constants K and L are

$$\begin{aligned} N_i = &\int \frac{E}{(1-\nu^2)}\left[K_i(1 - \frac{z}{r_j}) + L_i(1 - \frac{z}{r_j})z - e_i^i\right] dz \\ &+ \int \frac{E\nu}{(1-\nu^2)}\left[K_j(1 - \frac{z}{r_i}) + L_j(1 - \frac{z}{r_i})z - e_j^i\right] dz \end{aligned} \tag{5.10}$$

$$\begin{aligned} M_i = &\int \frac{E}{(1-\nu^2)}\left[K_i(1 - \frac{z}{r_j}) + L_i(1 - \frac{z}{r_j})z - e_i^i\right] z\,dz \\ &+ \int \frac{E\nu}{(1-\nu^2)}\left[K_j(1 - \frac{z}{r_i}) + L_j(1 - \frac{z}{r_i})z - e_j^i\right] z\,dz \end{aligned} \tag{5.11}$$

In order to simplify the solving of the four equations (Equation 5.10 and 5.11 and their corresponding j-direction equations), introduce the following four quantities where $n = 0, 1, 2,$or 3:

$$\int \frac{E}{(1-\nu^2)} z^n dz = \Upsilon_n \tag{5.12}$$

$$\int \frac{E\nu}{(1-\nu^2)} z^n dz = \Gamma_n \tag{5.13}$$

$$\int \frac{E}{(1-\nu^2)} e_i^i z^n dz = \phi_n \tag{5.14}$$

$$\int \frac{E\nu}{(1-\nu^2)} e_i^i z^n dz = \varsigma_n \tag{5.15}$$

Now rewriting all four simultaneous equations with Equations 5.12–5.15 substituted and the individual terms separated, one obtains

$$\left[\Upsilon_0 - \frac{\Upsilon_1}{r_j}\right] K_i + \left[\Gamma_0 - \frac{\Gamma_1}{r_i}\right] K_j + \left[\Upsilon_1 - \frac{\Upsilon_2}{r_j}\right] L_i + \left[\Gamma_1 - \frac{\Gamma_2}{r_i}\right] L_j = N_i + \phi_0^i + \varsigma_0^j \tag{5.16}$$

$$\left[\Gamma_0 - \frac{\Gamma_1}{r_j}\right] K_i + \left[\Upsilon_0 - \frac{\Upsilon_1}{r_i}\right] K_j + \left[\Gamma_1 - \frac{\Gamma_2}{r_j}\right] L_i + \left[\Upsilon_1 - \frac{\Upsilon_2}{r_i}\right] L_j = N_j + \phi_0^j + \varsigma_0^i \tag{5.17}$$

$$\left[\Upsilon_1 - \frac{\Upsilon_2}{r_j}\right] K_i + \left[\Gamma_1 - \frac{\Gamma_2}{r_i}\right] K_j + \left[\Upsilon_2 - \frac{\Upsilon_3}{r_j}\right] L_i + \left[\Gamma_2 - \frac{\Gamma_3}{r_i}\right] L_j = M_i + \phi_1^i + \varsigma_1^j \tag{5.18}$$

$$\left[\Gamma_1 - \frac{\Gamma_2}{r_j}\right] K_i + \left[\Upsilon_1 - \frac{\Upsilon_2}{r_i}\right] K_j + \left[\Gamma_2 - \frac{\Gamma_3}{r_j}\right] L_i + \left[\Upsilon_2 - \frac{\Upsilon_3}{r_i}\right] L_j = M_j + \phi_1^j + \varsigma_1^i \tag{5.19}$$

Let the equations be written as

$$A_j K_i + B_i K_j + C_j L_i + D_i L_j = G_i \tag{5.20}$$

$$B_j K_i + A_i K_j + D_j L_i + C_i L_j = G_j \tag{5.21}$$

$$C_j K_i + D_i K_j + E_j L_i + F_i L_j = H_i \tag{5.22}$$

$$D_j K_i + C_i K_j + F_j L_i + E_i L_j = H_j \tag{5.23}$$

where the coefficients A–H are defined by correspondence to Equations 5.16–5.19. To solve the system of four simultaneous equations by Cramer's Rule, first define a set of determinants to be

$$X_i = \det \begin{vmatrix} G_i & B_i & C_j & D_i \\ G_j & A_i & D_j & C_i \\ H_i & D_i & E_j & F_i \\ H_j & C_i & F_j & E_i \end{vmatrix} \qquad X_j = \det \begin{vmatrix} A_j & G_i & C_j & D_i \\ B_j & G_j & D_j & C_i \\ C_j & H_i & E_j & F_i \\ D_j & H_j & F_j & E_i \end{vmatrix}$$

$$Y_i = \det\begin{vmatrix} A_j & B_i & G_i & D_i \\ B_j & A_i & G_j & C_i \\ C_j & D_i & H_i & F_i \\ D_j & C_i & H_j & E_i \end{vmatrix} \qquad Y_j = \det\begin{vmatrix} A_j & B_i & C_j & G_i \\ B_j & A_i & D_j & G_j \\ C_j & D_i & E_j & H_i \\ D_j & C_i & F_j & H_j \end{vmatrix}$$

$$W = \det\begin{vmatrix} A_j & B_i & C_j & D_i \\ B_j & A_i & D_j & C_i \\ C_j & D_i & E_j & F_i \\ D_j & C_i & F_j & E_i \end{vmatrix}$$

And according to Cramer's Rule

$$K_i = X_i/W \qquad L_i = Y_i/W$$

$$K_j = X_j/W \qquad L_j = Y_j/W$$

The resulting equation for the principal stress becomes

$$\begin{aligned}\sigma_i = {} & \frac{E}{(1-\nu^2)}\left[\frac{X_i}{W}(1-\frac{z}{r_j}) + \frac{Y_i}{W}(1-\frac{z}{r_j})z - e_i^i\right] \\ & + \frac{E\nu}{(1-\nu^2)}\left[\frac{X_j}{W}(1-\frac{z}{r_i}) + \frac{Y_j}{W}(1-\frac{z}{r_i})z - e_j^i\right] \qquad (5.24)\end{aligned}$$

Equation 5.24 can be simplified for a plate constrained from bending with no membrane forces. In this case, the stress equation reduces to

$$\sigma_i(1-\nu^2) = \frac{E}{W}\left[X_i + \nu X_j\right] - E\left[e_i^i + \nu e_j^i\right] \qquad (5.25)$$

Furthermore, the determinants W and X are simplified and become

$$X_i = \det\begin{vmatrix} G_i & \Gamma_0 \\ G_j & \Upsilon_0 \end{vmatrix} \qquad X_j = \det\begin{vmatrix} \Upsilon_0 & G_i \\ \Gamma_0 & G_j \end{vmatrix}$$

$$W = \det\begin{vmatrix} \Upsilon_0 & \Gamma_0 \\ \Gamma_0 & \Upsilon_0 \end{vmatrix}$$

It can be shown that in the limit of homogeneous material properties for E and ν Equation 5.25 reduces to Equation 5.1.

5.3. Inelastic Strains

Inelastic strains are considered to arise from three sources: 1) thermal strains, 2) radiation induced swelling strains, and 3) thermal and radiation creep strains. Inserting the total strain

$$e_i^i = \alpha \Delta T + \frac{1}{3} S + e_i^c$$

into Equations 5.14 and 5.15, they become

$$\phi_0^i = \int \frac{E}{(1-\nu^2)} (\alpha \Delta T + \frac{1}{3} S + e_i^c) dz$$

$$\varsigma_0^j = \int \frac{E\nu}{(1-\nu^2)} (\alpha \Delta T + \frac{1}{3} S + e_i^c) dz$$

The quantity G_i defined previously as $G_i = N_i + \phi_0^i + \varsigma_0^j$ becomes ($N_i = 0$, no membrane forces)

$$G_i = \int \frac{E}{(1-\nu^2)} (1+\nu)(\alpha \Delta T + \frac{1}{3} S) dz + \int \frac{E}{(1-\nu^2)} (e_i^c + \nu e_j^c) dz$$

As a consequence of $\sigma_i = \sigma_j$, $e_i^c = e_j^c$. While the assumption of a one to one stress ratio is not necessary to the final development of the plate stress equations, it does greatly minimize the number of terms in the final result without detracting from the physical problem. G_i now becomes

$$G_i = G_j = G = \int \frac{E}{(1-\nu)} (\alpha \Delta T + \frac{1}{3} S + e^c) dz \tag{5.26}$$

and at the same time $X_i = X_j = X$. The stress Equation 5.25 is now

$$\sigma_i(1-\nu^2) = \frac{E}{W}(1+\nu)X - E(1+\nu)(\alpha\Delta T + \frac{1}{3}S + e^c)$$

or

$$\sigma_i = \frac{E}{(1-\nu)}\frac{X}{W} - \frac{E}{(1-\nu)}(\alpha\Delta T + \frac{1}{3}S + e^c) \tag{5.27}$$

where

$$\frac{X}{W} = \frac{\int \frac{E}{(1-\nu)}(\alpha\Delta T + \frac{1}{3}S + e^c)dz}{\int \frac{E}{(1-\nu)}dz} \tag{5.28}$$

Equations 5.26 and 5.28 represent the simplest case to study the stress evolution in a high heat flux component with spatially varying materials properties. Its simplicity makes it suitable for extensive scoping studies of composite structures for high heat flux applications. In the following, the time dependent profile in a duplex plate constrained from bending is investigated. This plate is assumed to consist of beryllium bonded to copper.

5.4. Materials Properties

Insufficient experimental evidence exists for copper to derive an empirical relationship between swelling and the irradiation parameters. In a previous chapter and in reference [5.4], a rate theory model for void swelling growth has been developed. This model predicts long term swelling rates for 316 stainless steel which agree quite well with the experimental evidence. Using the same model but with material properties of copper, theoretical swelling rates of copper as a function of temperature and neutron damage rate are calculated. The model predicts a maximum swelling rate of approximately

2%/dpa for copper in a rather narrow temperature range of 200°C to 450°C. Outside of this range little or no swelling occurs. To predict the swelling strains of the plasma side material beryllium, a recent model developed by Wolfer *et al.* [5.5] is used. Basically, the model assumes that swelling in beryllium takes place by two processes: 1) solid helium swelling where the helium precipitate grows by athermal emission of host metal atoms or loop punching, and 2) gaseous helium bubble swelling where growth occurs by the thermal absorption of vacancies. The latter process dominates at high temperatures and high helium concentrations. The helium production rate is assumed to be 14000 appm he/year; this quantity is derived from an assumed neutron wall loading of 4 MW/m^2.

For the inelastic strains associated with thermal creep, power law creep was assumed. The form of the power law creep equation is

$$\dot{e}^{th} = A\sigma^n e^{-B/T} \tag{5.29}$$

where for beryllium [5.6] $n = 3$, $A = 3.3 \times 10^{-12}$ per second, $B = 3.8 \times 10^4$ per °K. For copper $n = 4.8$, $A = 3.37 \times 10^{-31}$, and $B = 1.41 \times 10^4$. The constants for copper were found by fitting Equation 5.29 to the data by Frost *et al.* [5.7]. Irradiation creep strains are less well known than thermal creep strains. Nonetheless, some estimates can be made. Ghoniem states [5.6] that at a temperature of half the melting point there is a stress at which irradiation creep equals thermal creep. Ghoniem assumed that for beryllium this stress is 1.4×10^7 N/m^2 ($\sim$ 2 ksi). The creep compliance so calculated is $\psi = 4.79 \times 10^{-19}$ m^2/N/sec. The irradiation creep rate for beryllium is then

$$\dot{e}^{irr} = \frac{1}{2}\psi\sigma \tag{5.30}$$

The irradiation creep rate for copper can be estimated by considering the stress induced preferential absorption (SIPA) of interstitials at dislocations [5.8] due to irradiation. Using rate theory, a steady state creep compliance of $\psi = 5.35 \times 10^{-18}$ m^2/N/sec is estimated.

5.5. Discussion

The duplex structure examined consists of a layer of beryllium bonded to a layer of copper as shown in Figure 5.2. In the one dimensional temperature analysis it is assumed that the bonding between the layers is ideal. For calculation of the temperature distribution it is assumed that the thermal conductivity k has the form $k = \frac{1}{A+BT}$. Then using the conductivity integral approach [5.9] the temperature distribution can be calculated. The calculated temperature distribution is shown in Figure 5.3. The backside temperature is 90°C and the surface heat flux and the neutron wall loading is 4 MW/m^2. By separating Equation 5.28 into two integrals, one through the beryllium and one through the copper, the average strain through the duplex structure can be found. Then with Equation 5.27, the initial stress distribution through the structure as shown in Figure 5.4 is found. One can note the stress discontinuity at the interface between the two materials; this is due to the differences in properties between the materials.

To follow the time evolution of the stress distribution, the creep and swelling inelastic strains of each material are followed by numerically integrating their respective strain rates with each time increment. For the copper material it is found that the stresses relax very quickly to a near steady state value of about 40 MPa. The steady state value of the stresses can be found analytically by taking the time derivative of Equation 5.27 and setting it equal to zero. For the temperature calculated for the sample case, there is no swelling in the copper. It should be noted that the "steady state" stresses in copper are a function of the stresses in the beryllium.

The stress evolution in the beryllium is slightly more complicated. The evolution of the stress in beryllium is very dependent on the amount of helium assumed. Early in life before a significant amount of helium induced swelling occurs, the beryllium stresses relax. From beginning-of-life until about 1 year, the stress on the plasma surface relaxes from a value of ~240 MPa to ~90 MPa. After about 1 year, the compressive stress increases because of the onset of swelling. At about 20 years the stress distribution shown in Figure 5.5 is obtained.

5.6. Conclusion

The stress equation for thin walled shell elements as shown in Figure 5.1 has been developed and is given in Equation 5.25. A specialization of Equation 5.25 has also been developed for a thin plate constrained from bending with

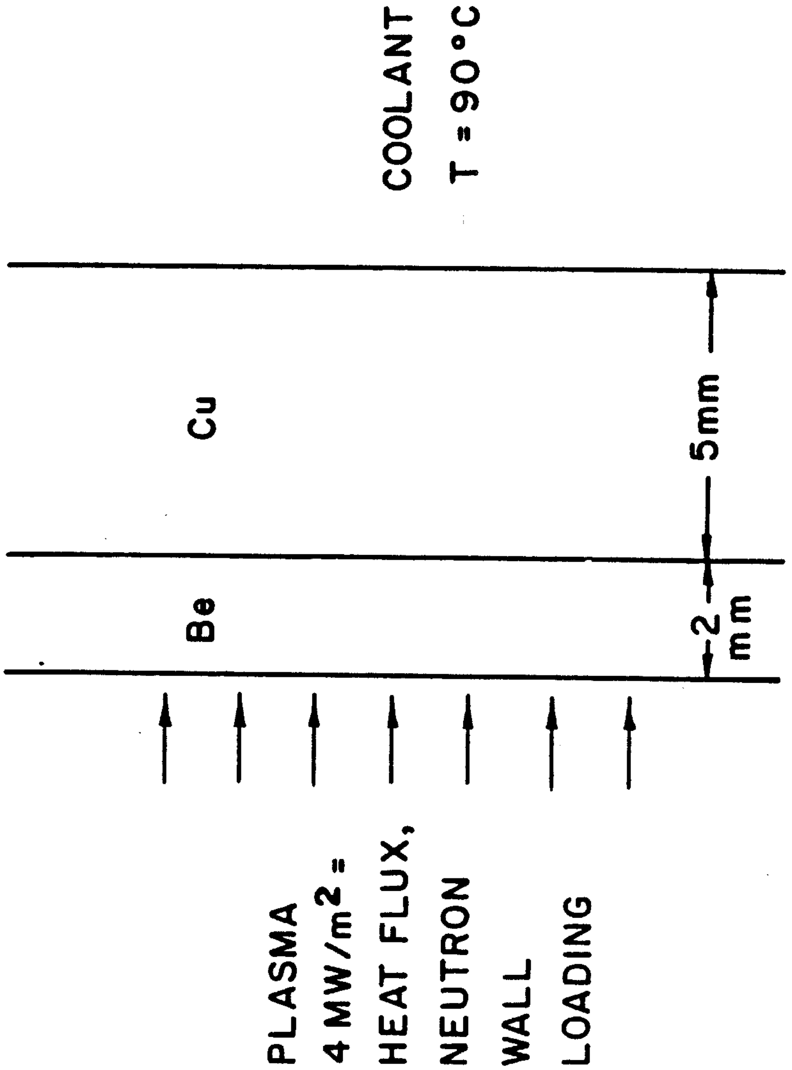

Figure 5.2. Illustration of duplex wall structure.

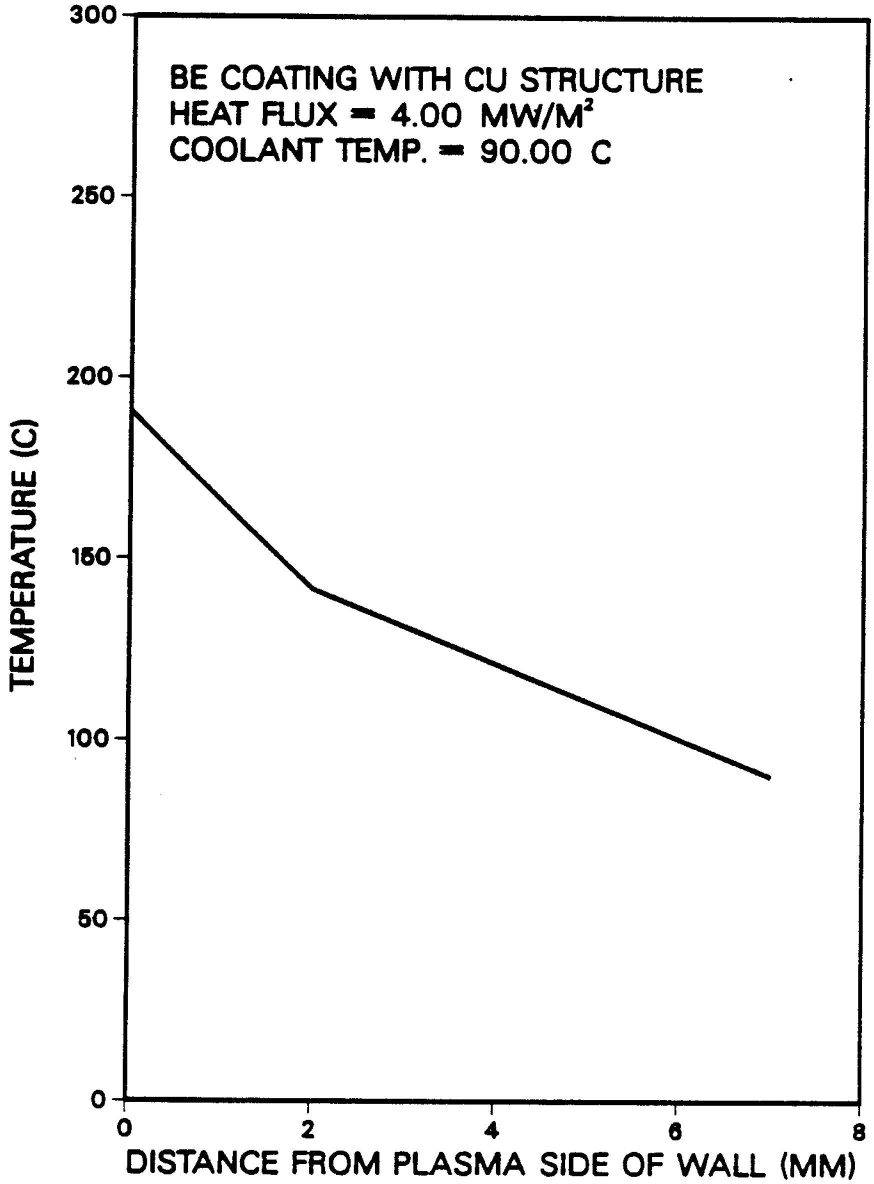

Figure 5.3. Temperature distribution through the duplex structure.

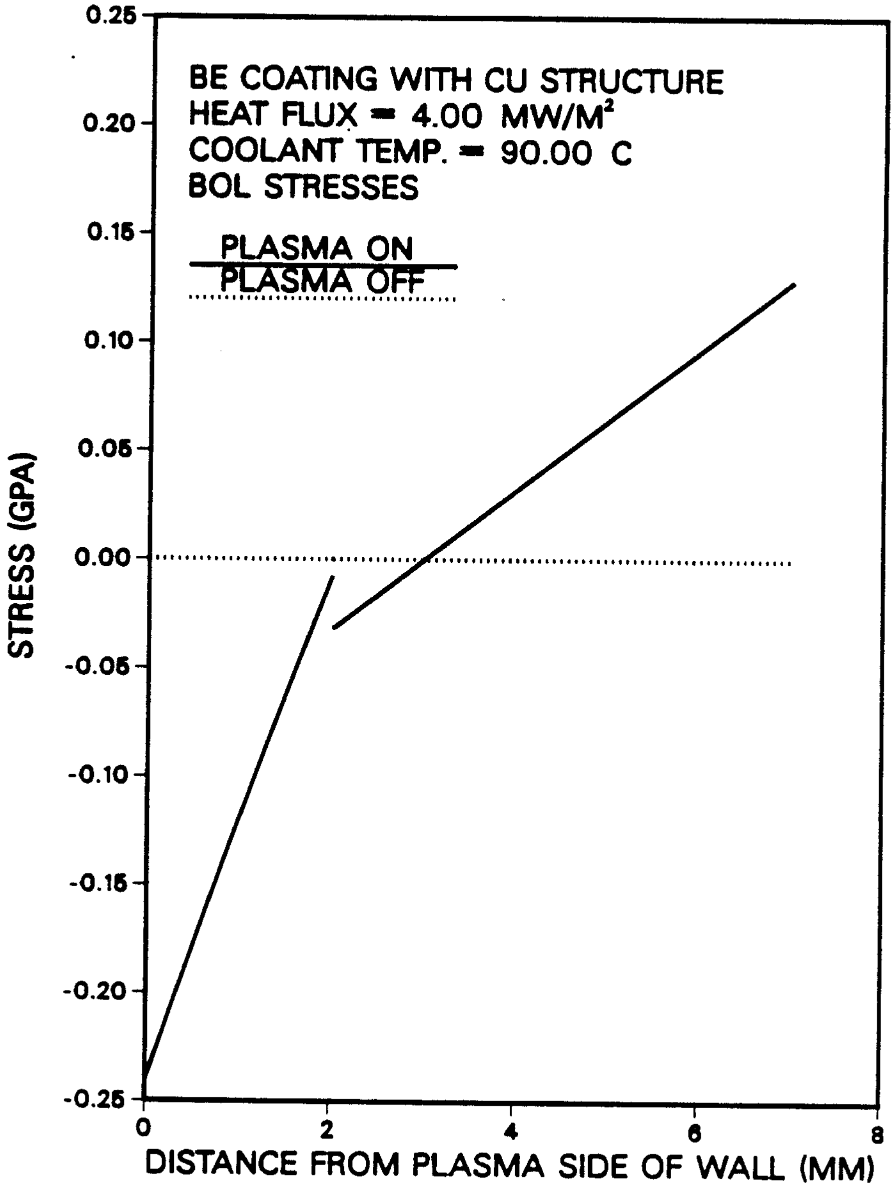

Figure 5.4. Initial stress distribution.

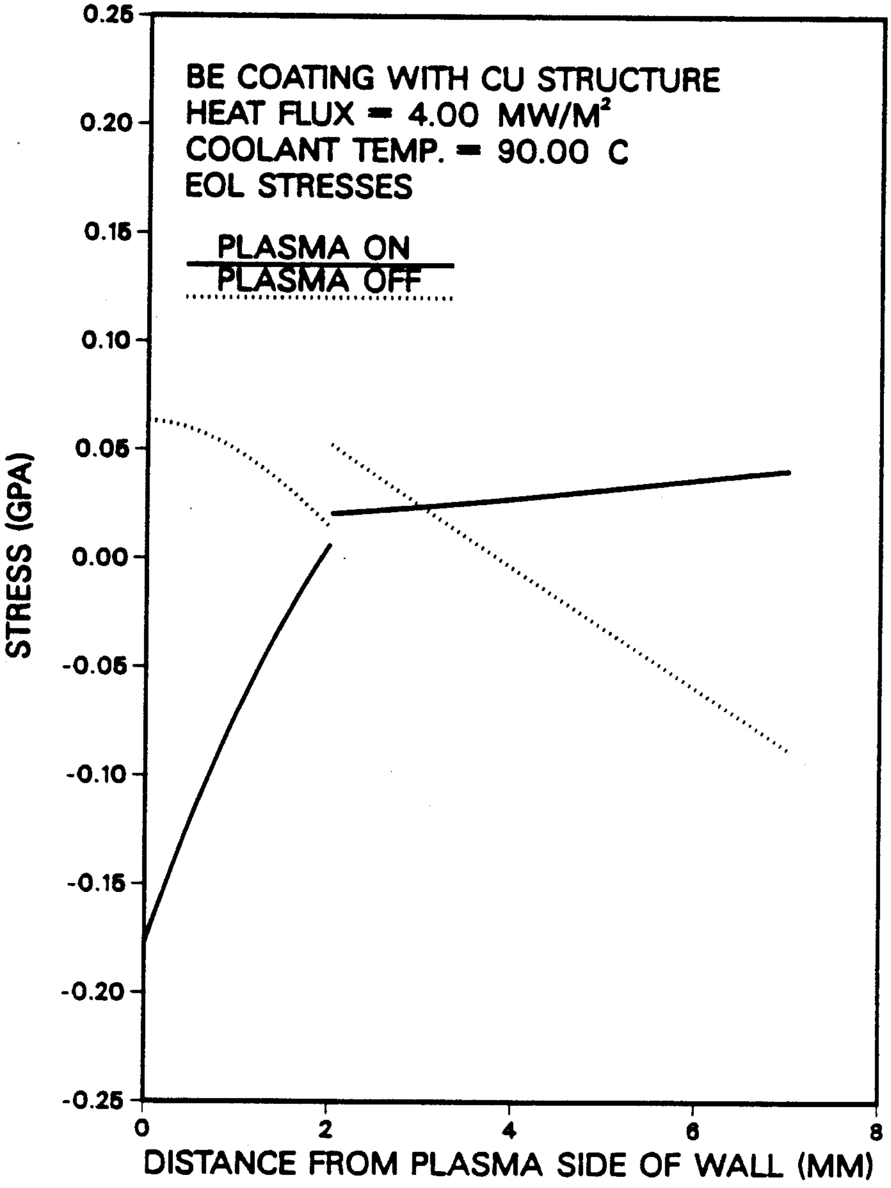

Figure 5.5. Stress distribution after about 20 years.

no membrane loads, Equation 5.26. If one then considers the inelastic strains to arise from thermal, creep, and swelling strains, Equation 5.27 can be derived. Equation 5.27 assumes isotropic material properties and strain rates. Given Equation 5.27 along with appropriate strain models for beryllium and copper, the stress distribution through a duplex wall exposed to a plasma environment (Figure 5.2) is calculated. It is found that the initial stress distribution (Figure 5.4) quickly evolves with time due to creep relaxation and swelling. After a period of about 20 years, a significantly different stress distribution exists.

References

[5.1.] Watson, R. D., Peterson, R. R., and Wolfer, W. G., The Effect of Irradiation Creep, Swelling, Wall Erosion, and Embrittlement of the Fatigue Life of a Tokamak First Wall, *Journal of Nuclear Materials* **103** 97 (1981).

[5.2.] Mattas, R. F., Fusion Component Lifetime Analysis, ANL/FPP/TM-160 (1982).

[5.3.] Mircea, S., *Applications of Finite Difference Equations to Shell Elements*, Pergamon Press (1967).

[5.4.] Glasgow, B. B. and Wolfer, W. G., *Modeling of Void Swelling in Irradiated Steels* **ASTM-STP-870**, to be published.

[5.5.] Wolfer, W. G. and McCarville, T. W., *Swelling of Beryllium*, to be published.

[5.6.] Ghoniem, N., private communication.

[5.7.] Frost, H. J. and Ashby, M. F., *Deformation-Mechanism Maps*, Pergamon Press (1982).

[5.8.] Wolfer, W. G., *Correlation of Radiation Creep Theory with Experimental Evidence*, Journal of Nuclear Materials **90** (1980) 175–192.

[5.9.] Olander, D. O., *Fundamental Aspects of Nuclear Reactor Fuel Elements*, **TID-26711-P1** (1976).

Chapter 6

LIFETIME COMPARISON OF FERRITIC TO 316 STAINLESS STEEL USING LINEAR ELASTIC FRACTURE MECHANICS

6.1. Introduction

Both experimental [6.1] and theoretical [6.2] work on 316 austenitic stainless steel show a long term swelling rate of about 1%/dpa. For ferritic steel, however, initial experimental work [6.1] shows a swelling rate of about 0.1%/dpa; theoretical work [6.2,6.3] predicts a maximum swelling rate of about 0.3%/dpa. Because of the much lower swelling rate of ferritic steels, these steels are being considered as an alternate material to 316 austenitic stainless steel. Another advantage of ferritic steels is their much reduced thermal stresses. Ferritic steel is a better thermal conductor than 316 austenitic stainless steel, and has a lower coefficient of thermal expansion. Because of these better thermophysical properties, the cyclic stresses which arise because of cyclic heat flux from the plasma (plasma-on / plasma-off cycles) are reduced. The reduction in cyclic stress is directly responsible for the improved fatigue crack growth performance of ferritic steel over 316 austenitic stainless steel.

Any lifetime analysis must consider the stress distribution through the structure as well as how the stresses will evolve with time due to stress relaxation and swelling. There have only been a handful of studies done for stress distribution evolution of fusion reactor high heat flux structures. Besides the work discussed in a previous chapter, two recent and complete studies were done by Mattas [6.4] and Watson *et al.* [6.5]. The results indicate that in modeling the stress evolution in a high heat flux fusion environment both creep relaxation and differential swelling must be included. The stress distribution model used in the lifetime analysis is based on the model discussed in a previous chapter. The model includes the effects of membrane loads, thermal and irradiation creep, differential swelling, and thermal expansion. The results of the stress distribution model are used as input into a crack propagation model. The end-of-life of the structure is assumed to occur when a pre-existing crack propagates through the wall resulting in a breach of the pressure boundary. Early work done by Cramer *et al.* [6.6] identified crack growth as the life limiting failure mechanism in tokamak reactors.

Previous to this work, the most complete work on crack propagation in fusion reactor first walls has been done by Watson *et al.* [6.5]. Watson *et al.* modeled a 316 austenitic stainless steel tokamak reactor first wall. The results indicate that fatigue crack growth is the dominant crack growth mechanism. Fatigue crack growth causes an initially small crack to grow either completely through the wall in a slow manner or partially through the wall until the crack reaches a critical size for brittle fracture. Both modes result in failure; however, brittle fracture may be much more catastrophic in terms of damage to the fusion reactor itself and the present analysis distinguishes the two failure modes. The lifetime analysis model discussed in this chapter is a continuation of the model developed by Watson *et al.* [6.5]. Improvements to the model include an improved stress analysis, the incorporation of ferritic steel properties, and more accurate numerical integration procedures.

6.2. Stress Analysis

The first wall of a fusion reactor will be exposed to several adverse conditions. Not only will membrane loads and bending moments exist but there will be a high neutron flux, high temperatures and temperature gradients, differential swelling, and thermal and irradiation creep. All of the above mentioned conditions are included in the two dimensional stress distribution evolution model. Since most fusion first wall designs specify a thin walled structure because of the high heat flux, the stress state is assumed to be plane. Furthermore, in order to conservatively predict the magnitude of the stresses, a plate element constrained from bending but free to expand is assumed to represent the most critical part of the first wall. This generic element of the first wall structure is shown in Figure 6.1.

For a plate element of thickness h free to bend and expand, one of the principal stresses can be given by

$$\begin{aligned}\sigma_x(z) = \frac{N_x}{h} + \frac{12M_x z}{h^3} + \frac{E}{(1-\nu^2)h}\int_{-\frac{h}{2}}^{\frac{h}{2}}(e_x + \nu e_y)dz \\ - \frac{E}{(1-\nu^2)}(e_x + \nu e_y) + \frac{12Ez}{(1-\nu^2)h^3}\int_{-\frac{h}{2}}^{\frac{h}{2}}(e_x + \nu e_y)z dz \quad (6.1)\end{aligned}$$

where the first two terms represent the elastic stress due to membrane loads N_x and bending moments M_x. The last three terms are due to the inelastic strains, e_x and e_y, such as thermal expansion, swelling, and creep. E is

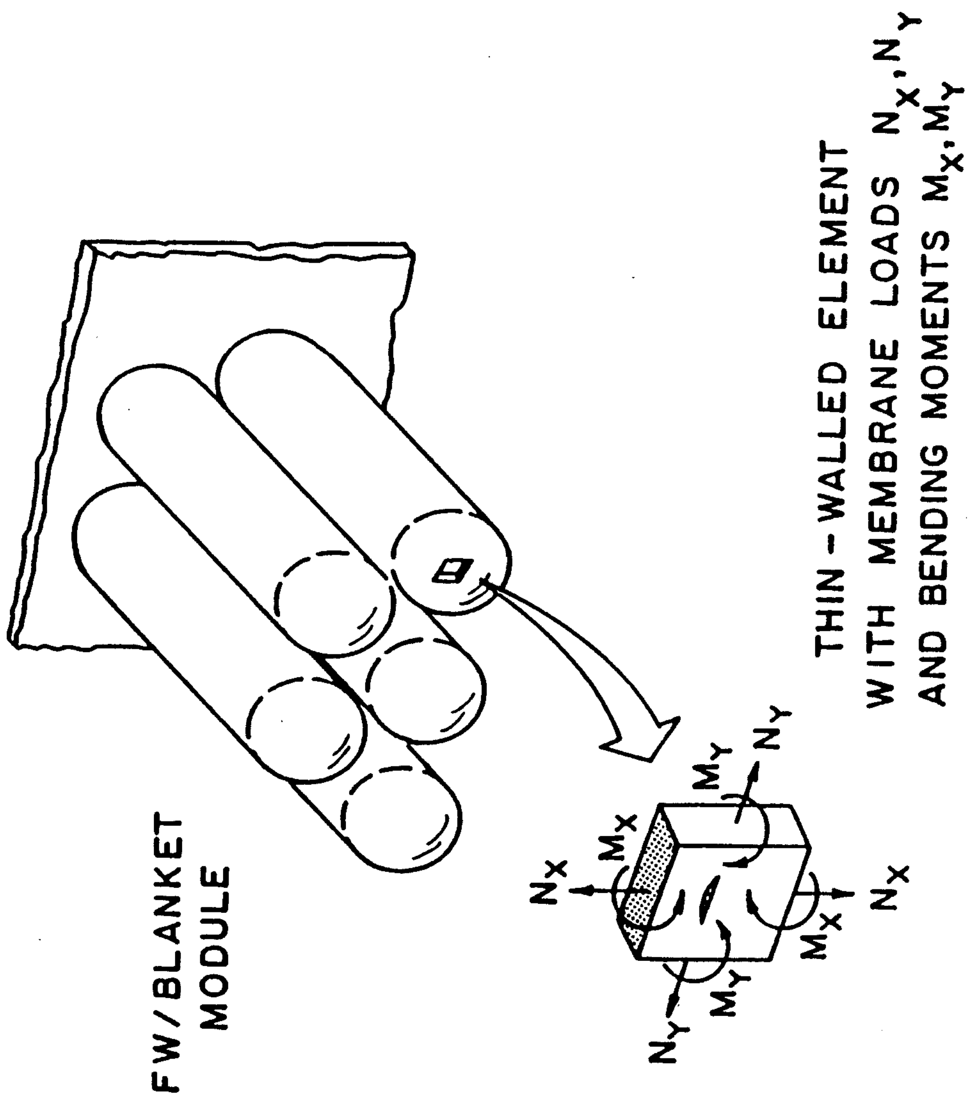

Figure 6.1. Generic first wall plate element model from the tip of a blanket module.

Young's modulus and ν is Poisson's ratio. For a plate constrained from bending the above equation is reduced to

$$\sigma_x(z) = \frac{N_x}{h} + \frac{E}{(1-\nu^2)h}\int_{-\frac{h}{2}}^{\frac{h}{2}}(e_x + \nu e_y)dz - \frac{E}{(1-\nu^2)}(e_x + \nu e_y) \qquad (6.2)$$

The stress distribution through the plate can be followed with time by calculating how the inelastic strains develop with time. In this lifetime analysis, however, the stress analysis results of a previous chapter are used

$$\sigma_x = \frac{E}{W}[X_i + \nu X_j] - E[e_i^i + \nu e_j^i] \qquad (6.3)$$

where X and W are defined in a previous chapter.

Inelastic strains arise from three sources: 1) thermal strains, 2) creep strains, and 3) swelling strains. Thermal strains are due to thermal expansion of the structure when the plasma is on. The thermal strain is found from the expression $e_{th} = \alpha(T - T_o)$ where α is the coefficient of thermal expansion and T_o is the reference temperature. There is, however, another aspect of thermal strains and the interrelation between thermal strain and creep. Initially the only inelastic strain is the thermal strain resulting in compressive stress at the plasma surface and tensile stress at the coolant surface. Over time as the stresses begin to relax by creep, the plasma-on stresses are reduced in magnitude and, accordingly, the plasma-off stresses increase in magnitude eventually resulting in a small plasma-on stress but a large plasma-off stress. The plasma-off stress is now tensile on the plasma surface and compressive on the coolant surface. An example of the stress evolution for ferritic steel is shown in Figure 6.2. The creep strain is calculated by numerically integrating the thermal and irradiation creep strain rates. Using the relationships proposed by Gelles *et al.* [6.7], irradiation creep is taken as the sum of a radiation-induced creep and a swelling-induced creep as $\dot{\epsilon}_c^{irr} = B\sigma^n\phi + D\dot{S}\sigma$ where B, n, and D are constants, ϕ is the dose rate, and $\dot{S}$ is the swelling rate. Gelles *et al.* also propose a thermal creep rate of $\dot{\epsilon}_c^{th} = A/(1 - ABt)$ where A and B are functions of temperature and stress, and t is time.

For ferritic steel the stresses evolve as shown in Figure 6.2; the swelling strains are negligible in this case compared to thermal and creep strains. However, if swelling strains cannot be ignored as in the case of 316 austenitic stainless steel, a different stress distribution evolves. As swelling strains build up compressive stresses for plasma-on conditions increase on the plasma side; likewise, equilibrating tensile stresses increase on the coolant side. Now the interrelation between thermal, creep, and swelling strains result in a significantly different stress distribution later in life as is shown in Figure 6.3. An additional interesting point on the stress evolution in 316 austenitic stainless steel is illustrated in Figure 6.4. Up to 1 year of full power operation the stresses relax by creep. But, at approximately 1 year (the incubation period for the onset of swelling) the swelling strains begin and increase until a steady state is reached at about 3 years. This type of behavior is not predicted for ferritic steel because of the very low swelling rate and the extensive incubation period. The swelling rate for ferritic steel has been expressed in the

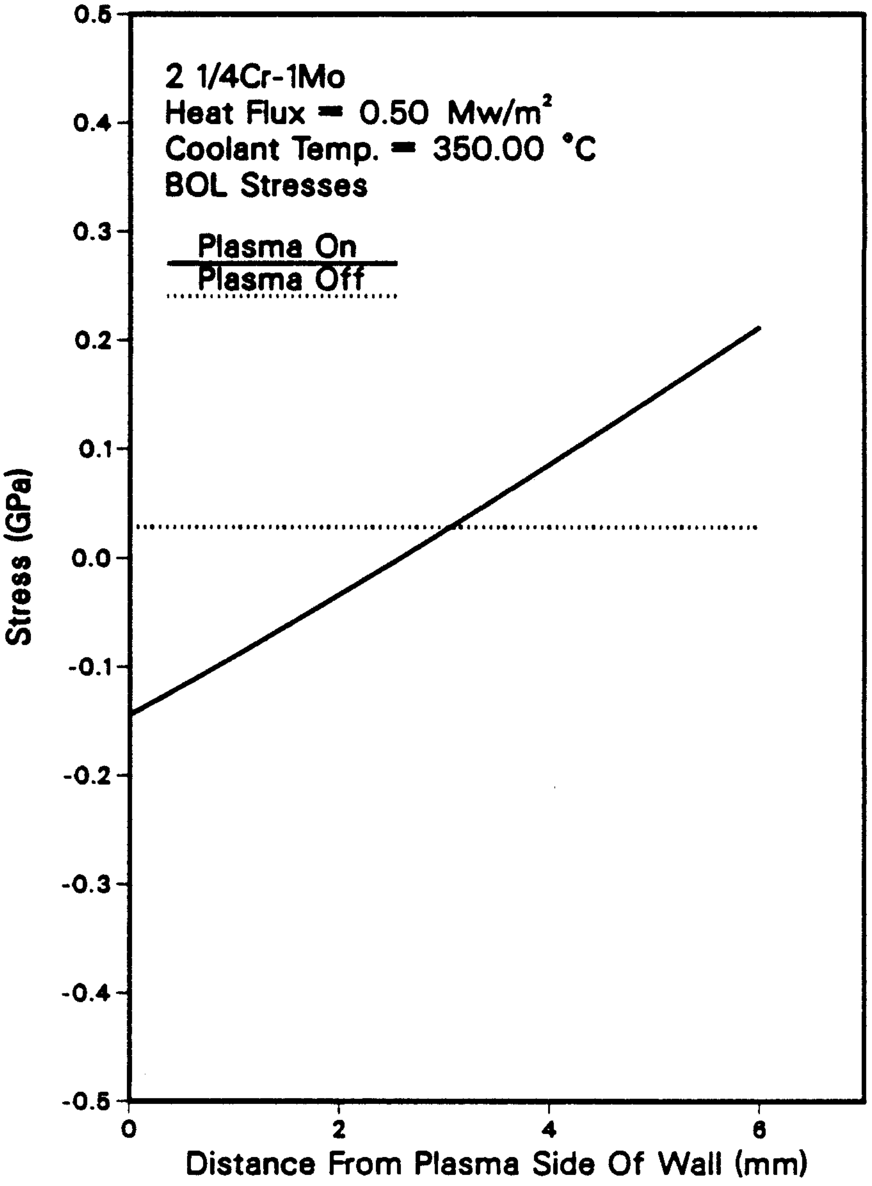

Figure 6.2a. First wall stress distribution at beginning-of-life for $2\frac{1}{4}$Cr–1Mo.

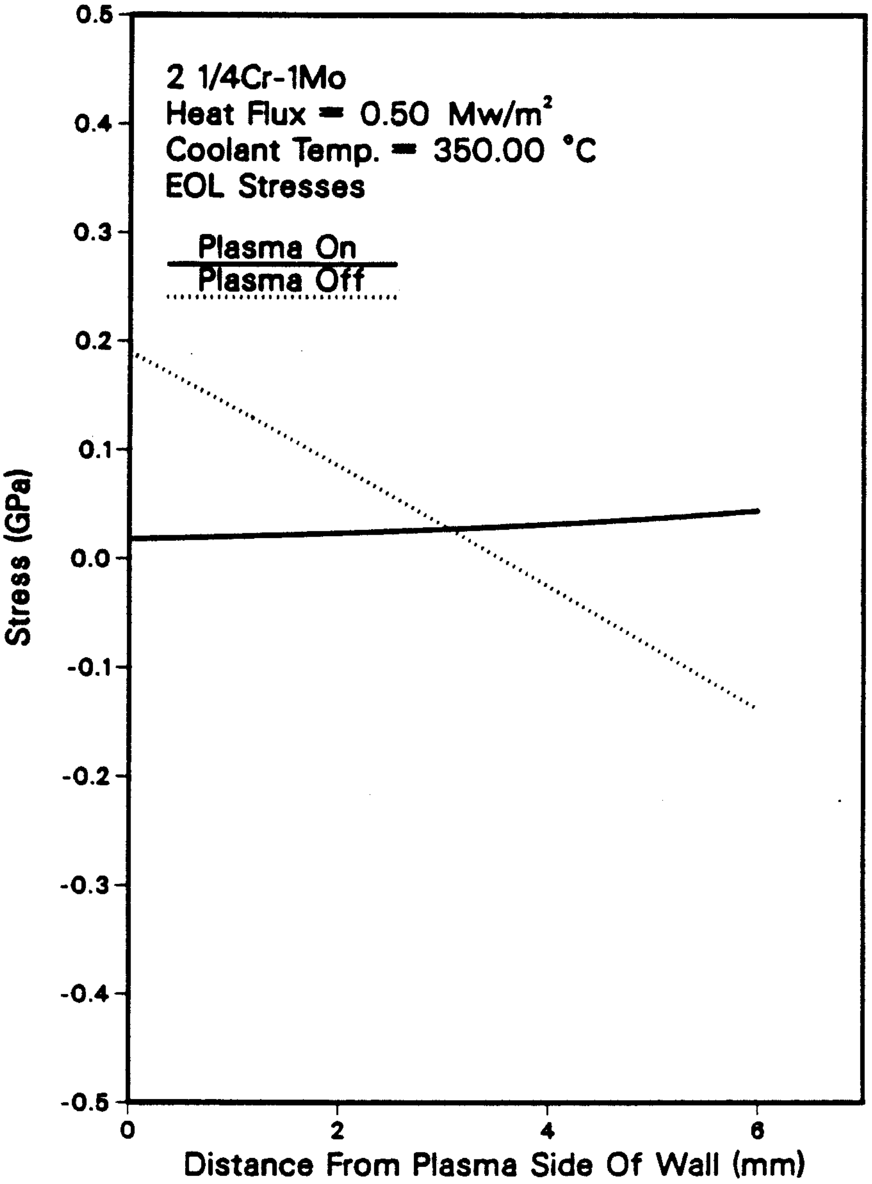

Figure 6.2b. First wall stress distribution at at end-of-life for $2\frac{1}{4}$Cr–1Mo.

empirical form

$$\dot{S} = R\phi\left[1 - \frac{1}{1+e^{-\kappa}}\right] + De^{-\chi}\phi \tag{6.4}$$

by Gelles *et al.* [6.7]. R and D are constants κ and χ are functions of time, dose, and temperature.

6.3. Failure Model

A crack no matter how small could grow to sufficiently large size to compromise the integrity of the first wall. In fact, Cramer *et al.* [6.6] first identified crack growth as the limiting failure mechanism in 316 austenitic stainless steel tokamak first walls. End-of-life is presumed when a pre-existing crack propagates through the plate causing a vacuum breach of the first wall. The mode of propagation can be either a slow crack propagation which will eventually cause a leak through, or a rapid brittle fracture potentially causing catastrophic failure. In most cases a combination of the two modes occur. Early in life when the assumed crack is small, propagation is slow. However, as the crack increases in size the linear elastic fracture mechanics (LEFM) limit is reached and brittle fracture occurs. The present model allows the crack to grow independently in depth and width permitting elliptical cracks to be modeled.

Brittle fracture occurs whenever the stress intensity factor K exceeds the plane strain fracture toughness K_{Ic}. The plane strain fracture toughness is a material property allowed to change with the irradiation exposure. While the "plane stress" fracture toughness is not generally regarded as a material

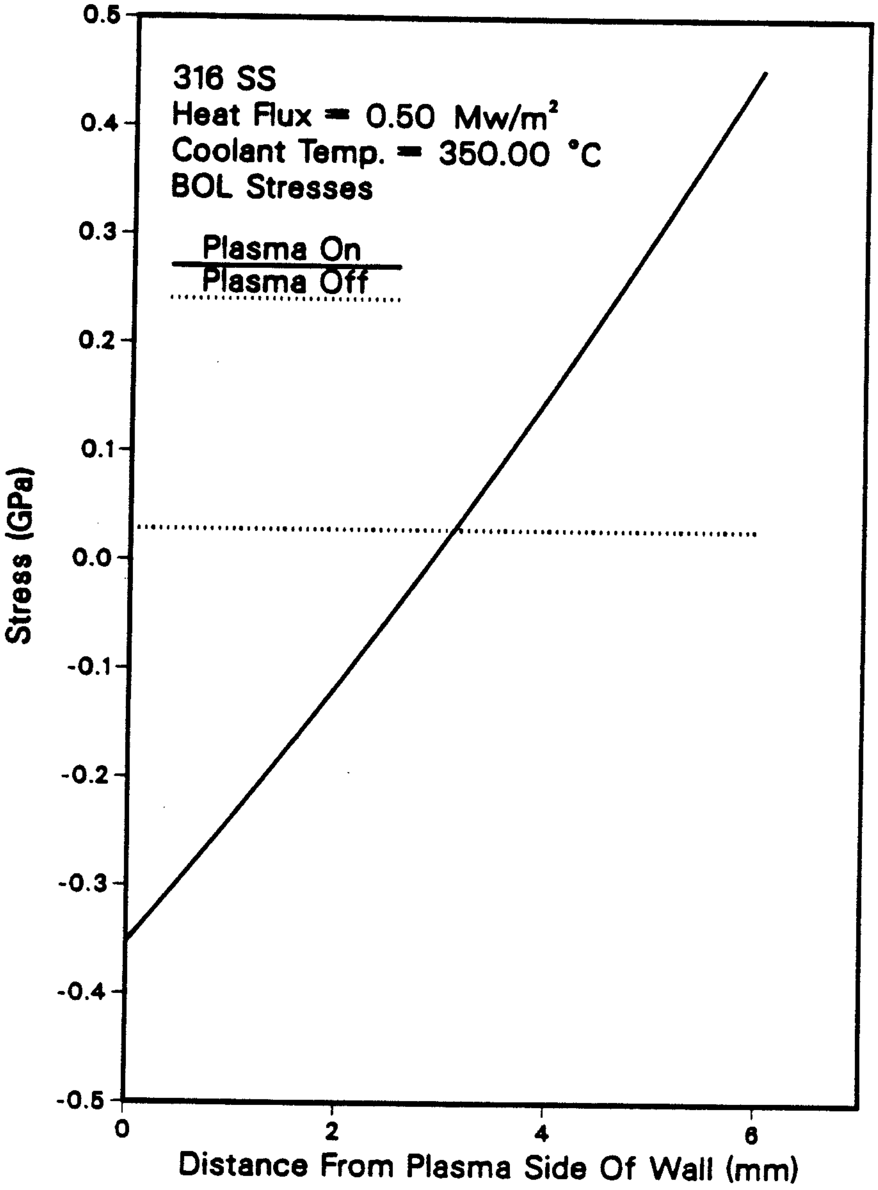

Figure 6.3a. First wall stress distribution at beginning-of-life for 316 stainless steel.

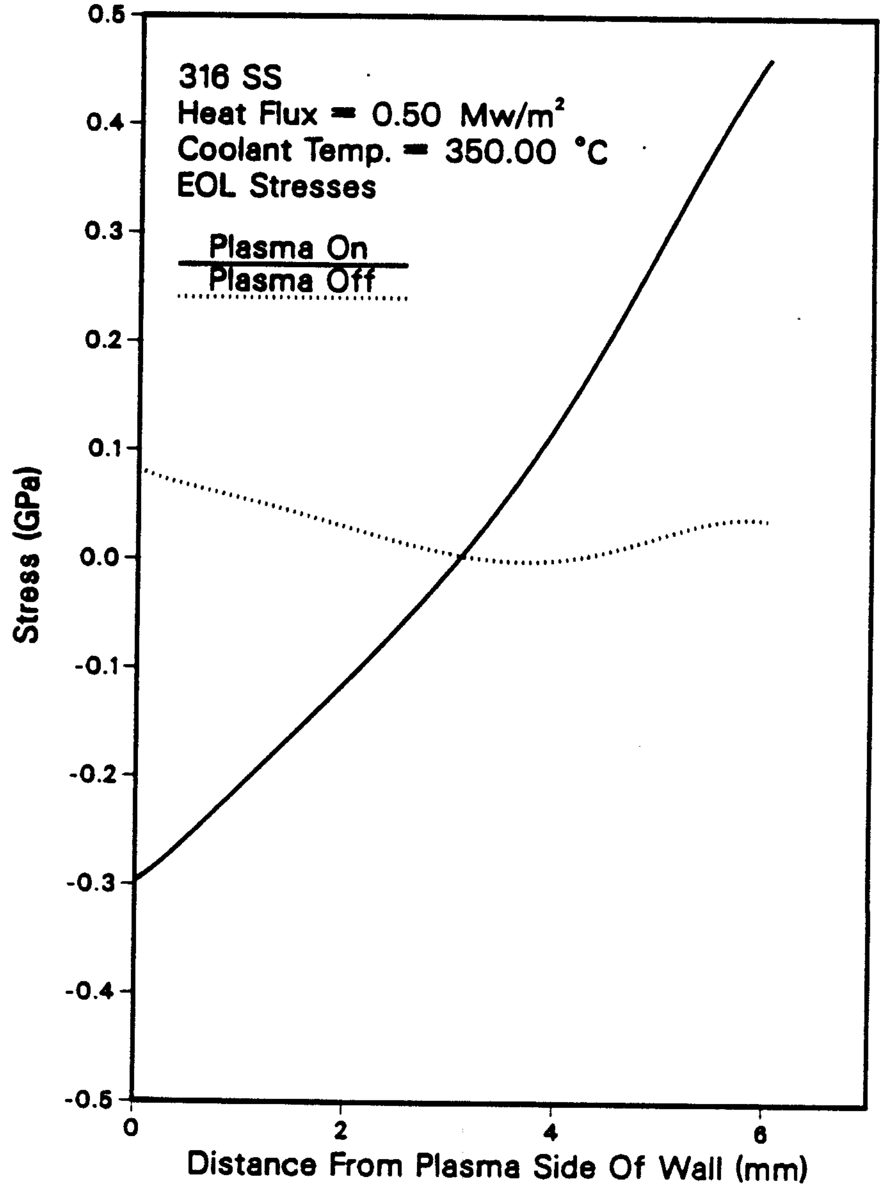

Figure 6.3b. First wall stress distribution at end-of-life for 316 stainless steel.

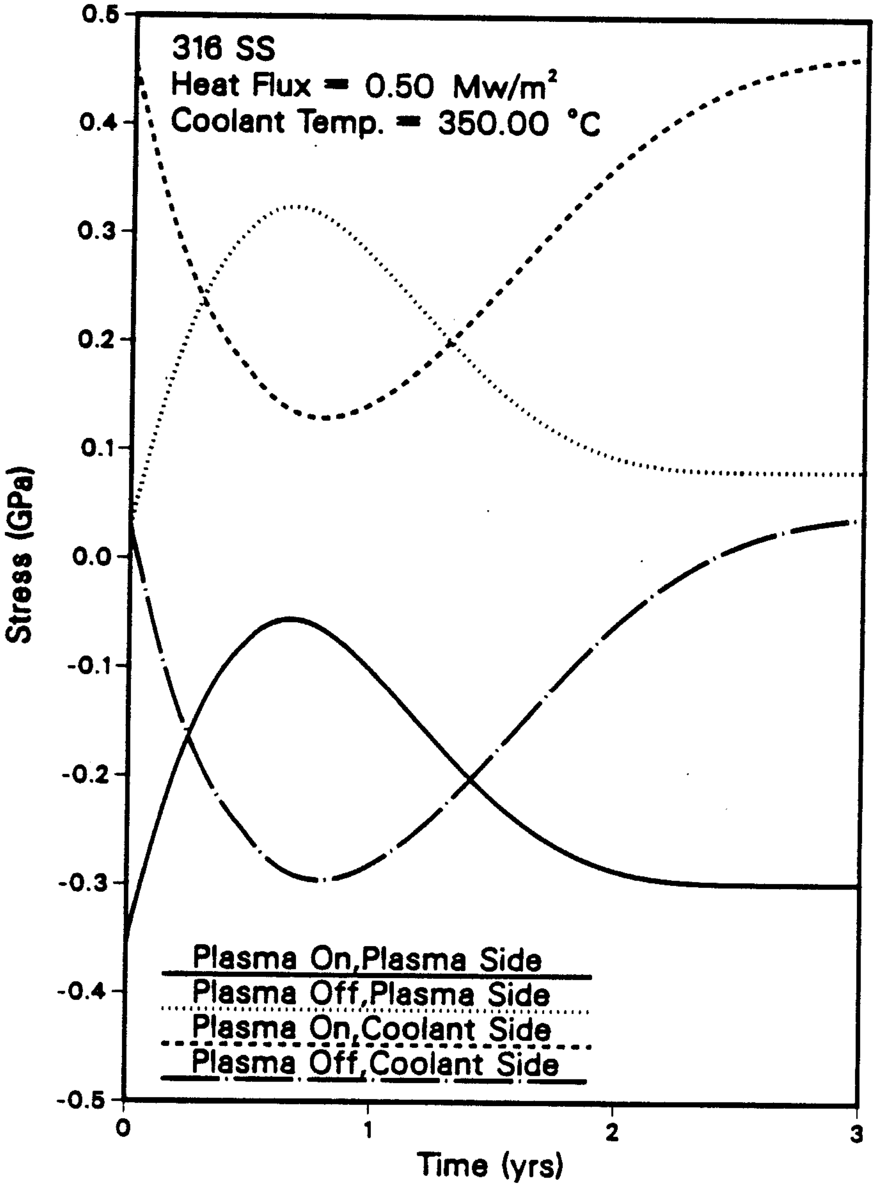

Figure 6.4. First wall stresses as a function of time for 316 stainless steel.

property, it is known to be higher than the plane strain value. The model conservatively uses the plane strain value even through the stress distribution at the crack tip may be plane stress. For some metals (like body centered cubic ferritic steel) K_{Ic} is a strong function of temperature exhibiting a sharp drop in fracture toughness at the ductile to brittle transition temperature (DBTT). Other metals (like face centered cubic 316 austenitic stainless steel) do not exhibit a DBTT; but K_{Ic} is still a mild function of temperature. Irradiation affects the fracture toughness of most metals by making the metals more brittle thereby degrading the fracture toughness. Also for those metals exhibiting a DBTT, irradiation tends to move the DBTT to higher temperatures. To be conservative in modeling a ferritic steel first wall, the lower shelf fracture toughness for ferritic steel is used at all temperatures and a value of 30 $\mathrm{MPa}\sqrt{\mathrm{m}}$ is assumed. The fracture toughness of irradiated 316 austenitic stainless steel is similar to the lower shelf fracture toughness of irradiated ferritic steel and the same value is also assumed.

In the present analysis it is postulated that a semi-elliptical surface crack exists on either the plasma or the coolant side and that the element containing the crack is subject to a combination of membrane loads and bending loads. The bending loads arise from the various inelastic strains. The expression for the stress intensity factor [6.8] for this crack is

$$K = (M_m \sigma_m + M_b \sigma_b) \frac{1}{\sqrt{Q}} \sqrt{\pi a} \tag{6.5}$$

where a is the crack depth, Q is the flaw shape factor, $M_{m,b}$ are the membrane and bending correction factors, and $\sigma_{m,b}$ are the membrane and bending stresses. In general, $M_{m,b}$ and Q are function of plate thickness, crack depth, and crack width. The model uses expressions for $M_{m,b}$ as given by Newman *et al.* [6.9].

Slow crack propagation proceeds by two mechanisms: 1) creep crack growth and 2) fatigue crack growth. Creep crack growth occurs at high temperatures when the crack tip is in a tensile stress field. The expression for creep crack growth rate is of the form

$$\frac{da}{dt} = D_o e^{-Q/RT} (K_{max})^P \tag{6.6}$$

D_o, Q, R, and P are constants. Fatigue crack growth is the dominant crack growth mechanism for tokamaks unless the cyclic stress frequency were drastically reduced, as might be the case for a steady state device. The fatigue crack growth rate for ferritic steel is modeled by the equation

$$\frac{da}{dN} = Cf \frac{[\Delta K^n - \Delta K_{th}^n]}{[1 - (\lambda f \Delta K / K_{Ic})^\lambda]} \tag{6.7}$$

where da/dN is the increase in crack dimensions with each cycle; C and n are constants, f is the ratio of Young's modulus at room temperature to the actual Young's modulus, ΔK is the cyclic stress intensity difference $(K_{max} - K_{min})$, ΔK_{th} is the threshold cyclic stress intensity below which no fatigue crack growth occurs, and $\lambda^{-1} = (1 - R)$ where $R = K_{min}/K_{max}$. Equation 6.7 above was used to correlate the experimental data of Suresh *et al.* [6.10]. In particular, the threshold cyclic stress intensity ΔK_{th} data are those given in that Reference. The threshold value is both a function of the R

ratio (K_{min}/K_{max}) and the environment. Using the data for a dry hydrogen environment, the data can be correlated with the following relationship

$$\Delta K_{th} = \begin{cases} 3 + 10(.25 - R), & \text{for } R < .25 \\ 3, & \text{for } R \geq .25 \end{cases} \tag{6.8}$$

which is shown is Figure 6.5. The results for fatigue crack growth rate are shown in Figure 6.6.

6.4. Discussion

The method for the present lifetime analysis is illustrated in Figure 6.7. The stress analysis is carried out with a code called TSTRESS; the results of TSTRESS are input into the crack propagation model WISECRACK. The input parameters for TSTRESS include wall thickness, heat flux, nuclear heating, coolant temperature, and inelastic strain constituitive laws. Besides the results of TSTRESS, the WISECRACK input includes initial flaw dimensions (depth and width), K_{Ic} as a function of temperature and dose, and the crack growth rates for fatigue and creep.

For the case of a first wall made of 316 austenitic stainless steel, Figures 6.3 and 6.4 show the stress distribution and evolution. It can be seen in Figure 6.4 that for times greater than about 3 years, the plasma side of the wall is subject mostly to tensile stresses. For long times then, it is the coolant side which seems most sensitive to crack propagation. If, however, failure occurs within less than 3 years, it is not obvious which side of the wall is most sensitive to crack growth. In the particular case shown here, it is predicted that a crack on the coolant side is more life limiting than a crack

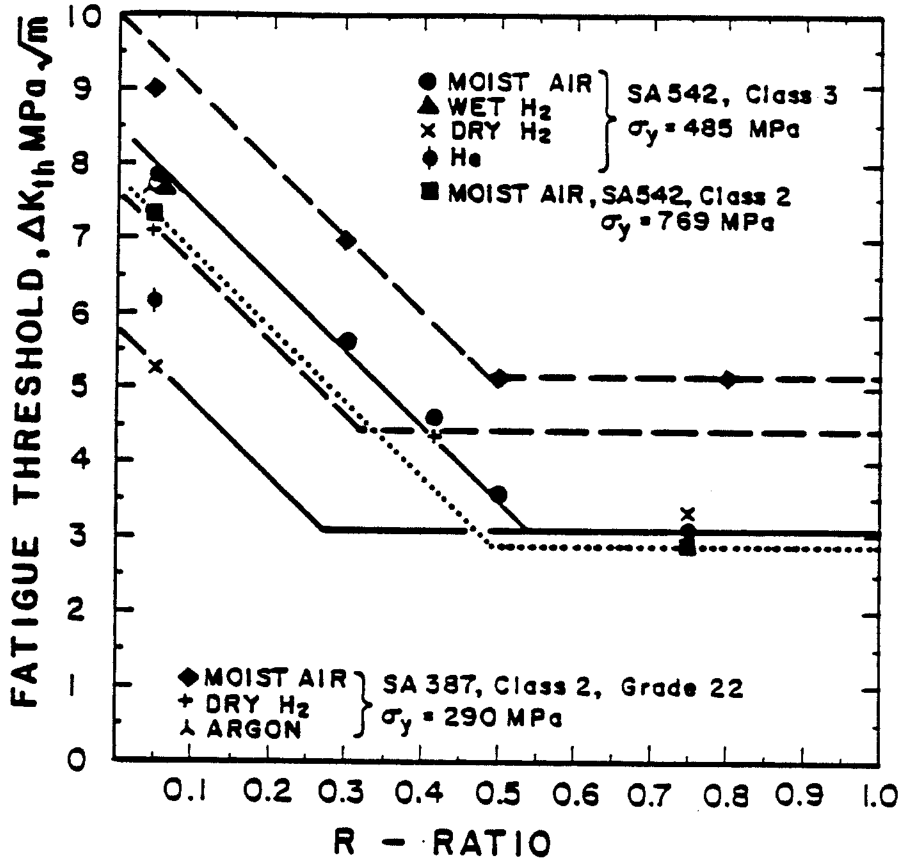

Figure 6.5. Fatigue crack growth threshold versus R ratio showing the effect of environment.

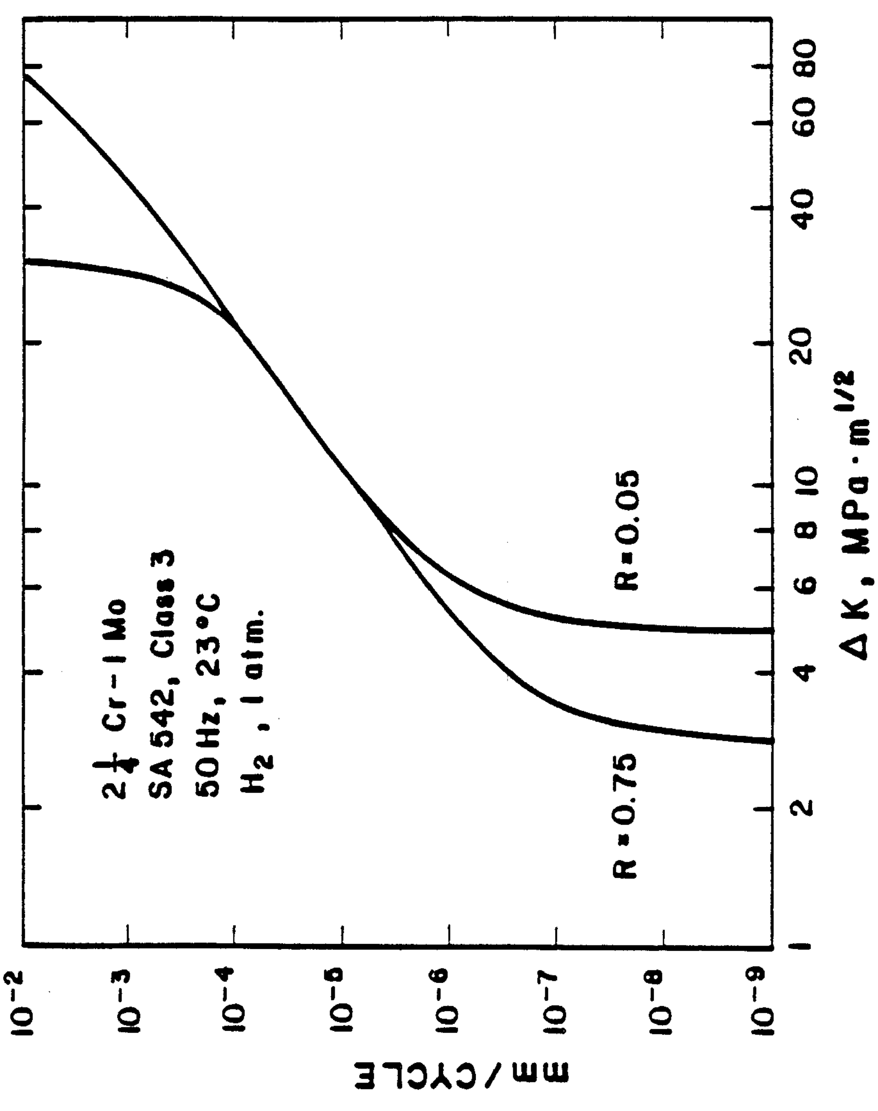

Figure 6.6. Fatigue crack growth rates versus ΔK for $2\frac{1}{4}$Cr–1Mo.

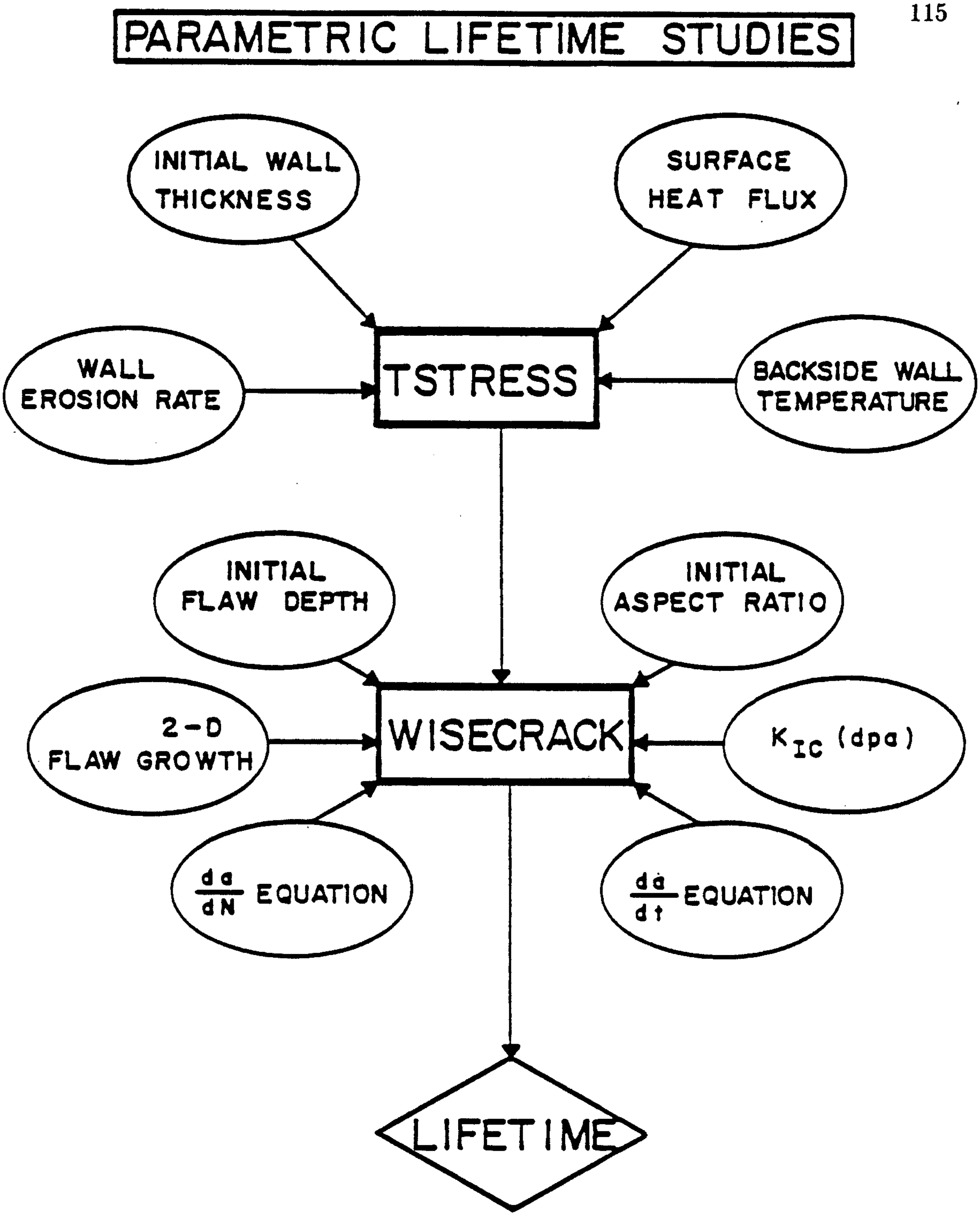

Figure 6.7. Illustration of model used for lifetime calculations.

on the plasma side. Figure 6.8 shows the crack depth versus time for a crack on the coolant side. The length of time for a 1mm crack to propagate through the wall is approximately 2 years. The mode of failure is brittle fracture; the failure occurs when the crack dimensions are such that K exceeds K_{Ic}.

For ferritic steel, Figure 6.2 shows the stress distribution at beginning-of-life and at end-of-life. The end-of-life distribution is, in fact, obtained in less than $\frac{2}{10}$ of a year because of the rapid creep relaxation and negligible swelling. As illustrated in Figure 6.2, the plasma side experiences the tensile cyclic stresses. The model predicts then that a crack on the plasma side is more critical than a crack on the coolant side. Under the same conditions as for 316 austenitic stainless steel, no failure is predicted for ferritic steel. In fact, the initial crack depth must be greater than about 3 times the initial crack depth for 316 austenitic stainless steel to get a failure within 30 years. Figure 6.9 illustrates the crack propagation for ferritic steel.

While the present lifetime analysis does not take all potential life limiting factors into account, it models in detail the crack propagation. Along with crack propagation, the effects of irradiation on K_{Ic} is also included, and an accurate evaluation of stress distribution and its evolution is accomplished. Based on this somewhat limited analysis however, it is clear that ferritic steels have a great potential as a first wall material to achieve the long lifetimes desired for future fusion reactors. One of the major shortcomings of this brittle fracture model is the omission of plasticity effects. For low yield strength materials such as ferritic steel, there is the possibility of failure by

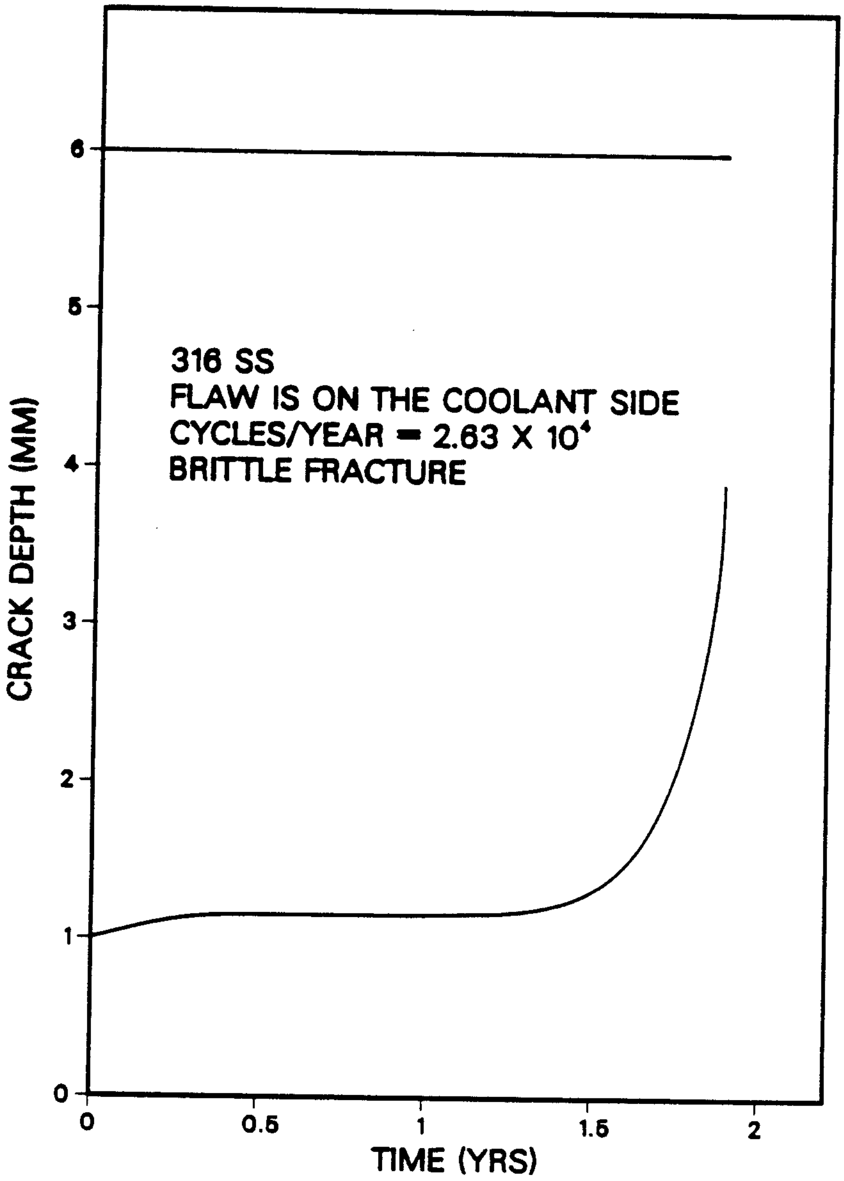

Figure 6.8. Crack depth into first wall versus time for 316 stainless steel.

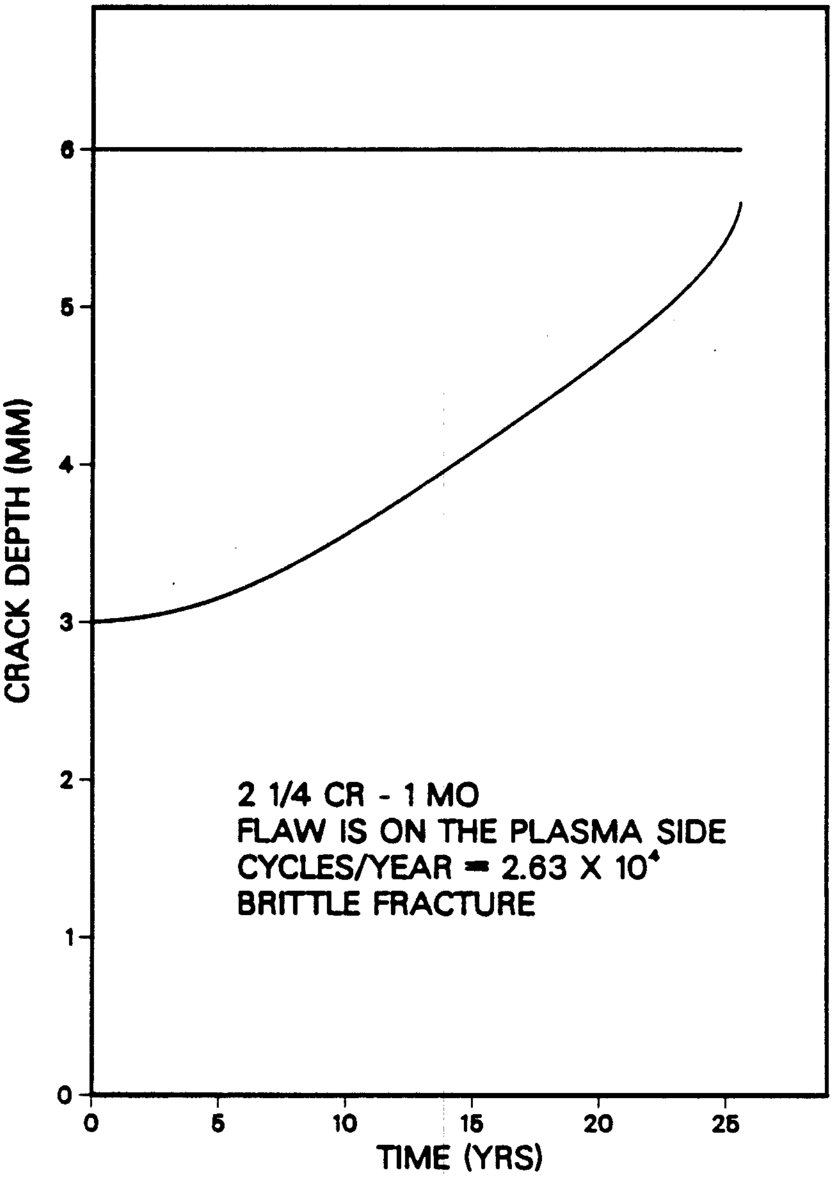

Figure 6.9. Crack depth into first wall versus time for $2\frac{1}{4}$Cr–1Mo.

plastic tearing or collapse. A future chapter will discuss plastic collapse and how to incorporate this failure mode in the lifetime analysis.

References

[6.1.] Garner, F. A., **ASTM-STP-870**, to be published.

[6.2.] Glasgow, B. B. and Wolfer, W. G., **ASTM-STP-870**, to be published.

[6.3.] Sniegowski, J. J. and Wolfer, W. G., *Proceedings of the Topical Conference of Ferritic Alloys for Use in Nuclear Energy Technologies* (Editors: J. W. Davis and D. J. Michel), page 579, The Metallurgical Society AIME, Warrendale (1984).

[6.4.] Mattas, R. F., Fusion Component Lifetime Analysis, ANL/FPP/TM-160 (1982).

[6.5.] Watson, R. D., Peterson, R. R., and Wolfer, W. G., The Effect of Irradiation Creep, Swelling, Wall Erosion, and Embrittlement of the Fatigue Life of a Tokamak First Wall, *Journal of Nuclear Materials* **103** 97 (1981).

[6.6.] Cramer, B. A., Davis, J. W., Kinder, R. C., and Bowers, D. A., An Approach For Determining the Lifetime of a First Wall Structure in a Tokamak Reactor, **CONF-760935-P4**, *Proceedings of the Second Topical Meeting on the Technology of Controlled Nuclear Fusion*, Richland, WA (1976).

[6.7.] Gelles, D. S. and Puigh, R. J., Evaluation of Ferritic Alloy Fe-2$\frac{1}{4}$Cr-1Mo after Neutron Irradiation – Irradiation Creep and Swelling, **HEDL 7405** (1983).

[6.8.] ASME Boiler and Pressure Vessel Code, Section XI, *Rules for Inservice Inspection of Nuclear Power Plant Components*, Appendix A, *Evaluation of Flaw Indicators* (1977).

[6.9.] Newman, J. C. and Raju, I. S., Analysis of Surface Cracks in Finite Plates Under Tension or Bending Loads, **NASA Technical Paper 1578** (1978).

[6.10.] Suresh, S., Toplosky, J., and Richie, R. O., Environmentally Affected Near Threshold Fatigue Crack Growth in Steels, **ASTM-STP-791** (1983).

Chapter 7

INCORPORATING PLASTIC COLLAPSE INTO THE LINEAR ELASTIC FRACTURE MECHANICS METHODOLOGY

7.1. Introduction

In the last few years increasing attention has been given to failure analysis, particularly with emphasis to Elastic–Plastic Fracture Mechanics (EPFM). Several failure assessment criteria have been proposed including: 1) K_{Ic}, 2) J-integral, 3) Crack Opening Displacement (COD), 4) R-curve, 5) Plastic yield criterion. Several of these criteria are reviewed by Larsson [7.1]. The J-integral, COD, and R-curve are either analytically difficult for a general case or are based on empirical studies. K_{Ic} is a valid failure criterion for brittle cracked structures in a state of plane strain but is not correct for highly plastic structures. The K_{Ic} failure criterion was used in a previous chapter to determine the lifetime of cracked first wall structures. Plastic yield criterion is valid for plastic behavior of smooth, uncracked structures.

From an engineering viewpoint, a failure criterion should be valid over a wide range of conditions (brittle–plastic, plane stress–plane strain) and should be computationally as simple as possible. From the brief discussion above, it seems that the union of K_{Ic} and a plastic yield criteria would meet these conditions at the extremes of brittle and plastic behavior, respectively.

The computational model used in work documented in a previous chapter predicted failure to occur when either the crack slowly propagated through the wall eventually causing a leak-through of the coolant into the plasma chamber or when the stress intensity factor K exceeded the plane strain fracture toughness K_{Ic} resulting in rapid brittle fracture. While K_{Ic} is conservative for brittle fracture, it is not entirely appropriate. First, since the first wall is expected to be rather thin ($\sim$ 10mm), the use of the plane strain fracture toughness may not be appropriate. The ASTM code [7.2] pertaining to the validity of plane strain fracture states that if $t > 2.5\left(\frac{K_{Ic}}{\sigma_y}\right)^2$, where t is the thickness, the structure is in a state of plane strain near the crack tip. Substituting unirradiated material properties for 316 stainless steel, one finds $2.5\left(\frac{150}{600}\right)^2 \sim$ 16cm which is much greater than a typical first wall thickness of about 1cm. Therefore, the structure is not always in plane strain and K_{Ic} may not be the appropriate parameter for failure analysis. (It should be noted that highly irradiated 316 stainless steel 1cm thick is in a state of plane strain as the relation $2.5\left(\frac{30}{800}\right)^2 \sim$ .35cm indicates) Second, failure by plastic collapse was not modeled. Hence, one possible significant failure mode was ignored.

A revised failure criterion discussed below will consider plastic collapse as well as brittle fracture and will incorporate the two failure modes into one analytic expression. The incorporation of this failure mode into the lifetime analysis is a major improvement over the previous studies.

7.2. The Two Criteria Approach

In 1975 Dowling *et al.* [7.3] proposed a two criteria approach to failure assessment of structures containing defects. The approach assumes that failure occurs when either the applied stress reaches the failure stress based on LEFM ($K > K_{Ic}$), or the applied stress exceeds the plastic collapse stress based on plasticity theory using an appropriate failure criterion. There is, however, a sizeable transition between fully brittle and fully plastic conditions. To bridge the transition region, Dowling *et al.* used the results of Heald *et al.* [7.4] which showed that the transition region between brittle and plastic can be described by expanding on the Bilby–Cottrell–Swinden (BCS) strip yield model [7.5].

The BCS model treats a crack and the plastic zone ahead of the crack as a line of dislocation pile-ups. Then using a continuous distribution model for the dislocations, the size of the plastic zone and the displacement, or COD, at the crack tip can be calculated. The BCS model results are similar to the simpler Dugdale model [7.6] for the spread of plasticity, as expanded by Burdekin *et al.* [7.7]. The Dugdale model assumes a crack of length $2a$ normal to an applied stress σ_{app}. Plastic yielding then is assumed to take place over a length $c - a$ ahead of the crack tip (see Figure 7.1). The size of the plastic zone can be calculated by assuming a uniform stress σ_{app} over a crack of length $2c$ where $K = \sigma_{app}\sqrt{\pi c}$ and then assuming a stress equal to the yield stress σ_y applied along the plastic zone, $c - a$. It can be shown [7.7] that for a notched thin sheet under tension and using Westergaard type stress functions, $K = 2\sigma_y\sqrt{\frac{c}{\pi}}\cos^{-1}\left(\frac{a}{c}\right)$. The two expressions for K can be set equal to each other; and one obtains

$$\frac{a}{c} = \cos\left(\frac{\pi\sigma_{app}}{2\sigma_y}\right) \tag{7.1}$$

Then from the BCS model, Heald *et al.* utilized the following expression for the COD

$$\delta = 4\sigma_y c \frac{(1-\nu)}{\pi\mu} \ln\left(\frac{a}{c}\right) \tag{7.2}$$

where δ is the COD and μ is the shear modulus. Combining Equations 7.1 and 7.2 gives

$$\delta_c = 4\sigma_y c \frac{(1-\nu)}{\pi\mu} \ln\sec\left(\frac{\pi\sigma_f}{2\sigma_y}\right) \tag{7.3}$$

when the condition for failure is met; in this case σ_{app} is replaced by the failure stress σ_f, δ is replaced by the COD at failure δ_c. Rearranging Equation 7.3 results in

$$\sigma_f = \frac{2}{\pi}\sigma_y \cos^{-1}\exp\left(-\frac{\pi\mu\delta_c}{4(1-\nu)\sigma_y c}\right) \tag{7.4}$$

Using the results of Griffith [7.8], it can be shown that for plane strain conditions that

$$\sigma_f = \sqrt{\frac{2E\gamma}{\pi c(1-\nu^2)}} \tag{7.5}$$

where γ is the energy expended per unit area of crack surface created. This energy can also be related to the plastic work dissipated in reaching the COD according to

$$2\gamma = \sigma_y \delta_c \tag{7.6}$$

Next, one relates $\sigma_f\sqrt{\pi c}$ to a fracture toughness and obtains

$$K_{Ic} = \sqrt{\frac{E\sigma_y\delta_c}{1-\nu^2}} \tag{7.8}$$

Solving now for the critical COD gives

$$\delta_c = \frac{K_{Ic}^2(1-\nu^2)}{E\sigma_y} = \frac{K_{Ic}^2(1-\nu)}{\sigma_y 2\mu} \tag{7.9}$$

Combining Equation 7.4 and 7.9 the failure stress can be found

$$\sigma_f = \frac{2}{\pi}\bar{\sigma}\cos^{-1}\exp\left(-\frac{\pi K_{Ic}^2}{8\bar{\sigma}^2 c}\right) \tag{7.10}$$

where σ_y has been replaced by the flow stress $\bar{\sigma}$ ($\bar{\sigma} = .5(\sigma_y + \sigma_u)$, σ_u is the ultimate strength) which is a better measure of failure than σ_y for materials with work-hardening. Equation 7.10 was originally derived by Heald *et al.*. It is reassuring to note that in the limit of large K_{Ic}, $\sigma_f \rightarrow \bar{\sigma}$ and for small K_{Ic}, $\sigma_f \rightarrow \frac{K_{Ic}}{\sqrt{\pi c}}$.

In order to describe the failure of complex structures, Dowling *et al.* proposed rewriting Equation 7.10 as

$$\frac{L_f}{L_u} = \frac{2}{\pi}\cos^{-1}\exp\left(-\frac{\pi^2 L_k^2}{8L_u^2}\right) \tag{7.11}$$

where L_f is the failure load, L_u is the plastic collapse load, and L_k is the LEFM load limit. Figure 7.2 shows a plot of Equation 7.11 along with some experimental failure data reported by Dowling *et al.*

While Equation 7.11 can be used to predict failure, Harrison *et al.* [7.9] rewrote it to be

$$K_r = S_r\left[\frac{8}{\pi^2}\ln\sec\left(\frac{\pi}{2}S_r\right)\right]^{-1/2} \tag{7.12}$$

where $K_r = K/K_{Ic}$ and $S_r = \sigma/\sigma_p$ and σ_p is the plastic collapse stress which is a function of $\bar{\sigma}$, structure dimensions, and crack dimensions. Writing the failure condition in the form of Equation 7.12 is an attempt to separate brittle failure (the left-hand side) from plastic collapse (the right-hand side). Figure 7.3 shows a plot of K_r versus S_r at failure; and it is called the Failure

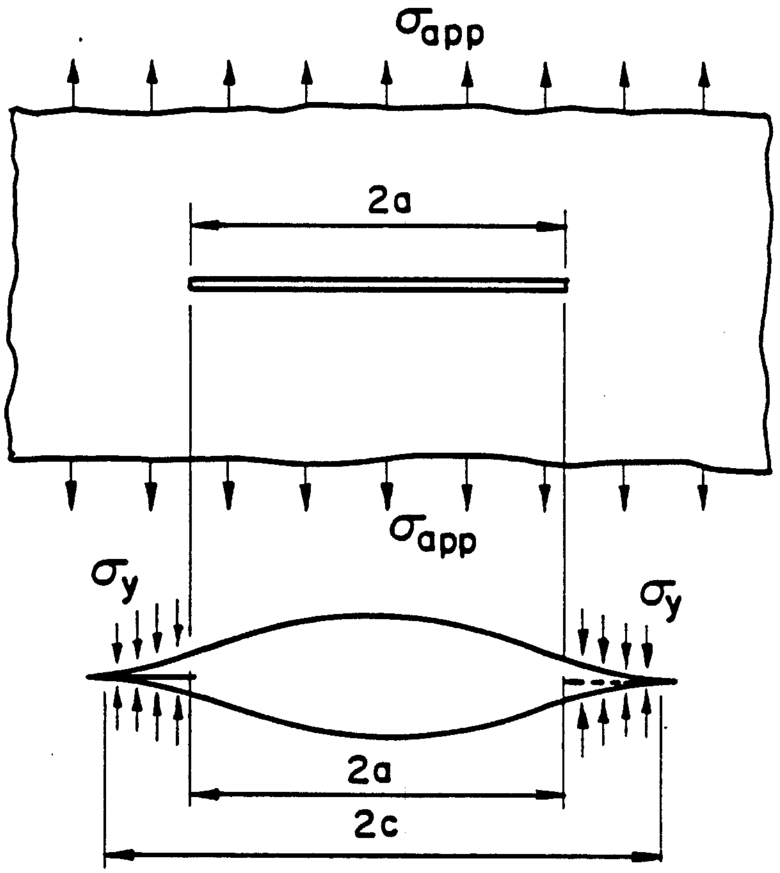

Figure 7.1. Illustration of the model used by Dugdale [7.6] to calculate the Crack Opening Displacement.

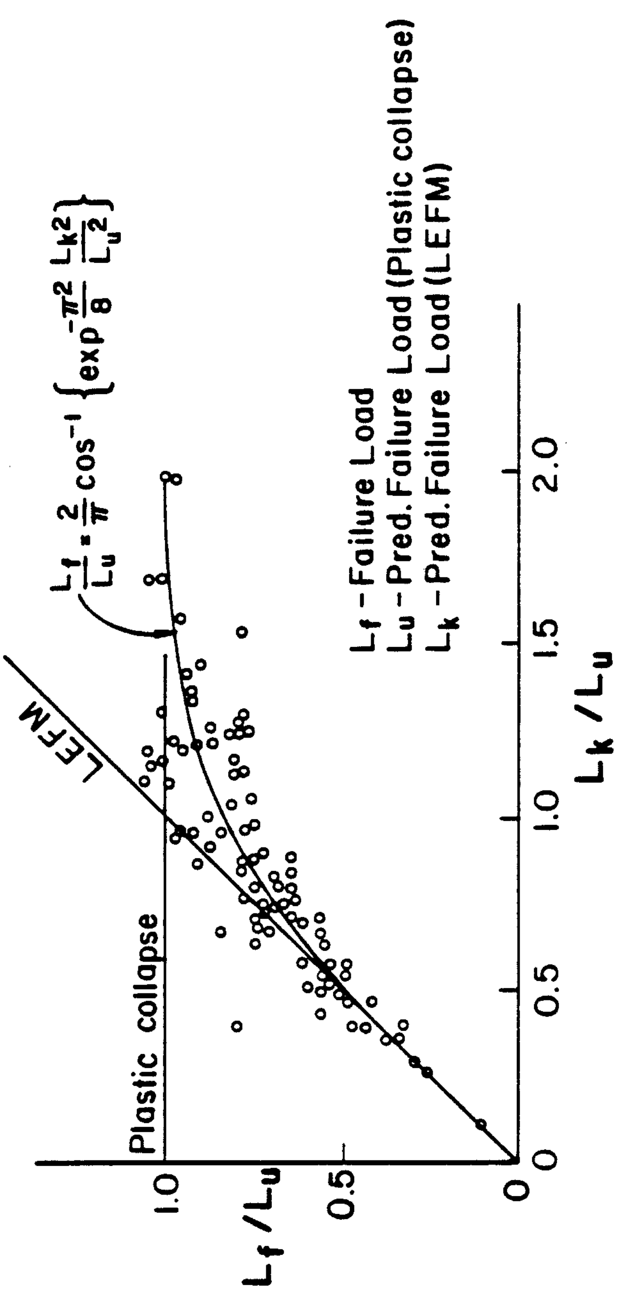

Figure 7.2. Comparison of Equation 7.11 with data as reported by Dowling *et al.* [7.3].

Assessment Diagram (FAD) by the Central Electricity Generating Board of England who have adopted Equation 7.12 as a valid method to determine the susceptibility of a flawed structure to failure. The method of solution proposed by Harrison *et al.* and outlined by Darlaston [7.10] is then as follows:

1. determine flaw shape and specimen geometry,
2. determine the stress at the flaw location,
3. calculate the stress intensity factor K,
4. determine the collapse load for the structure,
5. calculate K_r and S_r,
6. determine where on the FAD the coordinate (K_r,S_r) appears,
7. if the point is below the curve, there is no failure; if the point is above the curve, the structure is predicted to fail.

7.3. Limitations of the Two Criteria Approach

While this section discusses some limitations of the Two Criteria approach (called the CEGB–R6 criterion in England), it must be pointed out that at this time there is no other adequate engineering approach for the failure assessment of cracked structures to cover the full range of brittle to plastic behavior. While the other parameters discussed in the introduction to this chapter (J-integral, R-curve, COD, *etc.*) may eventually lead to an engineering approach, they all are still in a stage of development.

In deriving Equation 7.1 Burdekin *et al.* assumed a condition of plane stress; whereas later in the derivation (Equation 7.8) a state of plane strain

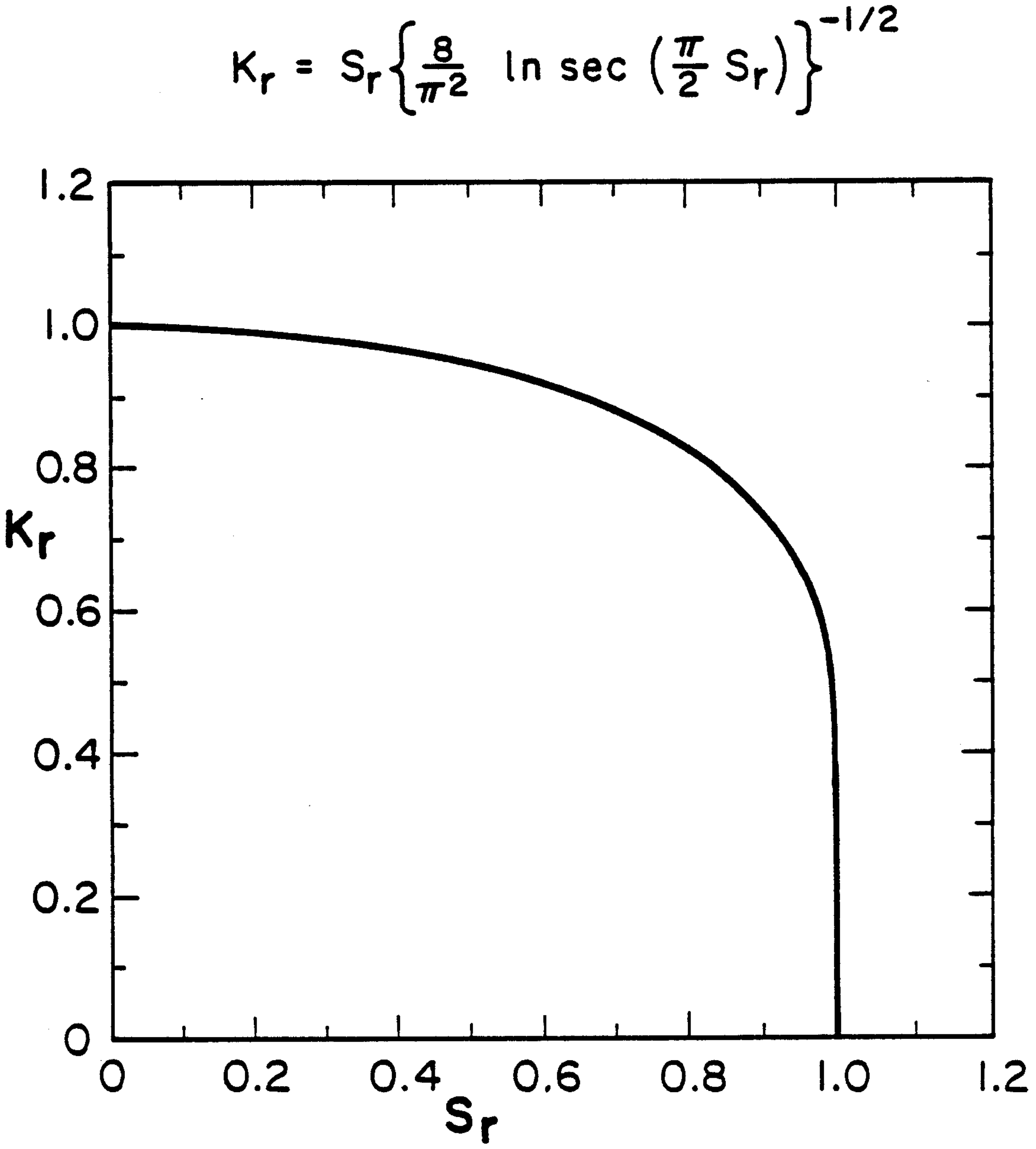

Figure 7.3. The Failure Assessment Diagram (FAD) used to determine the structural integrity of structures [7.9].

is assumed. Furthermore, the BCS model used to arrive at Equation 7.2 is strictly valid only for Mode III loadings and plane stress, yet the Two Criteria approach is used for Mode I and plane strain. Whereas in the BCS model the plastic zone lies in the same plane as the crack, it is known that the plastic zone ahead of the crack tip loaded in Mode I is formed in a larger area with the center at approximately 45° from either side of the plane of the crack (see Figure 7.4). However, even considering the above restrictive and mutually exclusive assumptions, the agreement of Equation 7.12 to data is quite good as illustrated in Figure 7.5, and it can therefore be used to describe, at least empirically, failure conditions over the entire range of brittle to plastic failure.

7.4. Primary Versus Secondary Stresses

In failure analysis a distinction must be made between primary stresses which will contribute to the general plastic collapse of a structure and secondary stresses which are self-equilibrating and do not contribute to the plastic collapse. Membrane stresses which can be caused by coolant pressure are primary stresses; another way to think of primary stresses is that local plastic strains in a structure will not change the primary stresses. Thermal, swelling, and residual stresses are usually considered secondary stresses; that is, they are strain-controlled stresses and are self-limiting once yielding of the structure occurs. It must be noted that the role of primary and secondary stresses in EPFM is still under discussion. Some researchers do not consider secondary stresses to contribute to brittle fracture while others consider both primary and secondary stresses to be applicable over the entire EPFM range.

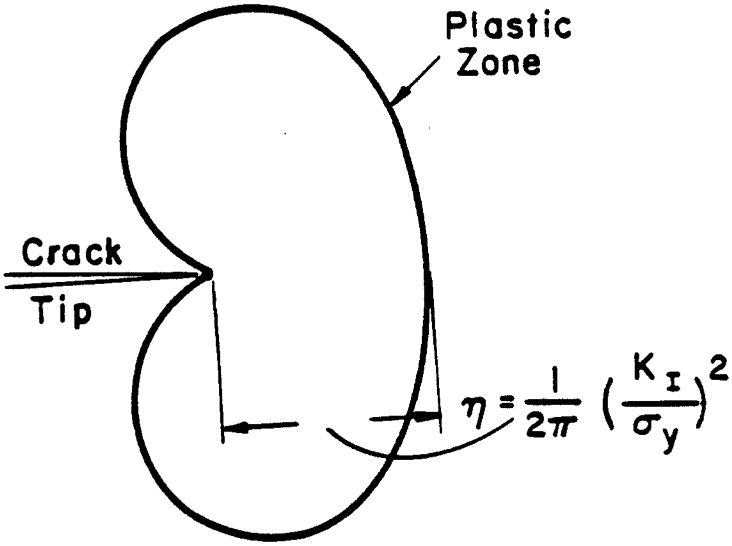

Figure 7.4. Illustration of the plastic zone in front and a crack tip.

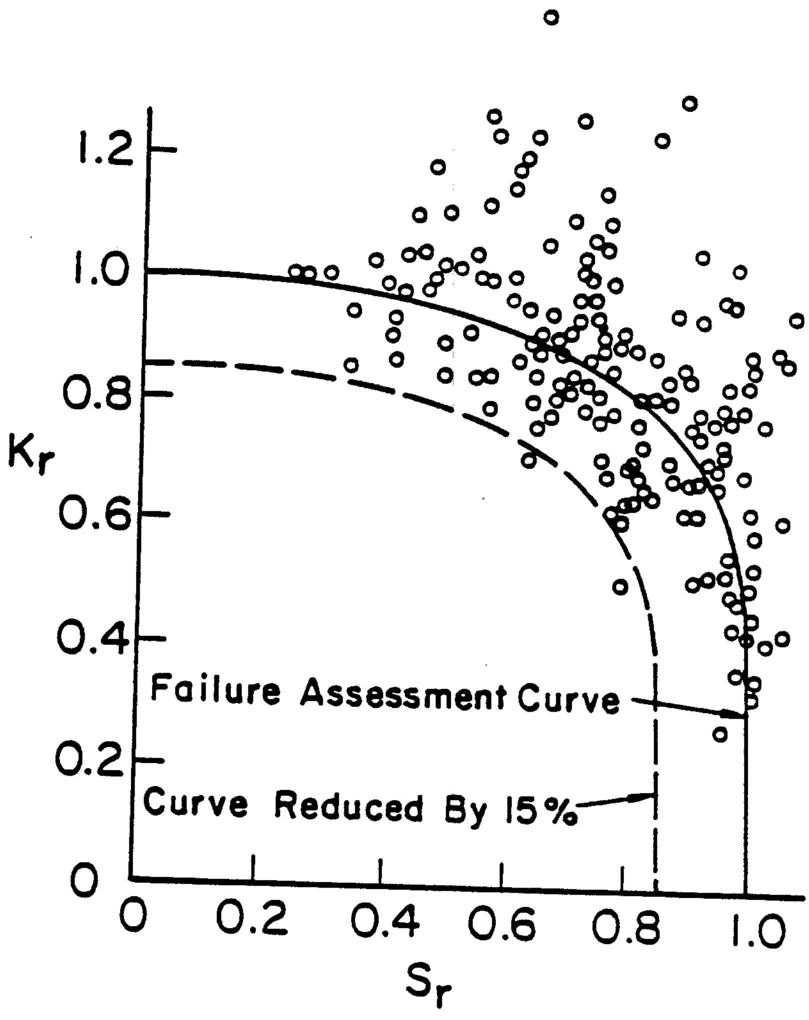

Figure 7.5. Comparison of experimental data points with the FAD [7.12].

Furthermore, even if the traditional method of treating primary stresses as those contributing to plastic collapse and primary plus secondary stresses as those contributing to brittle fracture is assumed, it is not always clear as to what constitutes a secondary stress [7.11]. In developing the methodology to include plastic collapse into EPFM, the standard convention is adopted that only primary stresses contribute to plastic collapse and primary plus secondary stresses contribute to brittle fracture, and that thermal and swelling stresses are secondary stresses. These assumptions are then consistent with both ASTM and CEGB standards.

For incorporating the distinction between primary and secondary stresses, Equation 7.12 is particularly useful. The brittle fracture contribution K_r and the plastic collapse contribution S_r are distinctly separated in that equation. Accordingly, K_r and S_r could be written as $K_r = K_r^p + K_r^s$ and $S_r = S_r^p$, where the superscripts p and s refer to primary and secondary loads. This would be correct if failure could be actually broken up into a brittle fracture and a plastic collapse. However, the effect of secondary loads on failure far from plastic collapse must be considered in a more detailed manner. It has been shown [7.12] that the plasticity effects of secondary loads do indeed contribute to the overall failure of a structure when that structure is far from plastic collapse. This can be thought of as a plastic contribution to failure of the secondary stress. The idea that plasticity influences failure is not a new one; it was first developed by McClintock and Irwin [7.13] when defining the extent of the plastic zone ahead of the crack tip. Using Irwin's expression for the extent of the plastic zone η due to secondary stresses, one obtains

$$\eta = \frac{1}{2\pi}\left[\frac{K^s(a)}{\sigma_y}\right]^2 \tag{7.13}$$

where a is the crack depth and K^s is the stress intensity factor due to secondary loads. Harrison *et al.* [7.9] have then recommended the following procedure to determine the effect of plasticity from secondary loads on failure:

1. find η using Equation 7.13,
2. calculate $K^s(a)/K^s(a+\eta)$,
3. with this ratio determine a quantity ρ [7.14] in Figure 7.6,
4. determine the total K_r^s from the equation $K_r^s = \frac{K^s}{K_{Ic}} + \rho$.

The variables then that need be determined are K_r and S_r and are given by

$$S_r = S_r^p, \qquad K_r = K_r^p + \frac{K^s(a)}{K_{Ic}} + \rho \tag{7.14}$$

The function ρ and its method of incorporation into K_r is based on the assumption that secondary loads affect failure in the following way. Secondary loads do affect plastic failure, contributing fully in the LEFM regime but not at all in the plastic collapse regime. Assuming a linear interpolation between the two, one can write S_r as

$$S_r = S_r^p + (1 - S_r^p)\, S_r^s \tag{7.15}$$

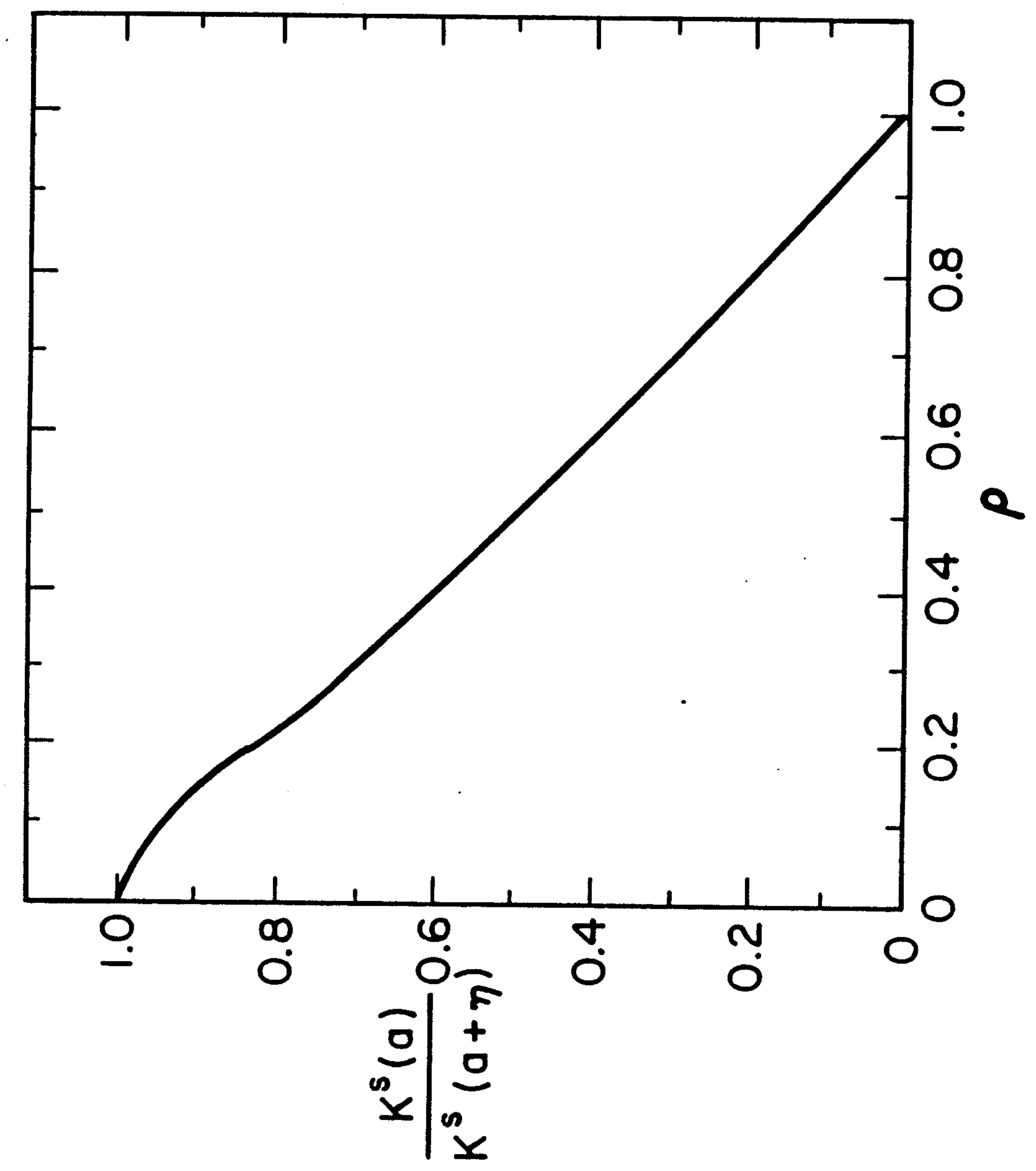

Figure 7.6. Functional dependence of ρ on the ratio $K^s(a)/K^s(a+\eta)$ [7.14].

Incorporating Equation 7.15 into Equation 7.12 would result in a new FAD where the ordinate is offset by some amount ρ. This amount ρ can be correlated with the size of the plastic zone η due to the secondary stress using the ratio $K^s(a)/K^s(a+\eta)$. Milne [7.14] has tabulated the quantity ρ and recommends its use in evaluating K_r in Equation 7.14, to allow for the offset in the ordinate in the FAD.

7.5. Plastic Collapse Analysis

Plastic collapse or limit load theory usually assumes elastic - perfectly plastic behavior (no work-hardening). Accordingly, the limit loads are expressed in terms of the yield strength σ_y only. To account for work-hardening of metals, σ_y is replaced by the flow stress $\bar{\sigma}$ taken to be $\bar{\sigma} = .5(\sigma_y + \sigma_u)$. The flow stress $\bar{\sigma}$ is considered a better measure of plastic collapse than the yield strength σ_y. In a smooth uncracked structure, plastic collapse would be predicted when the stress through the structure thickness is equal to or greater than the flow stress. However, the introduction of a crack in the structure will result in a stress redistribution around the cracked area. While the plastic collapse stress σ_p of a cracked structure will be less than the $\bar{\sigma}$ of the material, the calculation of σ_p is not always straightforward.

Chell [7.12] presents several complicated plastic collapse solutions for the standard-type Fracture Mechanics specimens (*i.e.* center cracked, double edge cracked). However, for the geometry of interest herein (a plate with a semi-elliptical surface flaw), Harrison *et al.* recommend the following equation

$$\sigma_p = \bar{\sigma}\left(1 - \frac{c}{w}\right)^2 \tag{7.16}$$

where $\frac{c}{w}$ is related to the crack dimensions and plate thickness as shown in Figure 7.7, and $\frac{c}{w} = \frac{\pi a l}{4t(l+t)}$. To calculate the applied stress in the area of the crack and hence S_r, the following equation is recommended [7.9]

$$S_r = \frac{\frac{\sigma_b^p}{4} + \sigma_m^p\left(\frac{c}{w}\right) + \left[\left(\frac{\sigma_b^p}{4} + \sigma_m^p\left(\frac{c}{w}\right)\right)^2 + \sigma_m^{s^2}\left(1 - \frac{c}{w}\right)^2\right]^{1/2}}{\bar{\sigma}\left(1 - \frac{c}{w}\right)^2} \tag{7.17}$$

where σ_b^p is the primary bending stress and σ_m^p is the primary membrane stress. The $\bar{\sigma}$ is a function of material properties, $\frac{c}{w}$ is based solely on geometry considerations, and $\sigma_{b,m}^p$ can be calculated given the stress distribution. For the case modeled herein, there are no primary bending loads and Equation 7.17 reduces to

$$S_r = \frac{\sigma_m^p}{\bar{\sigma}} \frac{\frac{c}{w} + \left[\left(\frac{c}{w}\right)^2 + \left(1 - \frac{c}{w}\right)^2\right]^{1/2}}{\left(1 - \frac{c}{w}\right)^2} \tag{7.18}$$

One other approximation used herein is in finding the ratio $K^s(a)/K^s(a+\eta)$. Knowing that $K \sim \sigma\sqrt{\pi a}$, the ratio can be approximated as $\sqrt{a/(a+\eta)}$.

The σ_y and the σ_u of a metal may be a strong function of temperature. Further, the upper and lower bounds on these measured properties may vary drastically at a constant temperature. Irradiation may affect these properties. To be conservative in calculating plastic collapse, lower values of σ_y and

σ_u for the temperatures of interest are used herein. However, irradiation effects on these properties are not considered due to lack of experimental data. Irradiation is usually thought of as causing an increase in both σ_y and σ_u. However, depending on the irradiation temperature, σ_y and σ_u may actually decrease with dose. Once the effect of irradiation on σ_y and σ_u is experimentally determined, it can be incorporated into the model. The values used herein are as follows: $\sigma_y^{316} = 450\text{MPa}$, $\sigma_u^{316} = 625\text{MPa}$, $\sigma_y^{ferrite} = 160\text{MPa}$, $\sigma_u^{ferrite} = 360\text{MPa}$; these are considered lower bounds.

7.6. Results

Incorporation of Equation 7.12 as a failure criterion into the methodology for crack growth as described in a previous chapter results in a more conservative (and more correct) failure condition than the brittle fracture condition discussed in that previous chapter. The Two Criteria failure condition (Equation 7.12) includes brittle fracture in one limit and plastic collapse in the other. The crack growth rate parameters have remained the same; it is only the failure conditions that are revised.

Using the same input parameters for the first wall conditions as discussed in a previous chapter, both a 316 stainless steel and a ferritic steel first wall were modeled. The results for 316 stainless steel show that plastic collapse is not an important consideration for the conditions imposed. That is, the structure is predicted to fail in a totally brittle fashion. This manner of failure is the result of a relatively higher flow stress $\bar{\sigma}$ and higher secondary stress (due to poorer thermal conductivity) compared to ferritic steel. The

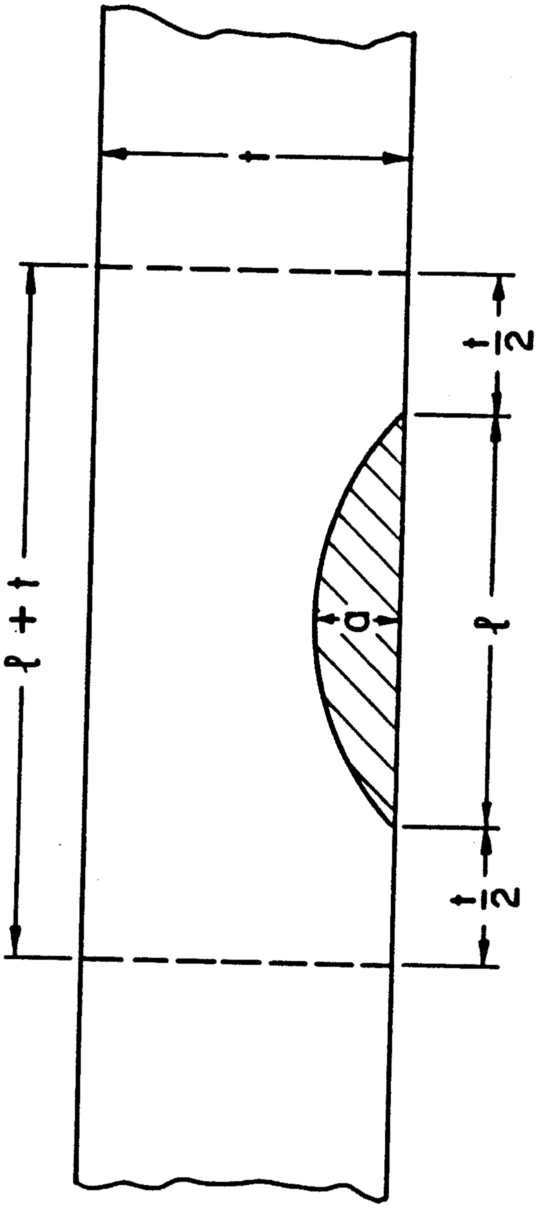

Figure 7.7. Illustration of geometry to calculate the quantity $\frac{c}{w}$ for the plastic collapse stress σ_p [7.9].

predicted time to failure is exactly as predicted in a previous chapter and is shown again in Figure 7.8. For ferritic steel, however, the conclusion is quite different. Because of the lower flow stress $\bar{\sigma}$ and smaller secondary stress, plastic collapse is not negligible for the conditions imposed. However, ferritic steel is still predicted to outlast 316 stainless steel. The structure is predicted to fail in about 22 years; a 15% reduction in the previous lifetime estimate for ferritic steel. Figure 7.9 illustrates the effect on lifetime as a result of incorporating the Two Criteria failure into the model. At the time of failure for the ferritic steel structure, neither pure brittle fracture ($K > K_{Ic}$) nor pure plastic collapse ($\sigma > \sigma_p$) would be found to cause failure independently; $K_r = .8$, $S_r = .9$. However, with a combined failure criterion (the Two Criteria failure, Equation 7.12), failure is predicted; see Figure 7.3. This clearly demonstrates that the assumption of either brittle fracture (LEFM) or plastic collapse does not give a conservative estimate of failure, and that a combined failure criterion is essential for reliable predictions.

While the predicted lifetimes are not meant to be accurate given the limitations of the material parameters, the results clearly show that plastic collapse cannot be ignored even when the structure is considered brittle. Nevertheless, due to the irradiation effect on K_{Ic}, brittle fracture is clearly an important failure mode for fusion reactor first wall structures.

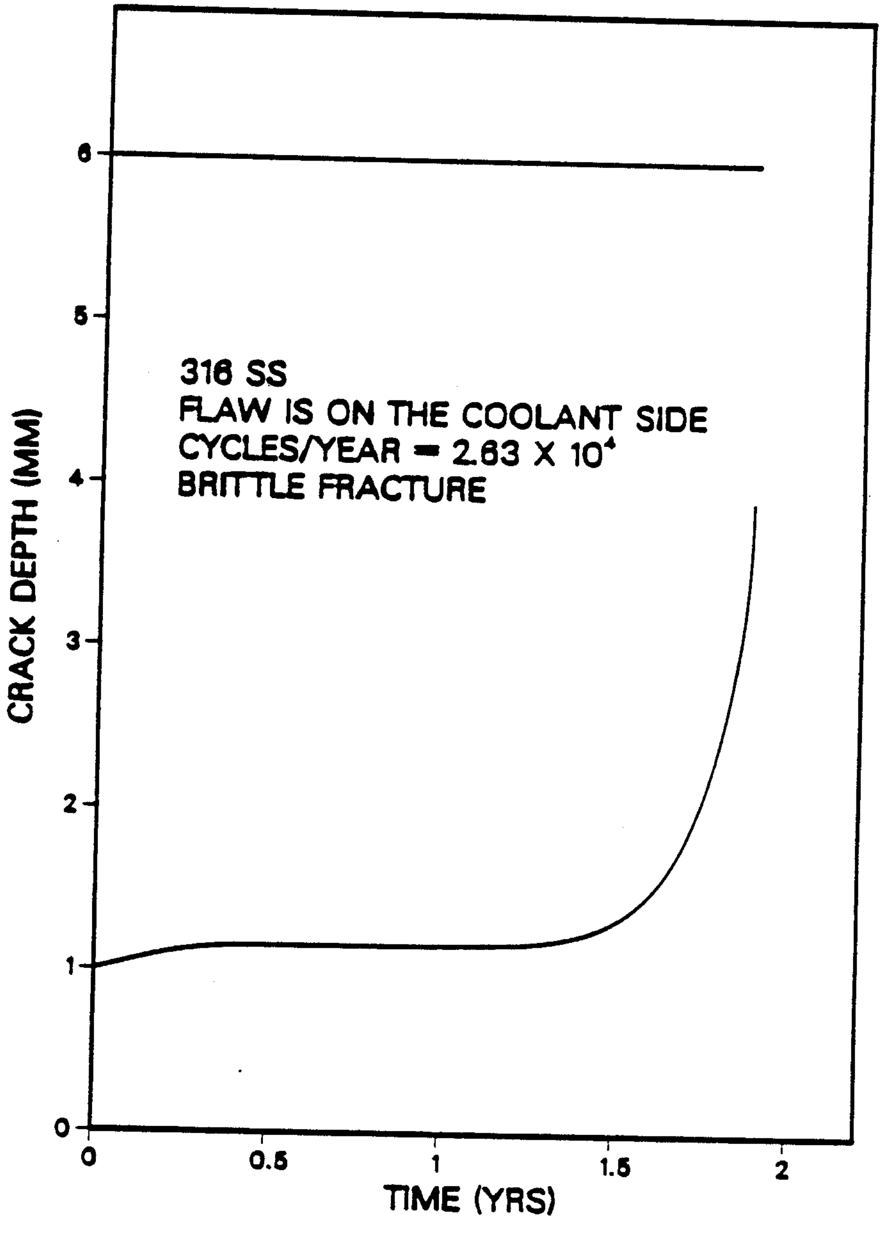

Figure 7.8. Crack depth into first wall versus time for 316 stainless steel. Lifetime estimate is unchanged from previous chapter.

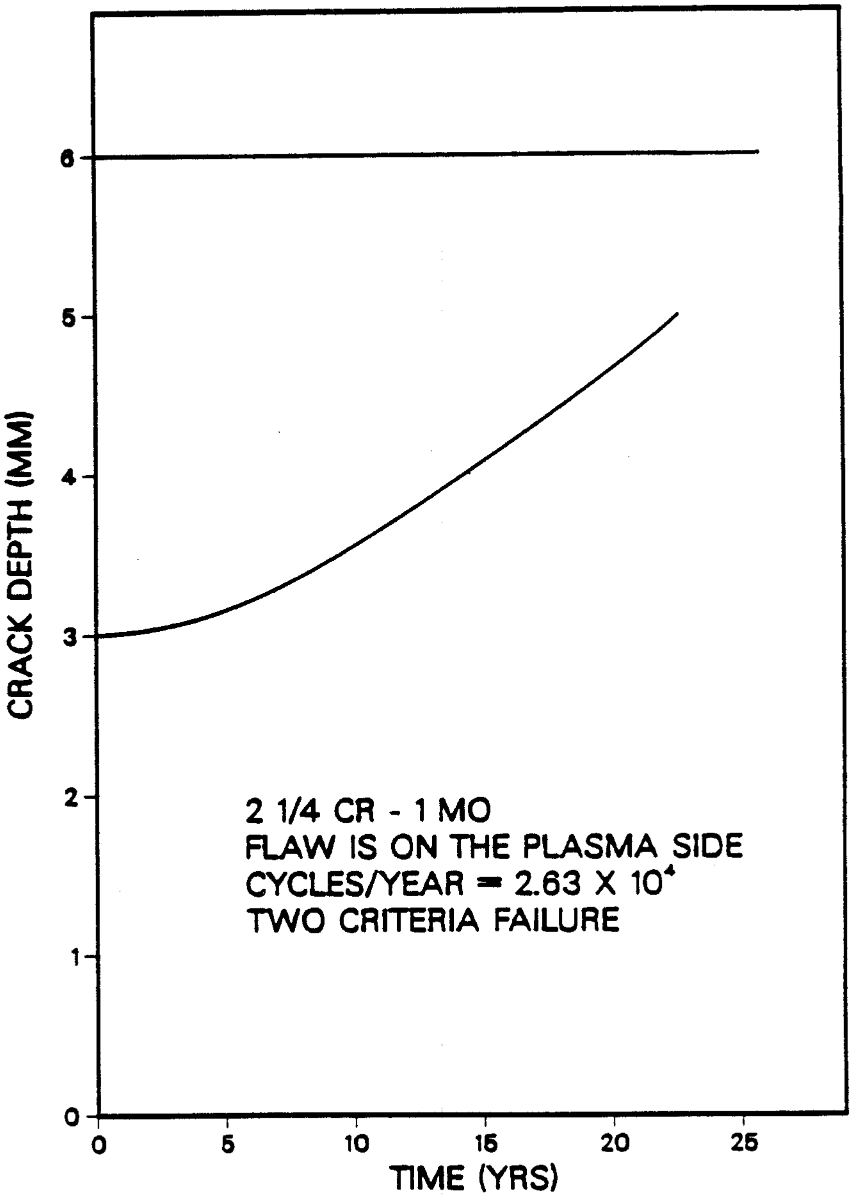

Figure 7.9. Crack depth into first wall versus time for ferritic steel. Lifetime estimate is reduced by 15% from previous chapter as a result of incorporating the Two Criteria failure. The maximum time of the wall thickness (upper) line indicates the previous lifetime.

References

[7.1.] Larsson, L. H., Use of EPFM is Design, *Advances in Elasto–Plastic Fracture Mechanics* (1979) 261–278.

[7.2.] ASTM Standard E399-72, *Annual Book of ASTM Standards* (1972).

[7.3.] Dowling, A. R. and Townley, C. H. A., The Effect of Defects on Structural Failure: A Two Criteria Approach, *International Journal of Pressure Vessel and Piping* **3** (1975) 77–107.

[7.4.] Heald, P. T., Spink, G. M., and Worthington, P. J., Post Yield Fracture Mechanics, *Materials Science and Engineering* **10** (1972) 129–138.

[7.5.] Bilby, B. A., Cottrell, A. H., Swinden, F. R. S., and Swinden, K. H., The Spread of Plastic Yield from a Notch, *Proceedings of the Royal Society A* **272** (1963) 304–314.

[7.6.] Dugdale, D. S., Yielding of Sheets Containing Slits, *Journal of Mechanics and Physics of Solids* **8** (1960) 100–104.

[7.7.] Burdekin, F. M. and Stone, D. W. E., The Crack Opening Displacement Approach to Fracture Mechanics in Yielding Materials, *Journal of Strain Analysis* **1** (1966) 145–153.

[7.8.] Griffith, A. A., The Phenomena of Rupture and Flaw in Solids, *Transactions, Royal Society of London, A-221* (1920).

[7.9.] Harrison, R. P., Loosemore, K., Milne, I., and Dowling, A. R., Assessment of the Integrity of Structures Containing Defects, *Central Electricity Generating Board R/H/R6–Rev.2* (1980).

[7.10.] Darlaston, B. J. L., The Development and Application of the CEGB Two Criteria Approach for the Assessment of the Defects in Structures, *Advances in Elasto-Plastic Fracture Mechanics* (1979) 319–357.

[7.11.] Chell, G. G. and Ewing, D. J. F., The Role of Thermal and Residual stresses in Linear Elastic and Post Yield Fracture Mechanics, *International Journal of Fracture* **13** (1977) 467–479.

[7.12.] Chell, G. G., Elastic–Plastic Fracture Mechanics, *Developments in Fracture Mechanics - 1, Editor: G. G. Chell* (1979) 67–105.

[7.13.] McClintock, F. A. and Irwin, G. R., *ASTM STP 381* (1965) 84.

[7.14.] Milne, I., Failure Assessment, *Developments in Fracture Mechanics–1, Editor: G. G. Chell* (1979) 259–301.

Chapter 8

Conclusions

The overall goal of this research is to determine what are the important factors in calculating a fusion reactor first wall lifetime. Several aspects have been examined; and these include:

1. the theoretical EOS for helium to determine accurate compressibility factors and pressure;
2. the evolution of the dislocation density which helps determine sink strengths as a function of time;
3. the swelling behavior of irradiated steels as a function of helium gas pressure, basic materials properties, and time-dependent sink strengths and bias factors;
4. the stress distribution through a thin walled structure given the swelling and creep properties, and including a novel stress analysis for a thin shell element;
5. the brittle fracture lifetime comparison between 316 stainless steel and ferritic steel with an accurate stress distribution history as input;
6. the incorporation of plasticity effects into the failure model for a thin walled structure by way of the Two Criteria failure law.

Based on this somewhat narrow analysis of crack propagation and subsequent failure, it is found that ferritic steel has several advantages over 316 stainless steel. Ferritic steel has a lower swelling rate, has lower cyclic thermal stresses, and is less susceptible to brittle fracture. Even though ferritic steel is more susceptible to plastic collapse, the calculated lifetime of ferritic steel is over 10 times longer than that for 316 stainless steel.

Specific conclusions and future improvements to each model include the following:

1. The EOS developed to determine the helium pressure in bubbles of irradiated steels is based on sound theoretical principles and should be good for very high densities. The gaseous EOS agrees quite well with the limited experimental data. However, no solid helium data exists. Once solid data becomes available, it may be necessary to re-evaluate the vibrational contribution to the solid EOS. For determining the pressure within the helium bubbles, the present model is adequate.
2. The dislocation evolution model agrees well with the limited data. The model does not consider small dislocation loops (important at temperatures below about 400°C). Further, there are two adjustable parameters, the mesh length and bias variance, which are determined so that a good fit to the data will result. But, these numbers are consistent with real material properties. If this model is to be improved it should be done in the above mentioned areas.
3. The void swelling model gives excellent agreement in the steady state regime. The incubation period, however, does not agree well with the experimental results. There is no doubt that the physics of void nucleation could be incorporated to better model early swelling behavior. Additionally, late in life the model does not predict a saturation to

swelling. While the existence of a saturation has not been shown, it appears likely that one should exist. This could probably be handled by assuming that if the ligament between the voids becomes on the order of the distance between dislocations (mesh length) then dislocations no longer contribute as sinks and swelling stops.

4. The stress analysis for a thin shell element is complete. However, computationally much more could be done. The effect of radius of curvature and bending moment could be examined, and comparison to standard stress equations could be done to understand the improvements gained in the new stress analysis.

5,6. The lifetime analysis models crack propagation and subsequent failure. No experimental data exists to confirm the results of the model. The model is, however, based on sound theoretical grounds. The biggest improvement to the model would be in the area of plastic collapse. While plasticity effects are included, a more detailed model of the plastic collapse stress of a structure could be performed. If any other failure criterion (such as J-integral) evolve sufficiently for engineering use, it should be examined for applicability to the problem. Other improvements to the lifetime model would include the use of cyclic stress-strain data instead of static stress-strain data, and the incorporation of creep-fatigue interaction into crack growth modeling.